Experimental Studies of High-Speed Dense Dusty Gases

Thesis by

A. V. Anilkumar

In Partial Fulfillment
of the Requirements for the Degree of
Doctor of Philosophy

California Institute of Technology
Pasadena, California

1989
(Submitted November 4, 1988)

Dedicated to my parents

ACKNOWLEDGMENTS

I would like to thank my advisor, Professor Bradford Sturtevant, for guiding this research effort. His keen physical insight and enthusiasm for tackling new and challenging problems in fluid mechanics have been inspirational. I am also thankful to him for his detailed editorial assistance and for his help in typesetting this manuscript.

I would like to thank all fellow members at GALCIT for making this work possible. In particular, I am thankful to: Mr. George Lundgren for construction of the flow facility, Ms. Betty Wood for the elegant drawings, and Dr. Harry Robey for rekindling my interest in electronics.

This work was supported in part by the Programs for Experimental and Theoretical Chemistry and Fluid Dynamics and Hydraulics, National Science Foundation, under NSF Grant No. EAR-8512724.

ABSTRACT

An experimental study of the flow of high-speed dense dusty gases has been conducted in a novel shock tube facility. The flow is generated through rapid depressurization and subsequent fluidization of a stationary packed bed of particles loaded under pressure in the vertical driver section of the shock tube. The flow was studied with high-speed photography and fast-response pressure transducers.

The studies have been exploratory in nature. The entire process of lofting and disassembly of packed particle beds has been documented. A wide spectrum of dusty flows with particle loadings ranging from that of a fully packed plug to that of a dilute disperse particle flow was observed in this facility. Only extreme flow fields like packed plug flows and very dilute disperse particle flows were found to be uniform. All other flow fields, with intermediate particle loadings, were characterized by the simultaneous presence of dense filamentary structures and dilute dispersions of particles. Typically, while operating with 0.5 mm glass beads, flows reached speeds of 60 meters per second in a period of 25 milliseconds.

Two lofting configurations of the packed beds were set up. In the first configuration, the rapid depressurization of the interstitial bed fluid and the consequent initiation of bed expansion was examined. Bed expansion starts along horizontal fractures that partition the bed into slabs. While the bed is accelerating, particles rain down from the bottom surfaces of the slabs partitioning the fractures into bubbles with a characteristic honeycomb pattern. The bubbles eventually compete and the dominant ones prevail. The observed instability of the bottom surfaces of the slabs is analogous to the Rayleigh-Taylor instability observed in continuous media. The flow development in this configuration was not influenced by any wall effects.

The second lofting configuration is a high-speed fluidization configuration. Here, the role of the fluid entering from below the bed, in continuing the bed expansion initiated by the rapid depressurization of the interstitial bed fluid, was examined. The bed expansion occurs along expanding and elongating bubbles and the bubble walls are stretched into dense filamentary structures. Beds initially stacked with a gradient in particle size or density or both showed drastic differences in response to fluidization. The morphology of the expanded flow field in all cases was essentially the same: nonuniform, interspersed with dense filamentary structures and dilute dispersions of particles.

In the second lofting configuration, only the late stages of flow development were influenced by wall effects. Wall effects manifest as faster moving fluid along the walls and denser accumulation of flow structures towards the center of the channel. The bottom of the dusty flow is characterized by the presence of a *tail*; a concentric dense particle column formed by the accumulation of particles, initially present in the bottom regions of the flow. The tail terminates in a bulbous and streamlined bottom from which particles are slowly eroded by the coflowing fluid.

A multi-transducer probe was installed in the dusty gas flow for making dynamic pressure measurements and for correlating observations with those made through extensive flow visualization.

TABLE OF CONTENTS

LIST OF FIGURES

LIST OF TABLES

LIST OF SYMBOLS

Symbol	Description
a	Acceleration
A	Sound speed (appendix C)
b	Forscheimer constant (equation D2)
d	Diameter
D	Bed width (channel width)
DP	Dynamic pressure
f	Fracture size
g	Acceleration due to gravity
h	Bubble height
K	Expansion fan strength (appendix C)
l	Bed height
l_0	Initial bed height
Δl	Bed expansion (Tables 5.1, 5.2)
L	Distance below window center
m	Dust density
M	Dust mass loading (m/ρ_g; equation 6.4)
P	Pressure
P_0	Diaphragm burst pressure
P_1	Instantaneous pressure during depressurization (appendix C)
P_{T1}	Total pressure of the dusty gas (§6.2)
P_{T2}	Total pressure of the gas phase (§6.2)
P_{T3}	Static pressure in the channel (§6.2)
ΔP	Pressure difference across the bed (Tables 5.1, 5.2)

Re	Slip Reynolds number $\frac{\rho_g U d_p}{\mu}$
s	Slab thickness (initial spacing between fractures)
S	Displacement
t	Time
T	Transducer
T1	Probe transducer (total pressure dusty gas; §6.2)
T2	Probe transducer (total pressure gas; §6.2)
T3	Probe transducer (static pressure; §6.2)
u	Velocity
U	Slip velocity ($u_g - u_p$)
$\overline{U}$	Average fluid through flow velocity in a porous bed (equation D3)
x	Distance
α	Empirical constant for fracture growth rate (§3.2.3)
γ	Ratio of specific heats
ε	Fluid volume fraction (bed porosity)
κ	Permeability of the bed (equation D1)
μ	Dynamic viscosity
ρ	Density
$\overline{\rho}$	Average density of through flow past porous bed (equation D3)
τ	Time at which fractures are completely partitioned into bubbles

Subscripts

b	bubble
g	gas
p	particle
w	window

Chapter 1

INTRODUCTION

1.1. Motivation.

The present work is an experimental study of the flow of high-speed dense dusty gases in which the effects of the earth's gravity are unimportant compared to the large accelerations that occur. The flow is generated in a novel vertical shock tube facility by rapid depressurization and subsequent fluidization of a uniform packed bed of particles loaded under pressure in the shock tube driver section. The main objectives of this investigation have been: (i) to understand the detailed mechanism by which the dense dusty flow is generated in the facility, (ii) to study the effects of various initial operating conditions on the characteristics of the flow, and (iii) to make dynamic pressure measurements in the flow field.

Dusty gas flows are two-phase flows of gas and particles. The term dense specifically refers to flows in which the momentum flux of the particulate phase is greater than, or at least equal to, that of the gas phase, usually due to the fact that the mean density of the particulates is high. The term high-speed has been used here to refer to flows with particle transport velocities of the order of tens of meters per second. The dense dusty flows generated in this facility are rapidly accelerating flows. Typically, speeds of 60 meters per second were realized in a 25 millisecond period, with 0.5 mm dia glass beads, representing an average acceleration of 240 times that due to gravity.

In rapidly accelerating flows, with accelerations about a few hundred times that of gravity, the slip velocities (U) and consequently the slip Reynolds numbers (Re) of particles are an order of magnitude higher than the corresponding ones for free fall.

$$\text{slip velocity:} \quad U = u_g - u_p$$

$$\text{slip Reynolds number:} \quad \mathrm{Re} = \frac{\rho_g \, U \, d_p}{\mu}$$

where u_g is the gas velocity, u_p is the particle velocity, ρ_g is the gas density, μ is the dynamic viscosity of the gas and d_p is the particle size. While working with macroscopic particles (0.1 mm < d_p < 1 mm), the slip Reynolds numbers in rapidly accelerating dusty flows are high, and consequently the near field interactions between particles, namely particle wake interactions and collisional interactions, become important.

Rapid depressurization refers to the depressurization brought about by the passage of an expansion wave. In the current experiments, the interstitial bed fluid is rapidly depressurized, and consequently as the fluid is accelerated it drags the particles along creating an accelerating and expanding dense dusty flow. Typically, in this facility, a bed at 3 bar pressure is rapidly depressurized in the top layers in about 3 milliseconds. This represents an average rate of pressure drop of 1000 bar per second.

Fluidization conventionally refers to the dispersion of particles from a settled porous state, namely a packed bed, to one where particles are free to move around, the change being brought about by an upward flow of fluid from below the bed. High-speed fluidization in the current experiments follows the rapid depressurization of the interstitial bed fluid and is nonsteady in nature; in that the expanding bed continuously accommodates an increasing through flow.

1.2. Background.

High-speed dense dusty flows are encountered both in nature, as in pyroclastic flows (Sparks *et al.*, 1978; Kieffer and Sturtevant, 1984), avalanches (Voight, 1979) *etc.*, and in industrial contexts, as in dust explosions in mines (Bracht and

Merzkirch, 1979), nuclear air blast induced lofting (Zernow *et al.*, 1973), fast fluidization (Yerushalmi and Avidan, 1985), *etc.* Very little fundamental knowledge exists about how these flows are generated, about the role of transient effects on flow development, about the morphology of the flow field and about methods to monitor these flows. The present investigation, which is the first one of its kind, has addressed these issues in detail. The experiments have been exploratory in nature with the intention to point out simplifications in approach to understanding these flows. The results should have additional implications in modeling such flows. The advantage here is that dense dusty flow is generated starting from a perfectly uniform configuration, namely a packed bed, and the flow features that develop during the course of the experiment can in large part be traced to flow processes and instabilities which are the objectives of this study.

Pyroclastic flows generated by depressurization during explosive volcanic eruptions (Wilson *et al.*, 1980) have typical speeds of a few hundred meters per second in the two-phase regions of volcanic conduits, and the accelerations involved can be many times that of gravity. In the study of such high-speed pyroclastic flows (Walker and McBroome, 1983; Wilson, 1984; Valentine and Fisher, 1986) there has been considerable controversy as to whether the dusty flow should be modeled as a dilute and uniform turbulent flow or as a highly concentrated particle flow. The possibility of flows with both particle loadings existing simultaneously is totally ignored. The present experimental investigations show that such high-speed dense dusty flows although highly turbulent are strongly inhomogeneous with both dilute particle flow and dense aggregate flow occurring simultaneously.

Depressurization experiments have been done by Zernow *et al.* (1973) to simulate dust lofting behind a decaying blast wave in the far field of a surface nuclear blast; the lofting being brought about by the flow of air into and out of the sand medium behind the decaying blast wave. Zernow *et al.* built a vertical shock tube to simulate this surface breathing phenomenon. Here, typically a 7.5 bar

overpressure, imposed on a sand bed behind a reflecting shock wave, is slowly released over 0.75 seconds. This represents an average rate of pressure drop of 10 bar per second. This slow depressurization can be treated as a quasi-steady process and using Darcy's law (appendix D) to model gas flow through the sand medium, Zernow *et al.* estimate the transient presure distribution and resulting accelerations on the sand. Morrison (1977), Nilson (1981) have also used the quasi-steady approach to predict the transient pressure distribution in a porous medium that is suddenly exposed to a high pressure gas at one end. This simulates the flow conditions in the backfill following an underground nuclear explosion. They employ the Forscheimer relation (appendix D) to model the flow through the porous medium.

Fluidization (Davidson *et al.* 1977) provides a mechanism for bringing fluids and particles into intimate contact and, as such, has found wide application in chemical process engineering. All fluidization experiments in literature are steady flow experiments. Typically, fluidization is achieved by starting with a packed bed of particles, mounted on a porous screen in a channel, and subjecting it to a fluid through flow. As the through flow rate is increased, the bed expands and different flow regimes are observed. Incipient fluidization is the quiescent state attained when fluid through flow rate just supports the buoyant weight of the particles. Beyond this, with increased through flow rate the particles are dispersed. Uniform particle dispersion, however, is not achievable in practice till high levels of dilution are reached. In gas fluidized beds, where the nonuniformities are more apparent, excess fluid, beyond that necessary for incipient fluidization, leaves the bed as bubbles. These bubbles, which are formed at the distributor, resemble spherical cap bubbles (Davies and Taylor, 1950) rising in a mildly viscous fluid. In water fluidized beds, several investigators have observed organized motion of particles like steady patterns of recirculation and propagation of narrow strata of particles upwards through the bed (Willus, 1970; El-Kaissy and Homsy, 1976; Fortes *et al.* 1987).

In the context of fluidization, two and three-particle level interactions, and single-particle column experiments have received much attention. Happel and Pfeffer (1960) studied the interaction effects in two-particle systems with one plastic sphere (~ 6 mm dia) falling above the other in a viscous fluid. They found inertia effects, leading to attraction between the two spheres, dominant at Reynolds numbers as low as 0.25. The attracting spheres flip and assume stable high drag cross stream orientations. Volpicelli *et al.* (1966) fluidized a single column of large aluminum spheres (~ 3 mm dia) with water and, just beyond incipient fluidization at Reynolds number around 220, found that large horizontal discontinuities occur locally in the bed. They attributed such inhomogeneities in particle dispersion to the inherent mechanism of fluidization but did not elaborate on it. Fortes *et al.* (1987) systematically repeated the experiments of both Happel and Pfeffer and Volpicelli *et al.* by fluidizing large glass beads (~ 6 mm dia) with water at Reynolds number around 1000. They identified the wake-dominated suction between close spheres as responsible for attraction between them and formation of stable high drag horizontal arrays. They call the discontinuities occurring just beyond incipient fluidization, in their single column experiment, *void cracks*. The void cracks start as local horizontal discontinuities in the flow, grow in the flow direction and erupt at the top of the bed. Upward-moving horizontal strata of particles which they observe at higher dilutions are also manifestations of the stable high drag configurations assumed by particles. Fortes *et al.* did not observe any void cracks in three-dimensional beds, probably because here incipient fluidization occurs at lower Reynolds numbers. Also, no void crack observations have been documented in gas fluidization, not even in the case of large particles. In the current experiments, rapid depressurization leads to the formation of horizontal fractures in the bed, and this constitutes the first step in the complex bed disassembly process.

Fast fluidization is a term coined by Yerushalmi *et al.* (1976) to characterize a gas fluidized bed with fluid volume fractions (ε) between 0.8 - 0.95 and superficial gas velocities an order of magnitude higher than the terminal velocities of individual particles, resulting in a high rate of material carry over. Fast fluidization overcomes the problem of improper fluid particle contact in bubbling gas beds and low mass handling capacity of very dilute but homogeneous gas particle flows. In their experimental apparatus, Yerushalmi *et al.* observe that the fast fluidized bed is characterized by the simultaneous presence of individual particles and aggregates of particles in dense clusters which break and reform. Here the fluidized density is higher at the bottom than at the top. The aggregates formed are due to wake interactions between particles. The fluidized system in the current investigation resembles a fast fluidized bed, yet there are differences. The experimental apparatus of Yerushalmi *et al.* is patterned after industrial processes. It is a steady recirculation type fluidized bed where the material carried over in the fluid stream is reinjected at the bottom of the fluidization channel. This injection and extraction probably introduces large nonuniformities into the flow. The facility in the current investigation has a simple geometry and there is no material recirculation. Fast fluidization is achieved in a tall vertical channel starting with a uniform packed bed of particles and thereby a clear route to such a fluidization regime can be established. The average transport velocities in the current investigation are an order of magnitude higher than in conventional fast fluidized beds. Particle sorting by size or density is negligible during the course of the experiment.

Wake interactions, between particles close to each other, are also responsible for choking in pneumatic transport (Zenz and Othmer (1960)). Choking is the collapse into aggregates of an initially uniform high Reynolds number gas particle flow. Choking can occur even at 1% by particle volume in the flow.

Tsuji *et al.* (1982) have used drag measurements and flow visualization to study the wake-dominated longitudinal and transverse interactions between spheres at high

Reynolds numbers (Re ~ 100 - 1000) in a water tunnel. In longitudinal interaction, the rear sphere experiences a strong drag reduction, and the effects last up to 10 diameters, while in transverse interaction, the spheres experience a drag increase with effects lasting up to 3 diameters. Tsuji *et al.* were unable to point out any Reynolds number effects in their experiments.

1.3. Outline of Present Work.

The organization of the present work is as follows:

In chapter 2, the facility developed to generate dense dusty flows, along with the instrumentation to monitor these flows is described. Two initial lofting configurations are set up. In configuration 1, a moderate-to-long bed ($4 < l_0 / D < 16$; l_0 = initial bed height, D = bed width) is loaded at the bottom end of a short driver. The rapid depressurization of the interstitial bed fluid and the consequent initiation of bed expansion is examined. In configuration 2, a short-to-moderate length bed ($0.5 < l_0 / D < 4$) is mounted on a porous mesh in the driver section with a long reservoir of working fluid below it. The role of the fluid entering from below the bed, in continuing the bed expansion initiated by the rapid depressurization of the interstitial bed fluid, is examined.

In chapter 3, the results of the rapid depressurization experiments in configuration 1 are presented along with flow visualization and pressure measurements. Here, the bed disassembly consequent to the rapid depressurization of the interstitial bed fluid occurs along horizontal fractures that partition the bed into slabs. During the acceleration phase of the bed expansion, particles rain down from the bottom surfaces of the slabs partitioning the fractures into bubbles with a characteristic honeycomb pattern. This instability of the bottom surfaces of the slabs is analogous to the Rayleigh-Taylor instability observed in continuous media (Sharp, 1983; Baker *et al.* 1987). The parameters varied in the experiments are particle size and bed height. The quantitative results are discussed in terms of bed

speeds, bed expansion and fracture characteristics like: i) initial slab thickness, ii) fracture partitioning time and iii) initial bubble width. Speeds up to 15 m/s were attained in this configuration.

In chapters 4 and 5, the results of the rapid depressurization and high-speed fluidization experiments in configuration 2 are presented along with flow visualization and pressure measurements. The presentation in chapter 4 is qualitative in nature. The various stages of flow development are outlined here. As the bed expansion occurs along bubbles, the through flow increases, and the bubble walls are continuously stretched, resulting in a flow with dense filamentary structures.

In chapter 5, the quantitative results of a parameter study on experiments in configuration 2 are discussed. Parameters varied are particle size, particle composition, particle density, bed height and what will be called acceleration gradient (cf. §5.2). The effects of bed height (l_0) and particle size (d_p) are recorded by the ratio l_0/d_p. The fluidization mechanics is strongly influenced by the presence of a gradient in acceleration, set up by stacking particles of different size or density or both, in the stationary bed prepared for lofting. In high acceleration-to-low acceleration stacking configuration, the bed cannot expand and lofts as a plug. The reverse stacking configuration is highly unstable. The results have implications in understanding the fluidization response of monodisperse and polydisperse systems. A time study of fluid and particle velocities, and slip Reynolds numbers in stable and unstable lofting has been presented. Reynolds numbers of through flows attaining quasi-steady conditions have been directly estimated using the Ergun equation (appendix D). The role of wall effects and electrostatic forces on flow development are also discussed. Speeds up to 60 m/s were realized in configuration 2.

In chapter 6, dynamic pressure measurements of the flow fields in configuration 2 are presented. One can characterize all the features of the flow field with the probe. In flows such as these, a point measurement of the dynamic pressure of the dusty gas will be very useful. Some typical estimates of dust loadings have also been presented.

In the appendix, some of the key electronics and instrumentation that was developed to run the experiments is discussed. Also, the governing equations for fluid flows in shock tubes, and fluid flows through porous media are discussed.

Chapter 2

EXPERIMENTAL FACILITY & INSTRUMENTATION

2.1. Dusty gas shock tube.

The shock tube facility fabricated to generate dense dusty flows is operated in the mode of a Ludwieg tube (Ludwieg, 1957; Cable & Cox, 1963), in that the flow in the high pressure driver section of the shock tube is studied. To generate the dusty flow, the driver section is first loaded with a bed of particles and pressurized with the working gas. Flow is then initiated by rapid depressurization through diaphragm rupture. Two configurations were used. In configuration 1, a moderate-to-long bed ($4 < l_0 / D < 16$) is loaded at the bottom end of a short driver (Figures 2.1, 2.2). Lofting occurs due to the rapid depressurization of the gas within the bed. In configuration 2, a short-to-moderate length bed ($0.5 < l_0 / D < 4$) is loaded on a mesh screen in the driver with a long reservoir below (Figures 2.3, 2.4). Lofting occurs here due to both the rapid depressurization of the gas within the bed and subsequent fluidization by the gas below the bed. The generated dusty flow is monitored by fast-response pressure transducers and high-speed photography.

The driver and driven sections of the shock tube are separated by diaphragm and knife blades (Figures 2.2, 2.4). The shock tube is folded to accommodate it within the laboratory. The test-section is 3.8 cm square in inside dimension and 80 cm in length. It has an all-welded aluminum construction and is flat black anodised. The test-section has two viewing windows 11.4 cm long, located on opposite walls. The windows are made from plexiglass, which is machined flat and polished. The center of the window is 80 cm below the diaphragm section. The spacers are square aluminum tubes with the same inside dimension as the test-section, and they are used to load the beds from different starting locations below the window. The spacers are 8.9 cm, 17.8 cm and 35.6 cm long. The rest of the facility is round in cross section and made from rigid aluminum tubing. The closest match in inside cross sectional areas between the square

test-section and the round tubing was obtained with a tube with 4.1 cm inside diameter, representing a round-to-square area ratio of 1.1. The transition section is 11.4 cm long and was molded using aluminum epoxy liquid (*Devcon F-2*). The elbows have a 21.6 cm radius.

The overall length of the facility in configuration 1 is about 7 m and in configuration 2 about 13 m. In configuration 2, the facility was often lengthened to 17 m to achieve longer test-times. The working gas is nitrogen drawn from a pressurized bottle. The diaphragm material is 50 μm, 1145 aluminum foil with H19 temper. This material provided the most consistent burst conditions, and different operating burst pressures were achieved by changing the initial spacing between the diaphragm and knife blades. The maximum operating pressure in the driver section was 4 bar. The starting driven section pressure was always atmospheric.

The flow in the facility, especially in configuration 2, is characterized by the presence of colliding particles. While operating with glass beads, the collisions between the beads generates a lot of fine glass dust which clogs up the exhaust valve if the exhaust port is located anywhere above the bed. Hence the exhaust port is located at the bottom end of the driver. A scanning electron microscope study of the fine dust revealed an average size of 5 μm. Also, due to the erosive nature of the flow, the window needed polishing every few runs.

2.1.1. *Particles*. Glass beads, plastic beads, steel beads and ignimbrite volcanic ash were used in the experiments. Glass beads are inexpensive, readily available in various sizes and do not stick to the walls. Also their flow speeds, generated with the typical working pressures, made them optimally suited for motion-picture photography. Hence, most of the experiments were done with glass beads. The other types of particles were used only when it was necessary to understand the effects of particle density and composition on flow characteristics. The details of the particles used are listed in Table 2.1. All particles come in small tolerance ranges. Average size has been used to

designate the particles.

The ignimbrite volcanic ash, composed of particles of different sizes, density, shape and surface texture served as a typical naturally occurring bed material. The volcanic ash was dried and sieved before using, and the working sample chosen had particles in the size range 0.1 mm to 1.5 mm.

Table 2.1. Particles used

Type	d_p (mm)*	ρ_p (g/cc)**
Art 31/14 Glass beads (Jaygo)	0.09	2.5
P-0060 Glass beads (Potters)	0.125	2.5
P-0080 Glass beads (Potters)	0.18	2.5
P-0120 Glass beads (Potters)	0.25	2.5
P-0230 Glass beads (Potters)	0.5	2.5
Art 31/5 Glass beads (Jaygo)	0.75	2.5
A-100 Glass beads (Potters)	1.0	2.5
Polystyrene microcarriers (Ventrex)	0.18	1.04
Acetate plastic balls (New York Plastics)	1, 2, 2.5, 3	1.28
Hardchrome steel balls (Jaygo)	1.0	7.8
Ignimbrite volcanic ash†		

* d_p = average particle diameter

** ρ_p = particle density

† from Mono Craters, Sierra Nevada, California

2.1.2. *Mesh Screen.* In configuration 2, the particle bed is mounted on a mesh screen. Stainless steel wire cloth (*Newark Wire Cloth Co.*), with openings slightly smaller than bead size, was used for this purpose. All wire cloths used had a porosity of about 50%.

The dense dusty flow generated in this facility, especially in configuration 2, has very high momentum, and the particles are carried over to the driven section at the end of the run. Thereby, the driven section has to be scavenged at the beginning of each run to ensure run repeatability. This problem is circumvented by mounting a strong retaining mesh screen at the diaphragm section, below the knife blades. This holds back the particles at the end of the run. Blunting of knife blades that could result from particle impact is also avoided by this device. Screen-free runs were used only in special cases to understand the resulting differences in flow characteristics.

2.2. Pressure Measurements.

Static and dynamic pressure measurement in the dusty gas was accomplished using fast-response piezoelectric pressure transducers (PCB 112A21). For static pressure measurement, the transducers were flush-mounted at the center of the side walls at various streamwise locations in the facility (Figures 2.2, 2.4). Flush-mounting results in a noisy pressure trace due to collisions and shearing of particles against the sensitive surface of the transducer. Dynamic pressure measurement was accomplished by designing a special probe and mounting transducers head on in the flow (§6.2).

The static pressure signal from the transducer T_w, located at the window center level is used as a reference in each experiment. The origin of time for all experiments corresponds to the arrival of the expansion fan at this transducer. Other static pressure transducers provide information about flow characteristics and test-time. The transducer traces are recorded on a digital oscilloscope (*Nicolet*

4094) and stored on floppy disks. The digital pressure data are analyzed for plotting on a PDP-11 computer by transferring from the oscilloscope via a GPIB interface.

The PCB 112A21 series transducers are highly sensitive dynamic devices, with a calibration of 726 mv/bar, a rise time of 2 μs and a large discharge time constant of 1 sec. These transducers are ideally suited for a dynamic experiment like the current one with a test-time of about 35 ms. The signal decay due to transducer discharge, during the course of the entire experiment, is extremely low. These transducers are quite rugged and can take a maximum pressure of about 70 bar and therefore were also convenient for measuring the dynamic pressure of the dense dusty flow.

2.3. Flow Visualization.

2.3.1. *Dense Dusty Flow.* The dense dusty flow was visualized using high-speed photography. Since large portions of these flows are opaque, front lighting was found most suitable for visualizing and documenting the flow features. The photographs record the back scattered light from the dusty medium moving adjacent to the front window wall. The events captured through flow visualization cannot in general be directly correlated with the local events as monitored by the pressure transducer T_w, since the latter is located a half channel width behind the front window. Two setups, i) single-picture photography and ii) motion-picture photography, were used.

2.3.1.1 Single-Picture Photography. High resolution pictures were obtained by taking single-flash photographs. Figure 2.5 shows the arrangement. At the start of the run, the room is darkened and the camera shutter is opened. After diaphragm rupture, an expansion fan passes the window transducer (T_w). The pressure signal, detected by the transducer, triggers the oscilloscope (*Nicolet* 4094) and is recorded on it in real time. A synchronous output trigger available on the oscilloscope is

used to trigger the microprocessor control (appendix A) which is software programmed to provide a suitable delay. At the end of the delay, the microprocessor control triggers a stroboscope (*GenRad* 1538A) which simultaneously triggers a stroboslave (*GenRad* 1539). The image of the dusty flow is thus recorded. The stroboscope and the stroboslave are set up for low frequency operation, generating a high intensity light pulse of 3 μs duration. The stroboslave is identical to the stroboscope in pulse characteristics, but it has no internal oscillator and thereby can only be triggered externally. In runs during which pressure traces were not recorded, a trigger generator circuit (appendix A) was employed to provide the necessary trigger to the microprocessor control.

Trial and initial setup photography was done using a Graphex camera (135 mm lens) with Polaroid 667 Landsat film. The magnification was 0.84 and aperture setting was f/8. Better pictures were obtained with a Nikon FE2 35 mm camera. Here, a Micro Nikkor 105 mm lens, with aperture setting of f/8 and a magnification of 0.28 was used. The film was Kodak Tmax (400 ASA) developed with HC-110 developer.

2.3.1.2 Motion-Picture Photography. The general flow of events and details such as speed of the particulate material were best recorded by high-speed motion-picture photography. The arrangement is shown in Figure 2.6. Six 1000 watt lamps provide the front lighting. The motion picture camera was a 16 mm full-frame HYCAM II Model 410064 (*Red Lake Corp.*) fitted with a Canon 18 - 108 mm lens.

Kodak 7224 4X negative (400 ASA) film was found to be the most suitable for the present studies. Two framing speeds were used: 6000 frames per second (fps) with a 100 ft spool and 8000 fps with a 200 ft spool, both with a 1/2.5 framing shutter. The lens aperture was set at f/5.6. Most motion pictures were made at 6000 fps for it provided a good tradeoff between cost and speed while using glass

beads as the bed medium. 8000 fps was used to obtain higher temporal resolution motion pictures. These had to be push processed one stop for good results.

For motion-picture photography, the camera triggers the experiment. A run is started by first pressurizing the driver close to diaphragm burst pressure. The flood lights are then turned on and the camera is started. When the camera reaches the preset framing speed, the event synchronizer pulse from the camera triggers the solenoid valve which in turn connects the test section to a small high pressure reservoir. The pressure in the driver rises until the diaphragm ruptures. The pressure sensed by the window transducer, T_w, is recorded by the oscilloscope. The synchronous trigger from the oscilloscope triggers the microprocessor control which is programmed to deliver five pulses of 20 μs duration at 5000 Hz. These timing pulses are fed into a light emitting diode located in the camera along the film track. This marks the edge of the film and serves as a reference for start of the experiment. In the HYCAM, the picture image leads the timing light signal by five frames. Frame-by-frame analysis of the motion picture information was accomplished using a photo-optical data analyzer (*L W International*).

2.3.2. *Dilute Dusty Flow.* Very dilute dusty flow such as the one generated using short beds (§5.8.1) was best visualized using only backlighting in both single-picture and motion-picture photography. The working beads were darkened with flat-black spray paint and then dried before being put to use.

2.4. Run conditions.

Table 2.2 lists the details of the run conditions for the experiments discussed in the chapters that follow. A run number is used to identify a particular set of operating conditions, namely, a bed of initial height l_0, which is composed of particles of size d_p, and is loaded in configuration 1 or 2 and lofted from a distance L below the window center at a diaphragm burst pressure, P_0. The nature of studies conducted in a particular run set up is also mentioned. Runs 1 - 8 were

made in configuration 1, and runs 9 - 29 were made in configuration 2. Runs 2 - 24 were made with a retaining screen at the diaphragm section. Runs 21 - 24 were made with the dynamic pressure probe mounted in the dusty gas flow. Runs 25 - 27 were made with beds initially stacked with a gradient in particle size. Runs 28 and 29 were made with beds initially stacked with a gradient in particle density. The operating pressure for runs 3 - 5, 9 - 23 and 25 - 29 is approximately 2 bar.

Table 2.2. Details of the Run Conditions

Run	P_0^* bar	L^{**} cm	$l_0^\dagger$ cm	l_0/D	$d_p^\ddagger$ mm	l_0/d_p	Confgn.#	Studies
1a	3.1	0.0	60.0	15.8	0.125	4800	1	Pressure survey above and within the bed,
1b	3.1	-5.7	60.0	15.8	0.125	4800	1	bed expansion (flow visualization)
2	3.1	0.0	60.0	15.8	0.125	4800	1	Pressure history above the bed, with retaining screen at top, bed expansion (flow viz.)
3	2.0	-4.5	17.0	4.5	0.25	680	1	Effect of bed height (flow viz.)
4	2.0	-5.1	15.2	4.0	0.18	847	1	Occurrence of partitions
5	2.0	-4.5	17.0	4.5	0.5	340	1	Occurrence of partitions
6	3.1	0.0	60.0	15.8	0.25	2400	1	Effect of particle size (flow viz.)
7	3.1	0.0	60.0	15.8	0.5	1200	1	Effect of particle size (flow viz.)
8	1.3	0.0	60.0	15.8	0.25	2400	1	Effect of burst pressure (flow viz.)
9	2.1	3.8	8.9	2.3	0.25	356	2	Pressure history above the bed
10a	2.0	22.5	7.6	2.0	0.18	422	2	flow viz: expanded and elongated bubble
10b	2.0	32.5	7.6	2.0	0.18	422	2	flow viz: filamentary structure
11	1.9	17.8	5.1	1.3	0.25	204	2	Pressure survey in the flow field
12	2.0	16.0	5.7	1.5	0.18	317	2	bubble growth and bed expansion (pressure history and flow viz.)
13	2.0	42.5	7.6	2.0	0.18	422	2	dusty flow: ($x-t$ diagram, flow viz., intensity measurement)
14	2.0	20.0	8.5	2.2	0.18	472	2	motion of a buoyant bubble (flow viz.)
15	2.0	12.5	9.5	2.5	0.18	528	2	effect of bed height (flow viz.)
16	2.0	-29.2	11.4	3.0	0.5	228	2	Growing bubbles (Figure 7.1)
17	2.0	-29.2	11.4	3.0	0.25	456	2	Incomplete flow head (Figure 7.1)
18	2.0	-33.0	15.2	4.0	0.18	847	2	Flow head (Figure 7.1)
19	2.0	0.0	6.3	1.7	0.09	700	2	effect of particle size (flow viz.)
20	2.0	75.0	1.25	0.3	0.5	25	2	late stages of bed expansion (flow viz.)

Run	P_0^* bar	L^{**} cm	$l_0^\dagger$ cm	l_0/D	$d_p^\ddagger$ mm	l_0/d_p	Confgn.#	Studies
21	2.0	30.5	5.1	1.3	0.25	204	2	probe pressure history: dense dusty gas flow
22	2.0	12.7	5.1	1.3	0.25	204	2	total pressure history: expanding bed
23	2.0	51.0	2.5	0.7	0.25	100	2	total pressure history: approach to uniformity
24	4.0	61.0	1.25	0.3	0.25	50	2	total pressure history: mass loading estimate
25	2.1	-1.9	3.8	1.0	0.25, 0.5, 0.75		2	Effect of acceleration gradient: stable lofting flow viz., pressure history
26	2.1	-0.8	5.0	1.3	0.25 0.5		2	Stable lofting: effect of bed height (flow viz.)
27	2.1	-1.9	3.8	1.0	0.25, 0.5, 0.75		2	Effect of acceleration gradient: unstable lofting (flow viz., pressure history)
28	2.1	-1.9	3.8	1.0	1.0	38	2	Effect of acceleration gradient: (particle density) stable lofting
29	2.1	-1.9	3.8	1.0	1.0	38	2	Effect of acceleration gradient: (particle density) unstable lofting

* P_0 = diaphragm burst pressure
** L = distance below window center to bed top
† l_0 = initial bed height
‡ d_p = particle size
# initial loading configuration of the bed (*cf.*§2.1)

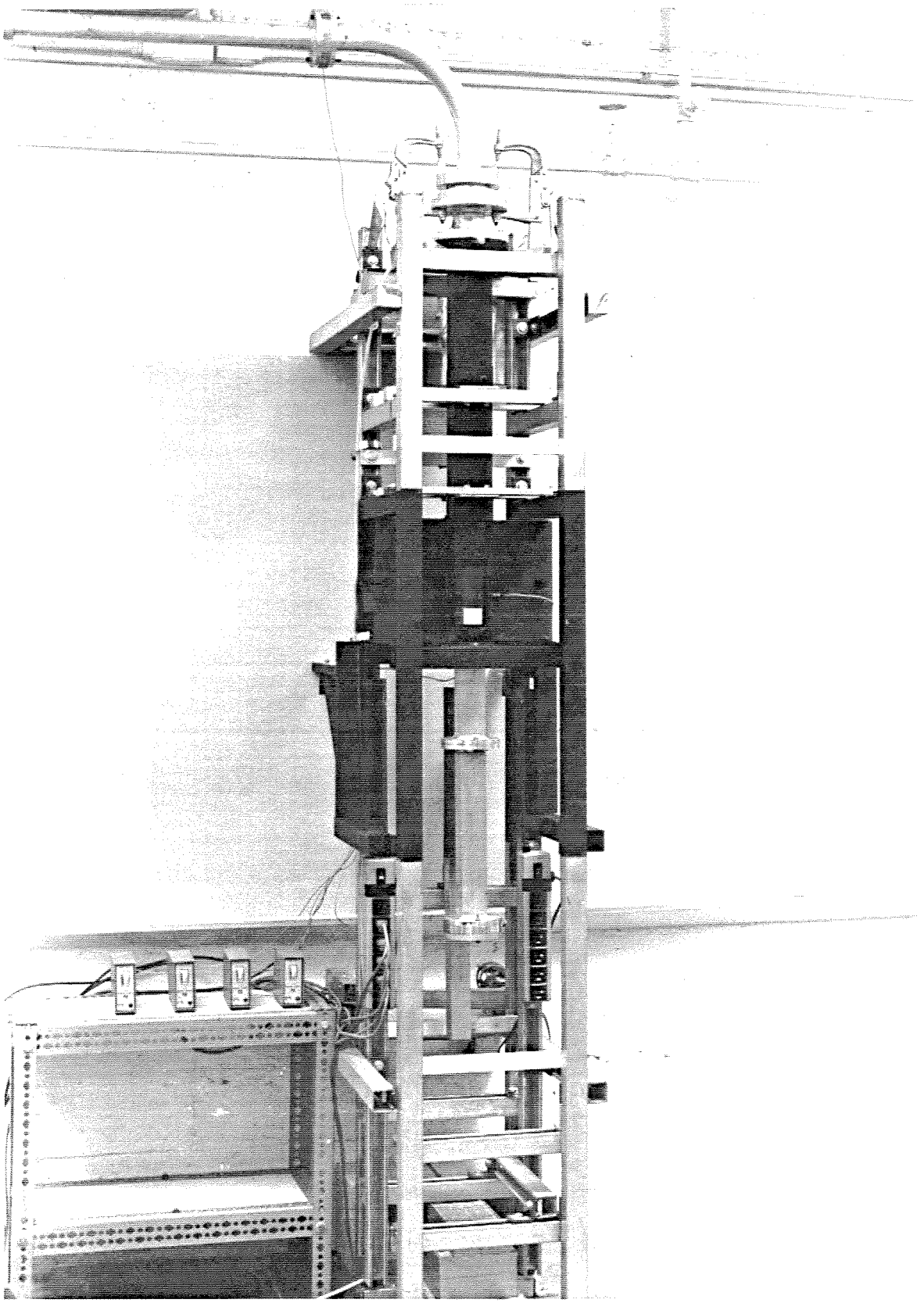

Figure 2.1 Dense dusty gas facility: configuration 1.

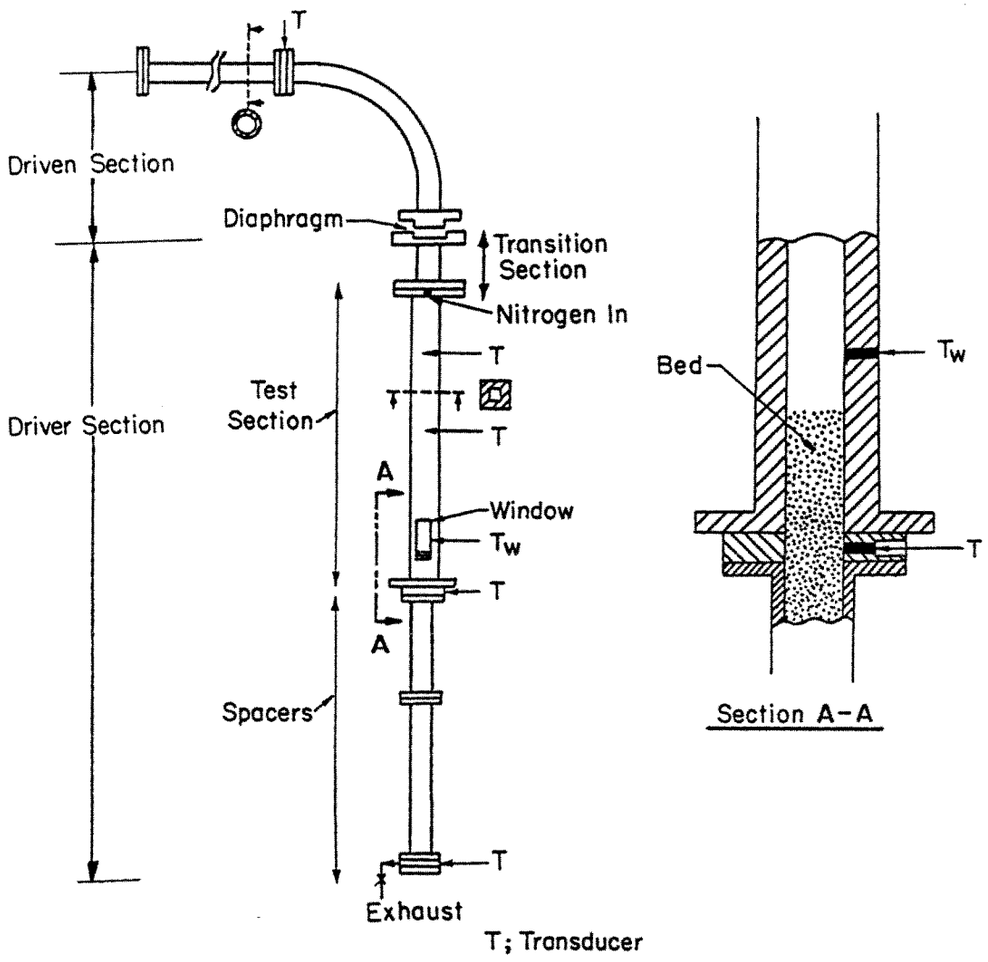

Figure 2.2 Schematic of configuration 1.

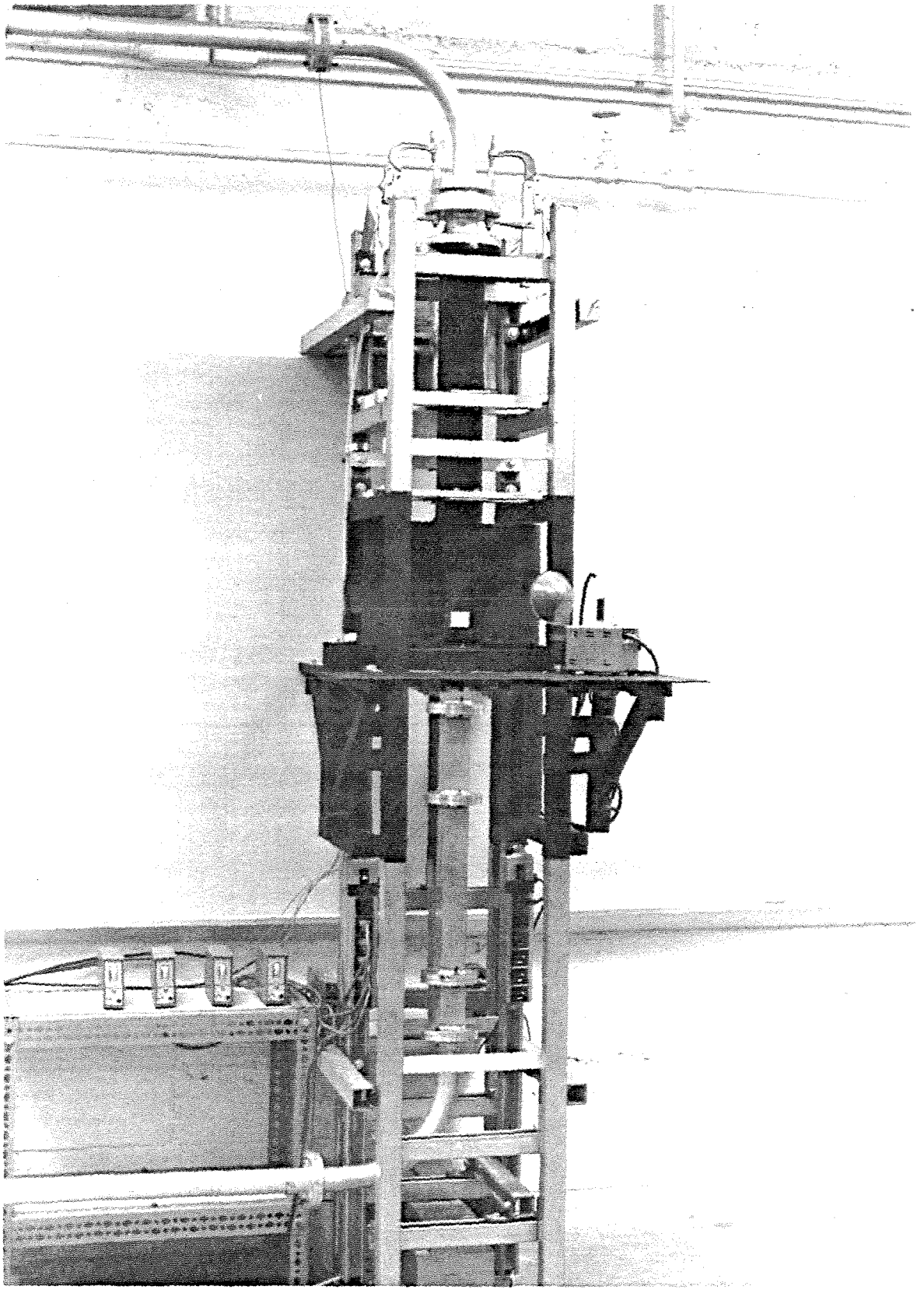

Figure 2.3 Dense dusty gas facility: configuration 2.

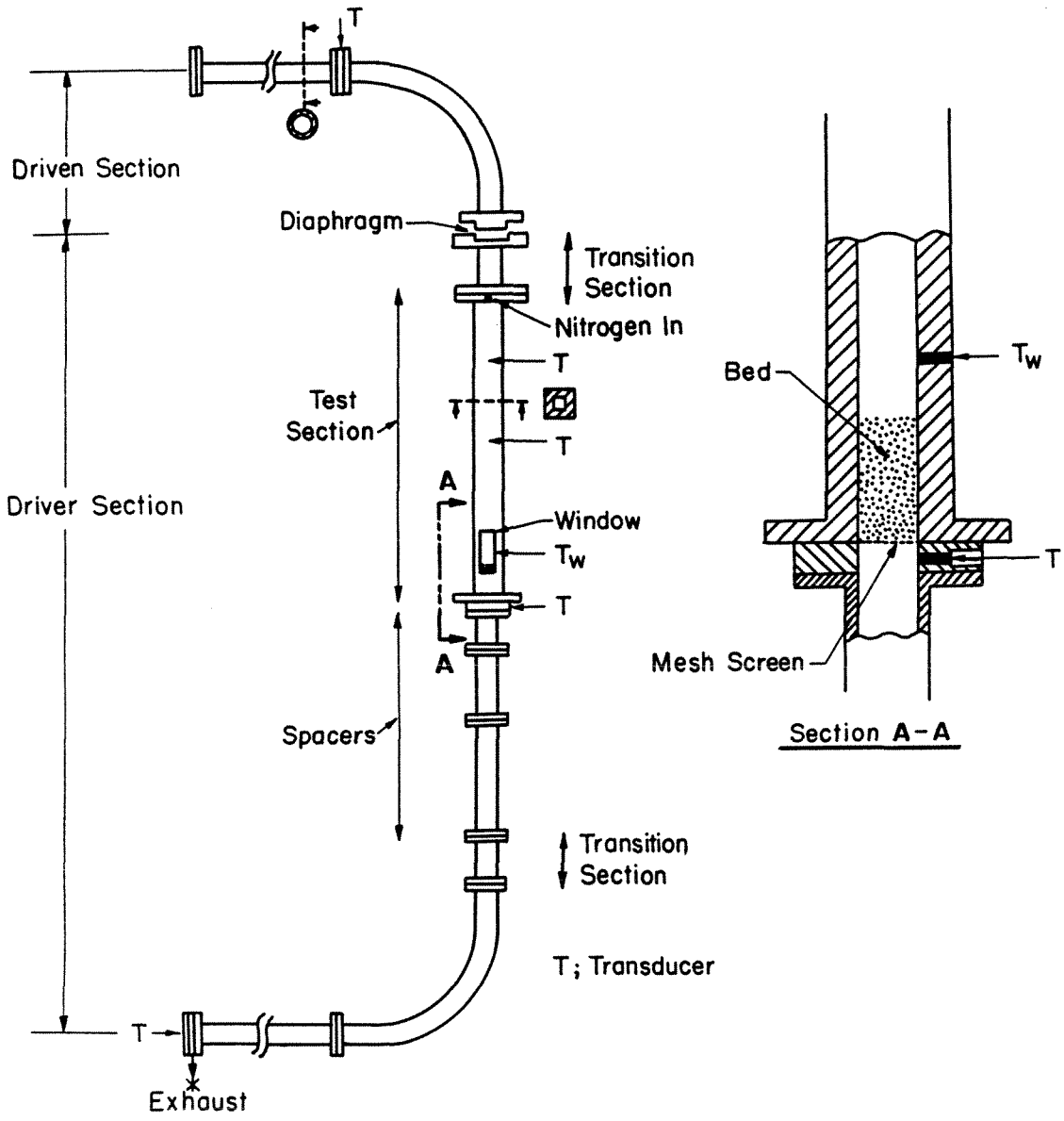

Figure 2.4 Schematic of configuration 2.

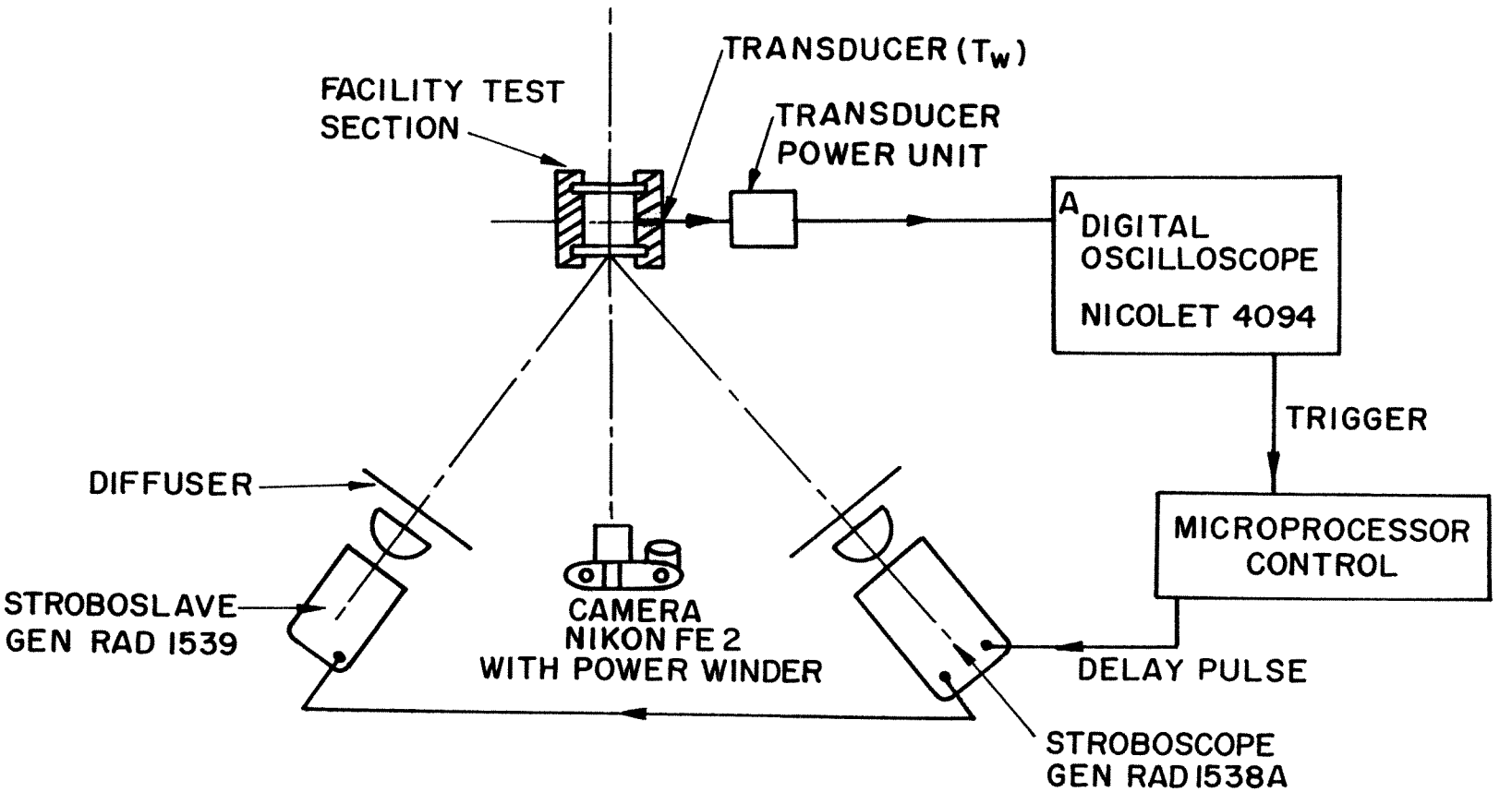

Figure 2.5 Top view of optical arrangement and instrumentation for single-picture photography.

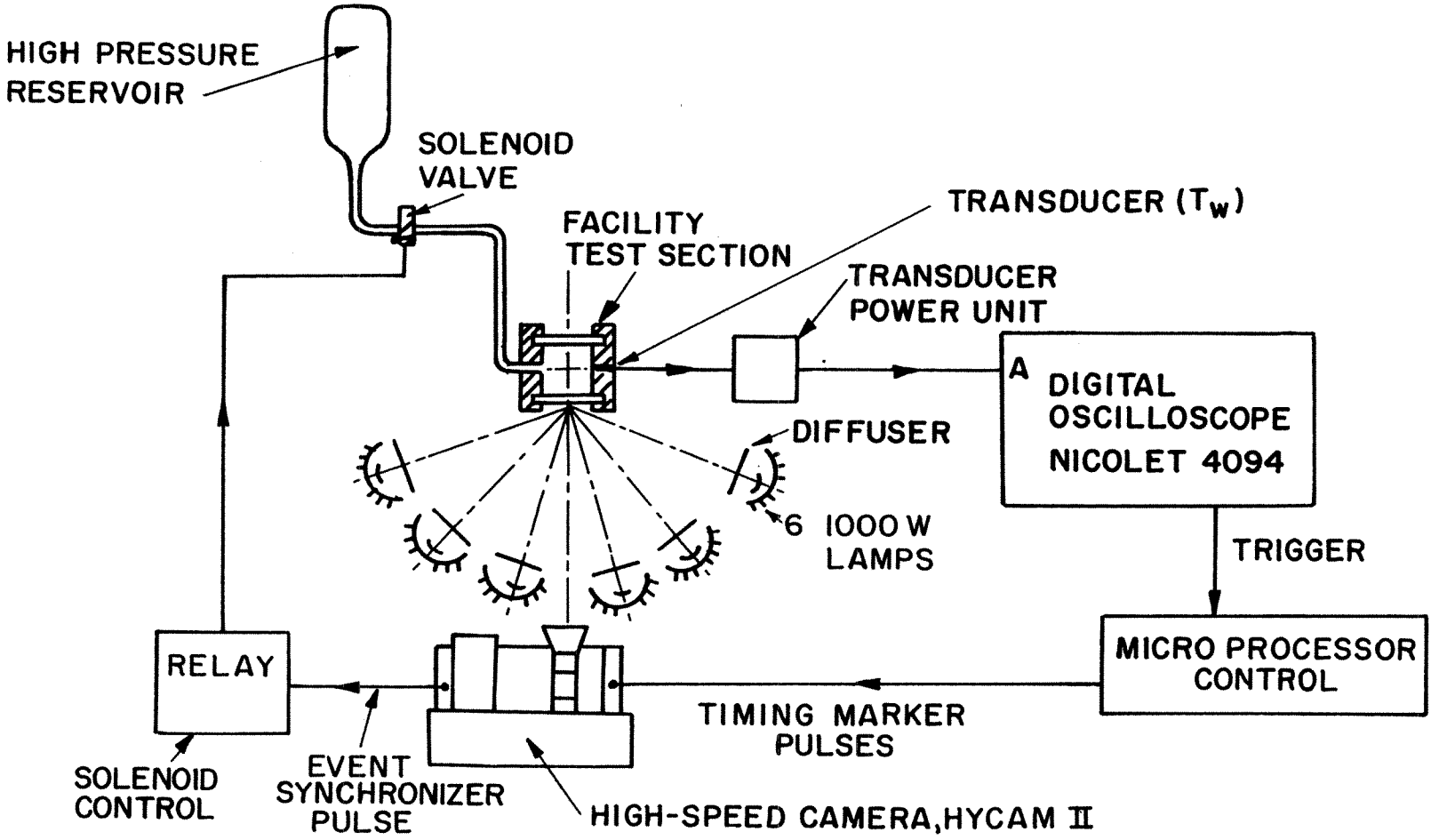

Figure 2.6 Top view of optical arrangement and instrumentation for motion-picture photography.

Chapter 3

RAPID DEPRESSURIZATION EXPERIMENTS: CONFIGURATION 1

3.1. Introduction.

These experiments were done with moderate-to-long beds ($4 < l_0 / D < 16$) resting on the bottom of a short driver section (Figures 2.1, 2.2). Dense dusty flow is generated here by the rapid depressurization of the gas within the bed. When diaphragm ruptures, an expansion fan moves down the tube. On striking the bed, the expansion fan reflects from it and transmits through it. The portion that is transmitted rapidly depressurizes the gas within the bed. As the gas within the bed is accelerated, it drags the particles along, generating an accelerating and expanding dense dusty flow. Single-flash pictures and high-speed motion pictures were used to study the flow. Glass beads 0.125 mm, 0.25 mm and 0.5 mm in dia, and their mixtures, were used in the experiments. The diaphragm burst pressures were 2.0 and 3.1 bar.

It is observed that, right from the onset, the dusty gas flow field is highly nonuniform. The bed expansion initially occurs along horizontal fractures which grow into bubbles with a honeycomb pattern. The extent of bed expansion depends on the original height of the bed.

3.2. Results: Run 1a.

Run 1a corresponds to a set of identical runs for a 60 cm deep bed of 0.125 mm glass beads, with the top of the bed initially located at the center of the window and the diaphragm burst pressure being 3.1 bar. The results for Run 1a have been presented in terms of: i) pressure histories above and within the bed, ii) $x-t$ diagram and iii) flow visualization. The origin of time for all the runs corresponds to the arrival of the incident expansion fan at the window transducer T_w (Figure 2.2).

3.2.1. *Pressure Traces.* Figure 3.1 is a pressure history recorded at a point 38 cm above the bed. The strength of the incident expansion fan (1 - 1′) is 1.95. The expansion fan is about 2.8 ms thick when it arrives at the bed. It generates fluid speeds of approximately 160 m/s before reflecting from the bed (appendix C). The strength of the reflected fan (2 - 2′) is 1.88. The difference in the two strengths implies an upward gas velocity of about 7.5 m/s just after reflection. The small pressure rise (3 - 3′) in Figure 3.1 is due to i) accelerated motion of the bed, ii) fluid leakage across the bed, and iii) transducer discharge. This test is terminated by the arrival of the reflected shock wave (4 - 4′) from the top end of the facility. 5 - 5′ is the reflection of this shock wave from the surface of the expanded bed.

Figure 3.2 is a pressure survey made at transducer locations 7.5 cm (trace A), 12.5 cm (trace B) and 60 cm (trace C) below the initial location of the top of the bed for Run 1a. The expansion wave disperses and weakens as it transmits through the bed. The average speed of the leading edge of the wave in the first four bed widths of travel is about 88 m/s. Quasi-steady through flow conditions are established quickly behind the expansion wave.

The weakened expansion wave reflects from the bottom end wall, and this results in a further drop in pressure as is evidenced by the pressure at the bottom transducer location (trace C) going below that of the others (traces A & B) at 35 ms and onwards. The reflected expansion wave decelerates the bed fluid. It gets highly attenuated in transit along the bed, and its effects are not seen at the top bed locations, as is evident from traces A and B. In a shorter bed the reflected expansion wave is stronger, and its deceleration effects are felt throughout the bed (§3.4)

3.2.2. *x-t Diagram.* Figure 3.3 is an $x-t$ diagram summarizing the behaviour for Run 1a. It has been constructed from transducer records, and flash photographs from several different experiments. The bed expansion data have been listed in

Table 3.1. The diagram shows the leading edge of the incident expansion fan that switches on the flow, the reflected shock wave that terminates the test, and the motion of the bed top. Particles close to the top of the bed experience an average acceleration, a_p, of 275 g in the first five milliseconds following the arrival of expansion fan and reach asymptotic speeds of 15 m/s. As the wave slowly disperses and weakens while transmitting through the bed, the lower bed layers are accelerated to lower speeds and, in fact, the bottom layers of the bed do not loft.

3.2.3. *Flow Visualization.* Figure 3.4 is a sequence of flash photographs showing the different stages of bed expansion for Run 1a. These pictures represent different experiments run with the same operating conditions. Figure 3.4a shows the initial position of the bed with the top at the center of the window. The bottom is 60 cm below. Figures 3.4b-e reveal the flow morphology during the expansion of the bed. Right from the onset, the flow is highly nonuniform.

The initial bed expansion occurs along horizontal fractures (Figure 3.4b) that apparently are a consequence of an inherent instability of high-density particle systems. The fractures partition the bed into slabs, each a few particle diameters thick. The dominant fractures, resulting from merger of shorter adjacent fractures, span the channel (Figure 3.4c). In the next stage, the fractures grow vertically. During the acceleration phase of bed expansion, particles rain down from the bottom surfaces of the slabs partitioning the fractures into bubbles with a characteristic honeycomb pattern (Figure 3.4c, d, e). This observed instability of the bottom surfaces of the slabs is analogous to the Rayleigh-Taylor instability observed in continuous media. The top surfaces of the slabs however are stable and retain their integrity. Assuming that the fracture partitions grow at a rate $f = \alpha/2\ a_p t^2$ (f = fracture size), the observed growth of 8 mm in 4 ms, at 275 g in the top regions of the bed, suggests that the value of the empirical constant α is about 0.2. Figure 3.5 is an idealized schematic of the dominant fractures showing the expansion route of the bed.

In the third stage of bed expansion, bubbles in a horizontal layer compete with each other; dominant bubbles grow (Figures 3.4d, e), bubbles fuse, and finally they penetrate the thinning roofs of the slabs (see §3.4). The resulting dusty flow has a fibrous appearance (Figure 3.4f). [In Figure 3.4f, the bed top is initially at the bottom of the window (Run 1b)]. In general, bubbles show unbounded growth, and often grow to span the channel (Figure 3.4g, h).

3.3. Operation With Retaining Screen.

The results presented in §3.2 (Runs 1a) were obtained with no retaining screen mounted at the diaphragm section to hold back the particles at the end of the run. It is however convenient to mount a screen below the knife blades (§2.1.2) and thus avoid the necessity of scavenging the driven section of the facility at the beginning of every run. Operating the experiments in this configuration leads to differences from experiments run with no retaining screen. Figure 3.6a is a pressure history monitored 38 cm above the same 60 cm deep bed of 0.125 mm glass beads, now with a 145×145 steel mesh at the diaphragm section (Run 2). A weaker expansion fan (1 - 1′) of strength 1.49, resulting from the choking of the screen, transmits towards the bed and reflects (2 - 2′) from it. A re-reflection from the retaining screen and return (3 - 3′, 4 - 4′), followed by another re-reflection and return (5 - 5′, 6 - 6′), is necessary to complete the expansion above the bed, and this takes a total of 10 ms following the arrival of the incident expansion fan at the bed.

The bed accelerations and speeds, and consequently the bed expansion, realized are lower than those while operating without the retaining screen. Figure 3.6b is the $x-t$ diagram showing the incident and reflected expansion fans and the bed expansion. The $x-t$ diagram has been constructed from transducer records, and flash photographs from several different experiments. The bed expansion data have been listed in Table 3.2. The average acceleration at the bed top in the first five milliseconds is 175 g, and the top layers of the bed reach asymptotic speeds of 13.5 m/s. The bed expansion in the first ten milliseconds is 9 cm, and this is 75% of

that realized while operating without the screen (Run 1).

3.4. Effect Of Bed Height.

The shorter the bed, the smaller the volume of fluid contained in it and, consequently, the lower the bed expansion. In shorter beds, the deceleration effect resulting from the reflection of the transmitted expansion wave from the bottom end of the driver section is strong, and this retards the bed expansion.

Figure 3.7a is a sequence of prints, selected every sixth frame, from a 6000 fps high-speed motion picture of a 17 cm deep bed ($l_0 / D = 4.5$) of 0.25 mm glass beads operated at 2 bar burst pressure (Run 3). Top bed layers reach speeds of 7.5 m/s, and the average initial acceleration is 150 g. Features typical of the Rayleigh-Taylor instability of continuous media are observed in the upper regions of the bed here. This includes partitioning of fractures into bubbles (5 - 9 ms), competition and interaction between bubbles (10, 11, 12 ms), growth of the dominant bubble (13, 14, 15 ms), bubble penetration of a thinning roof and subsequent bursting (16, 17 ms).

Figure 3.7b is an $x-t$ diagram showing the expansion in the upper regions of the bed for Run 3. It has been constructed from the sequence of prints presented in Figure 3.7a. The bed expansion data have been listed in Table 3.3. Traces 1 - 6 represent the motion of the top of the bubbles. There is no upward drift of the bubbles along the bed, since accelerations operate only at small times. The bed expands by about 9 cm in the first 15 ms. The subsequent bed expansion is slowed down by the arrival of the reflected expansion fan from the bottom end of the driver section.

3.5. Effect Of Particle Size.

Varying particle size in the range 0.125 - 0.5 mm had little effect on bed speeds. If the particle size were the characteristic length scale in the problem, then the characteristic time scale in the problem should also depend on particle size to

yield the above result.

The flow structure corresponding to different particle sizes exhibits interesting differences. Figure 3.8 a, b, c show an early time comparison for similar beds with 0.125, 0.25 and 0.5 mm glass beads under the same operating conditions (Run 2, 6, 7) and at 6.3 ms after the arrival of the expansion fan. The thickness of the slabs (s) increases with particle size. As compared with 0.125 mm particles (Figure 3.8a), the the fractures for the 0.5 mm particles (Figure 3.8c) are wider and longer. With even larger particles, individual fractures could eventually span the channel. Figure 3.8d shows an expanded bed made of a mixture of equal volumes of 0.125, 0.25 and 0.5 mm glass beads and operated at the same conditions as the monodisperse beds. The mixture bed also expands along horizontal fractures much the same way as monodisperse beds, and its fracture characteristics resemble the intermediate 0.25 mm beads. Table 3.4 lists the thickness of the slabs for various diaphragm burst pressures and particle sizes. The mean thickness of the slabs, and the standard deviation for the selected sample sizes have been tabulated. It is apparent that the slab thickness is a characteristic of particle size, and is not dependent on other operating conditions. The slab thickness seems to be proportional to the square root of particle size; a result which is not understood.

The second stage of expansion, *viz.* partitioning of the fractures into bubbles, occurs earlier for smaller beads (Figure 3.8 a, b, c). Table 3.5 lists the time τ following the arrival of the expansion fan at the bed, when the fractures are completely partitioned into distinct bubbles. The data have been drawn from the motion pictures of the flow. τ seems to be the characteristic time scale in the problem. The initial span of the bubbles is related to particle size. Table 3.6 lists the initial bubble width for different runs. Interestingly, the initial width of the bubbles is about 25 particle diameters. The bubbles eventually compete, and the dominant ones prevail. However, in general, beds with smaller particles show more nonuniformities owing to the smaller scales of the nonuniformities. This is especially true at late times (Figure 3.9 a,b,c).

Table 3.1. Data for $x-t$ Diagram: Figure 3.3

t (ms)	S (mm)*
0	0.0
2.8	17.0
4.0	32.1
5.2	48.4
6.5	66.3
7.6	81.6
9.0	101.7

* S = displacement

Table 3.2. Data for $x-t$ Diagram: Figure 3.6b

t (ms)	S (mm) *
0	0.0
2.5	12.4
3.8	22.5
5.0	31.8
6.3	44.6
7.5	58.8
8.8	75.1
10.0	90.6

* S = displacement

Table 3.3. Data for $x-t$ Diagram; Figure 3.7b

t (ms)	S (mm)*					
	1 †	2	3	4	5	6
1	0.0	-	-	-	-	-
3	10.0	-	-	-	-	-
4	16.3	-	-	-	-	-
5	22.5	-	-	-	-	-
6	28.7	-	-	-	-	-
7	36.6	-	-	-	-	-
8	43.3	-	-	-	-	-
9	51.2	-	-	-	-	-
10	58.2	38.7	18.3	10.8	-9.2	-
11	65.3	45.8	24.5	17.5	-2.9	-10.8
12	72.8	52.4	30.8	23.5	2.9	-5.0
13	80.7	59.9	38.3	30.8	9.2	1.3
14	87.4	68.2	46.2	38.3	15.4	7.0
15	94.0	74.0	52.0	43.7	20.8	12.9
16	101.9	79.0	58.2	48.3	27.3	17.9
17	105.3	83.2	61.6	51.6	30.8	20.8

* S = displacement

† point representing top of the bubble (cf. Figure 3.7a)

Table 3.4. Fracture Characteristics : Slab Thickness

Run *	P_0 (bar)**	d_p (mm)†	s (mm)‡			$\frac{s}{\sqrt{d_p}}$
			mean	std. devn.	sample	
8	1.3	0.25	3.9	0.26	20	7.8
3	2.0	0.25	4.0	0.28	10	8.0
6	3.1	0.25	3.9	0.18	20	7.8
1, 2	3.1	0.125	2.8	0.16	15	7.9
7	3.1	0.5	5.8	0.23	10	8.2

* cf. Table 2.2
** P_0 = diaphragm burst pressure
† d_p = particle size
‡ s = slab thickness

Table 3.5. Fracture Characteristics : Partitioning Time

Run *	P_0 (bar)**	d_p (mm)†	τ (ms)‡	τ/d_p
4	2.0	0.18	4.6	25.5
3	2.0	0.25	6.0	24.0
5	2.0	0.5	10.4	20.8

* cf. Table 2.2
** P_0 = diaphragm burst pressure
† d_p = particle size
‡ τ = time at which fractures are completely partitioned into bubbles

Table 3.6. Fracture Characteristics : Initial Bubble Width

Run *	d_p (mm) †	w (mm) ‡			$\frac{w}{d_p}$
		mean	std. devn.	sample	
1, 2	0.125	3.1	0.17	25	24.8
3, 6, 8	0.25	6.2	0.20	15	24.8
7	0.5	12.2	0.42	10	24.4

* cf.Table 2.2

† d_p = particle size

‡ w = initial bubble width

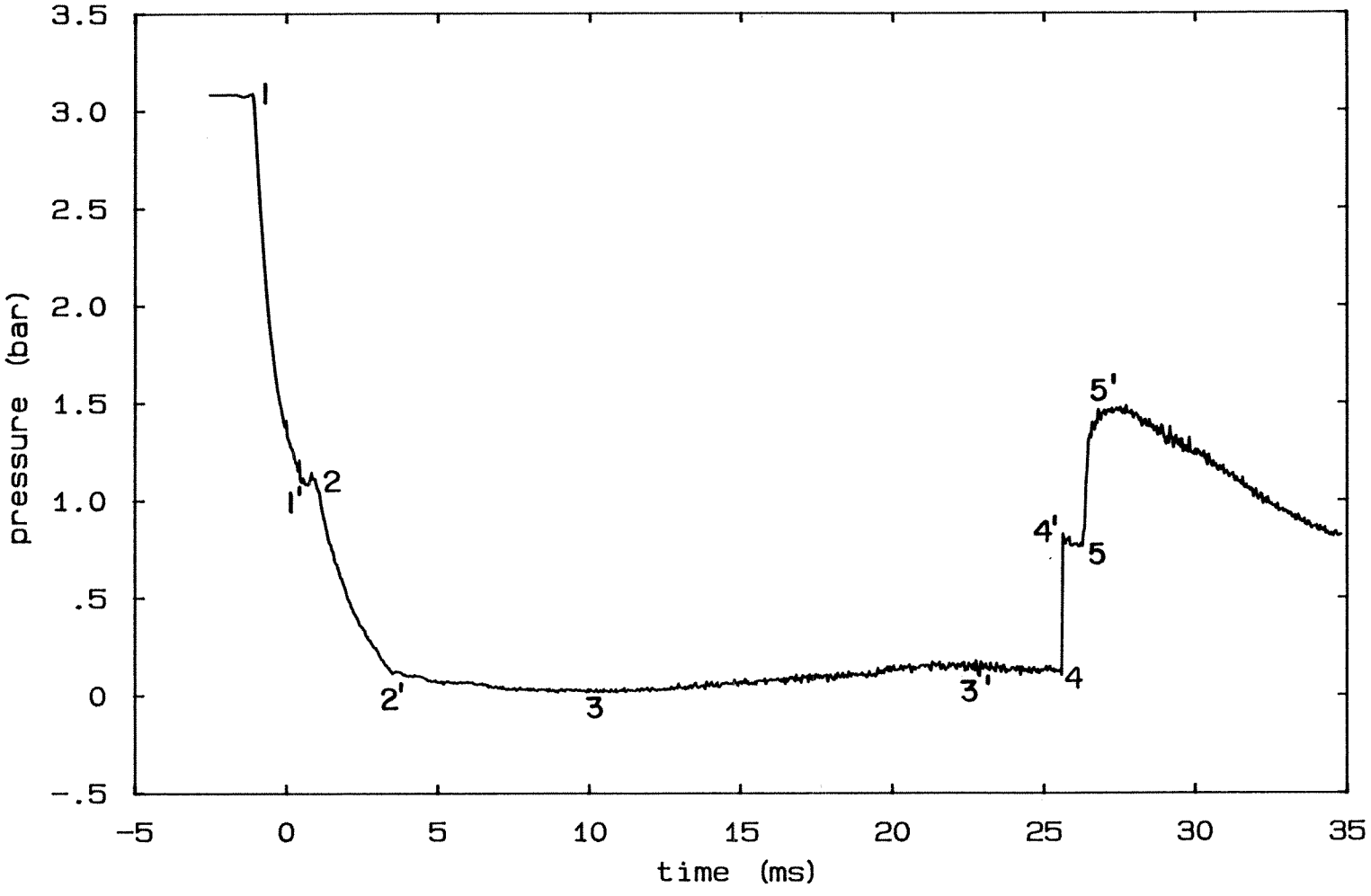

Figure 3.1 Pressure history 38 cm above bed (Run 1).

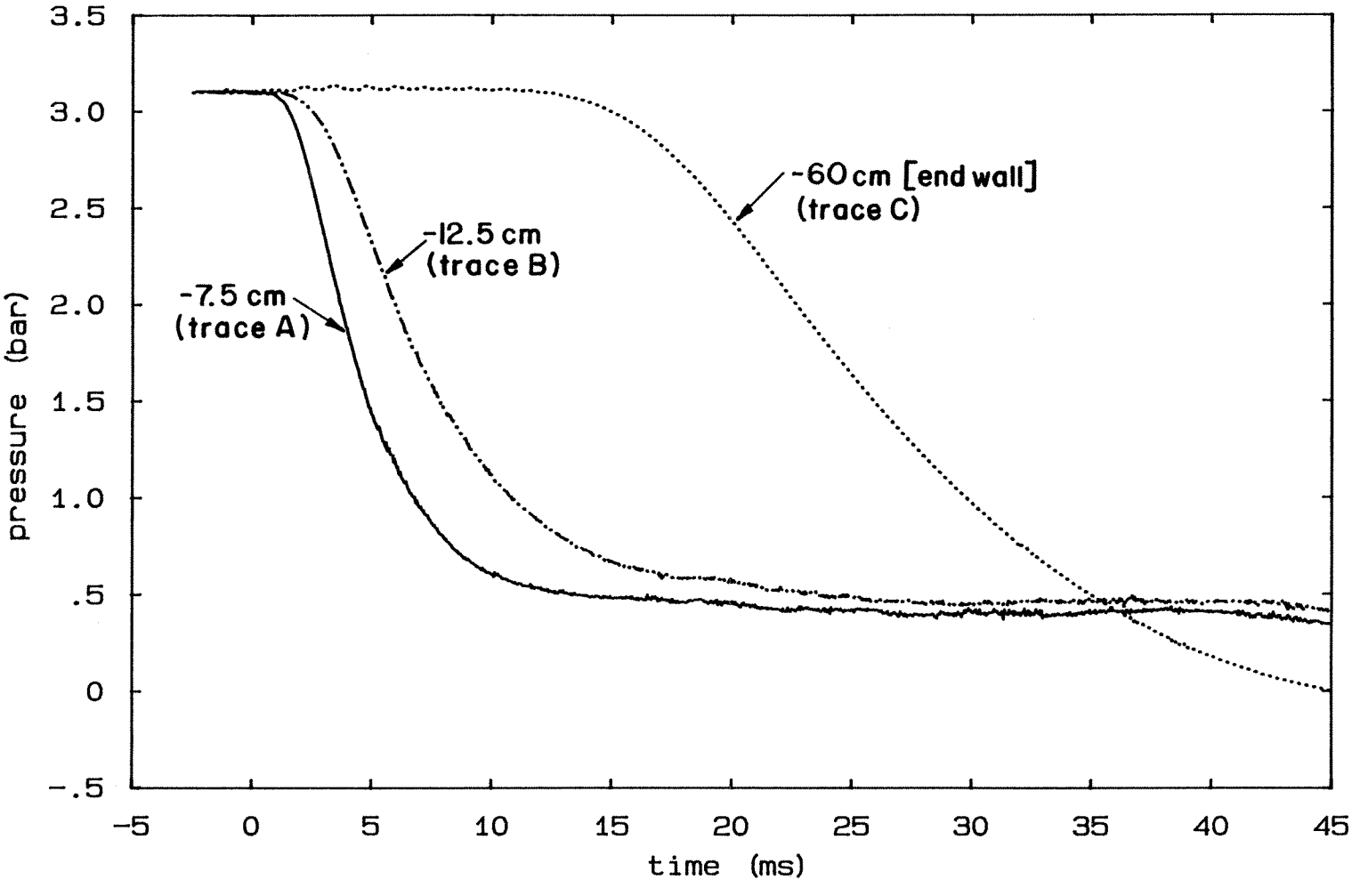

Figure 3.2 Pressure survey within the bed (Run 1).

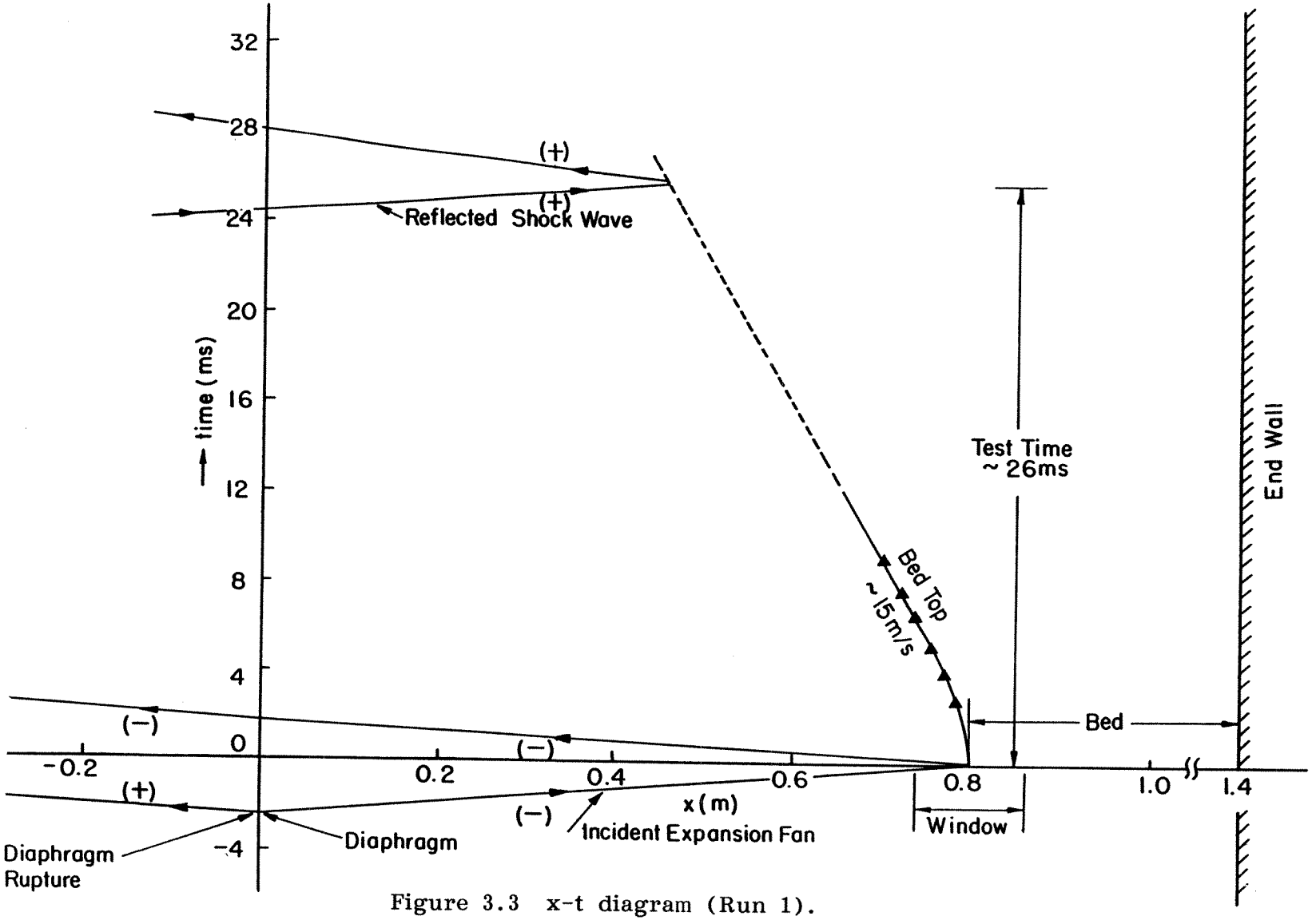

Figure 3.3 x-t diagram (Run 1).

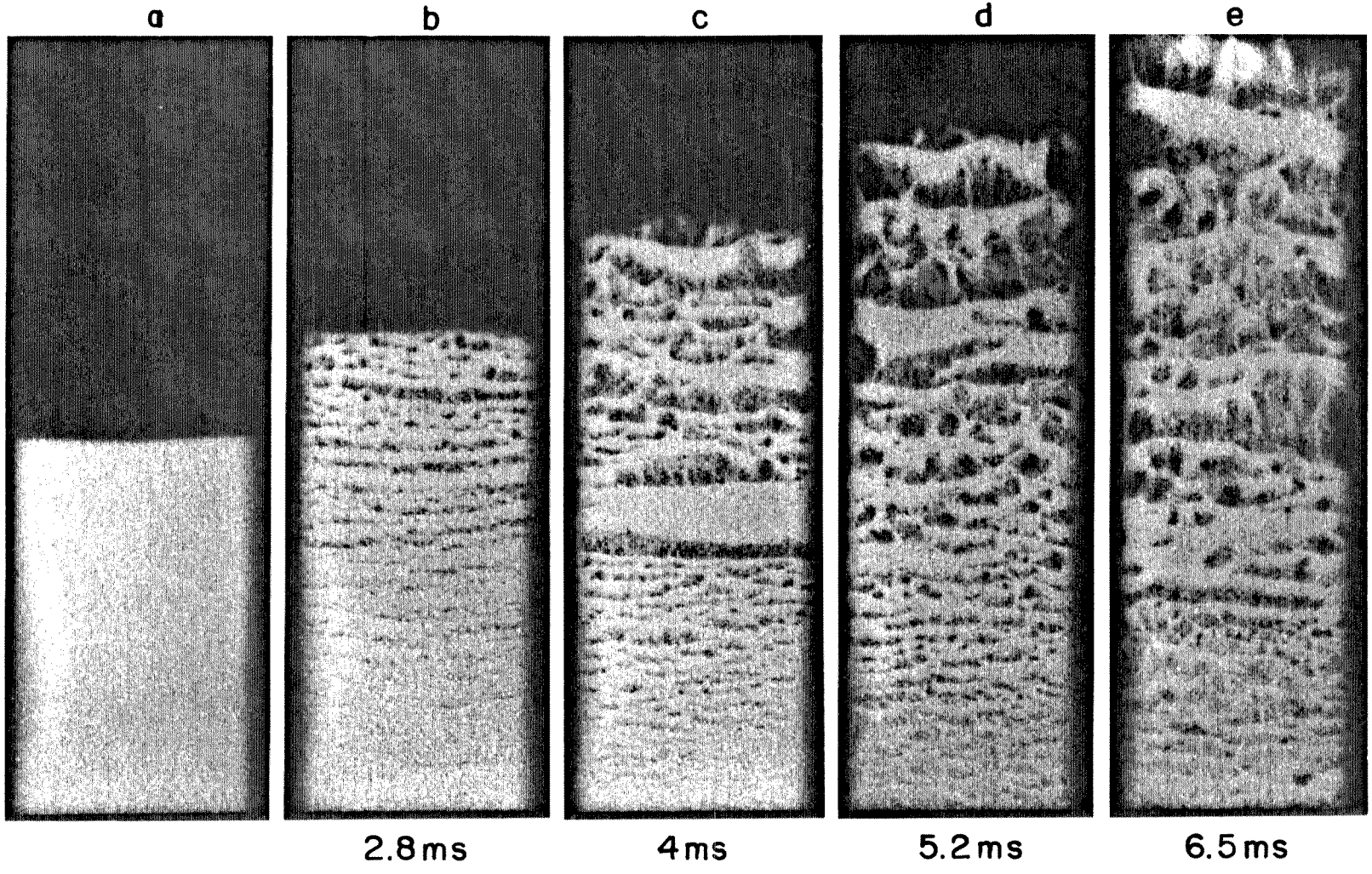

Figure 3.4 Rapid depressurization of the bed (Run 1): single-flash photographs.

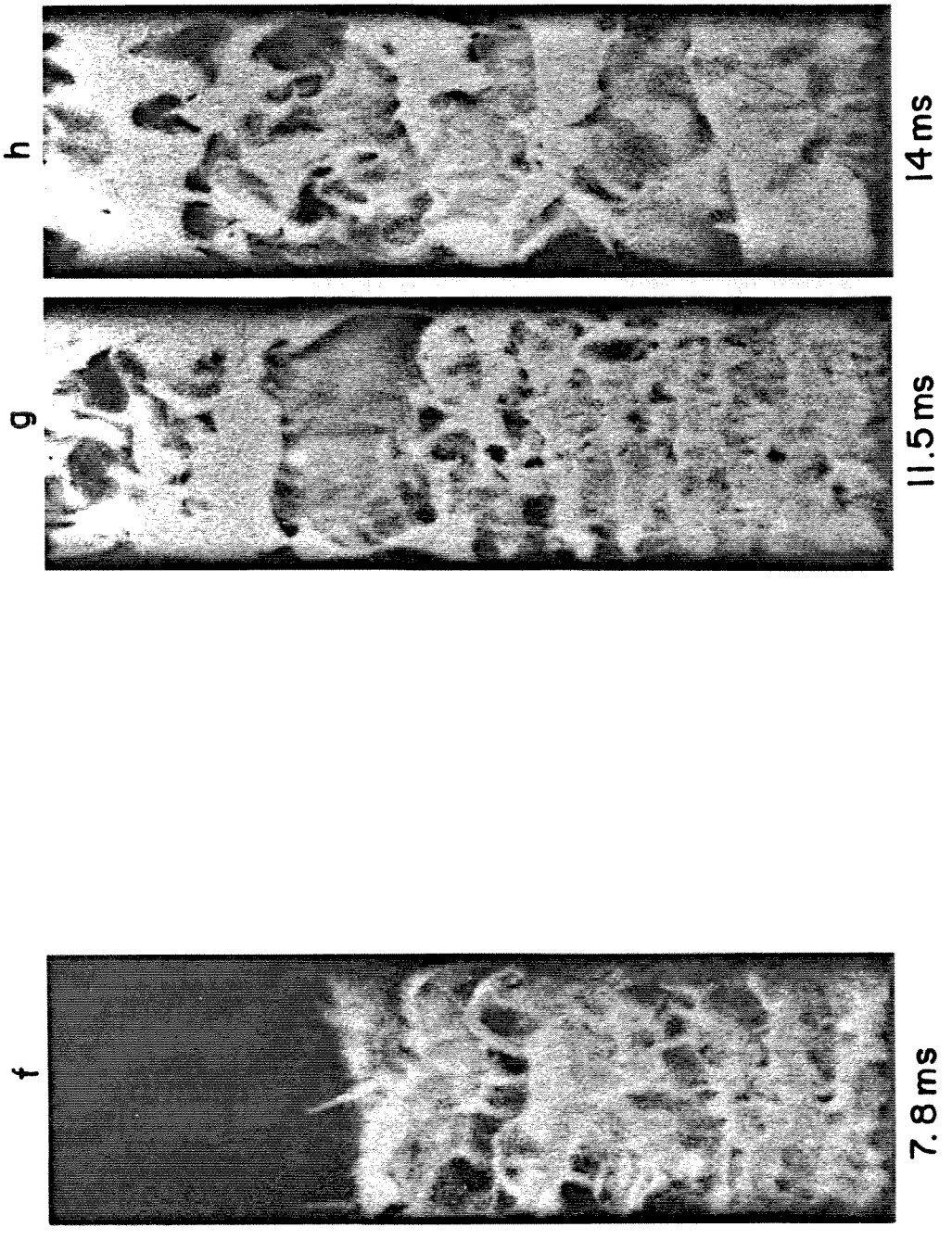

Figure 3.4 continued

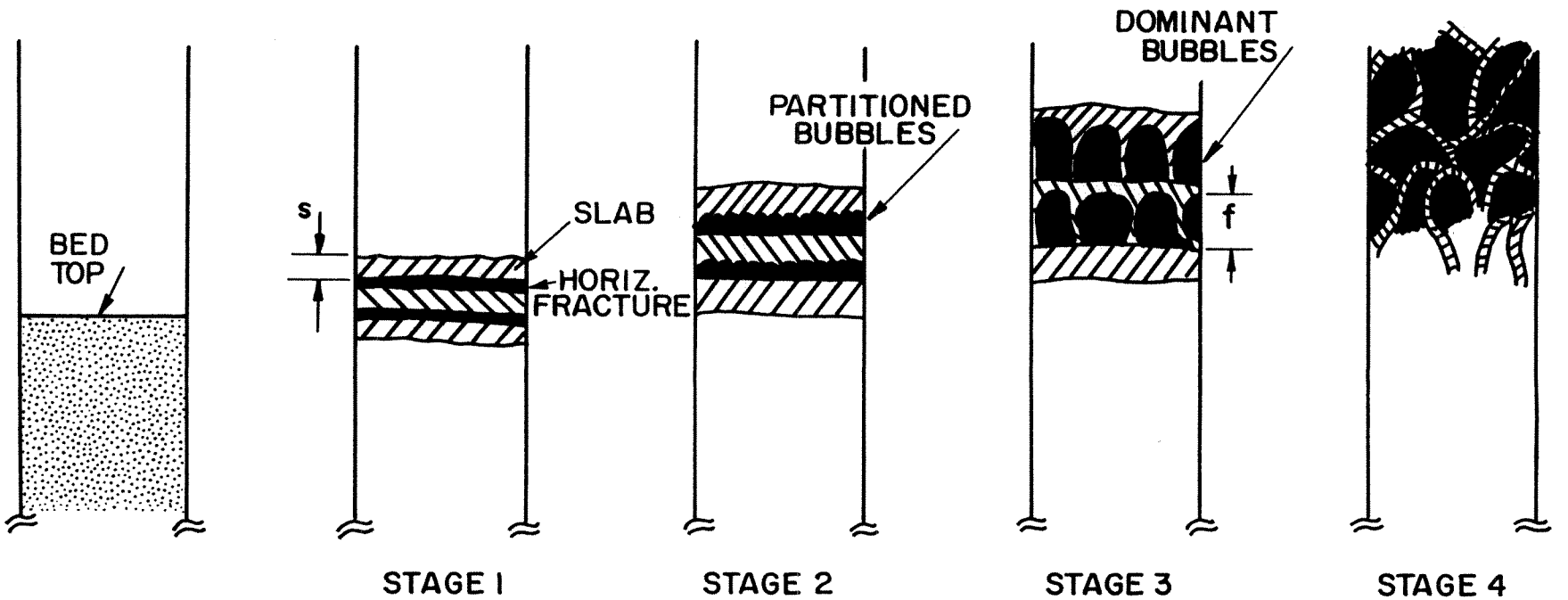

Figure 3.5 Schematic of bed expansion route.

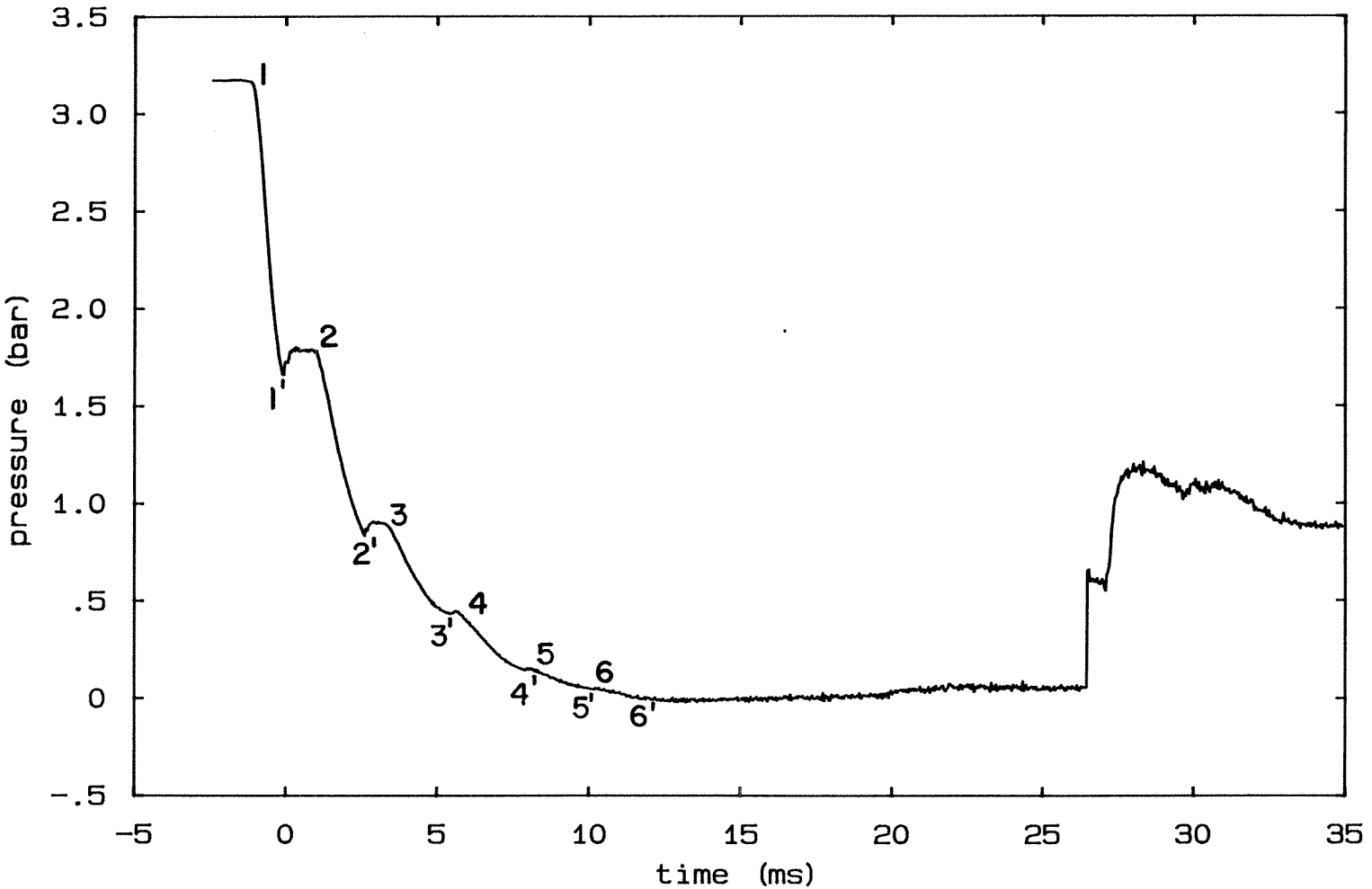

Figure 3.6a Pressure history 38 cm above bed (Run 2): with retaining screen.

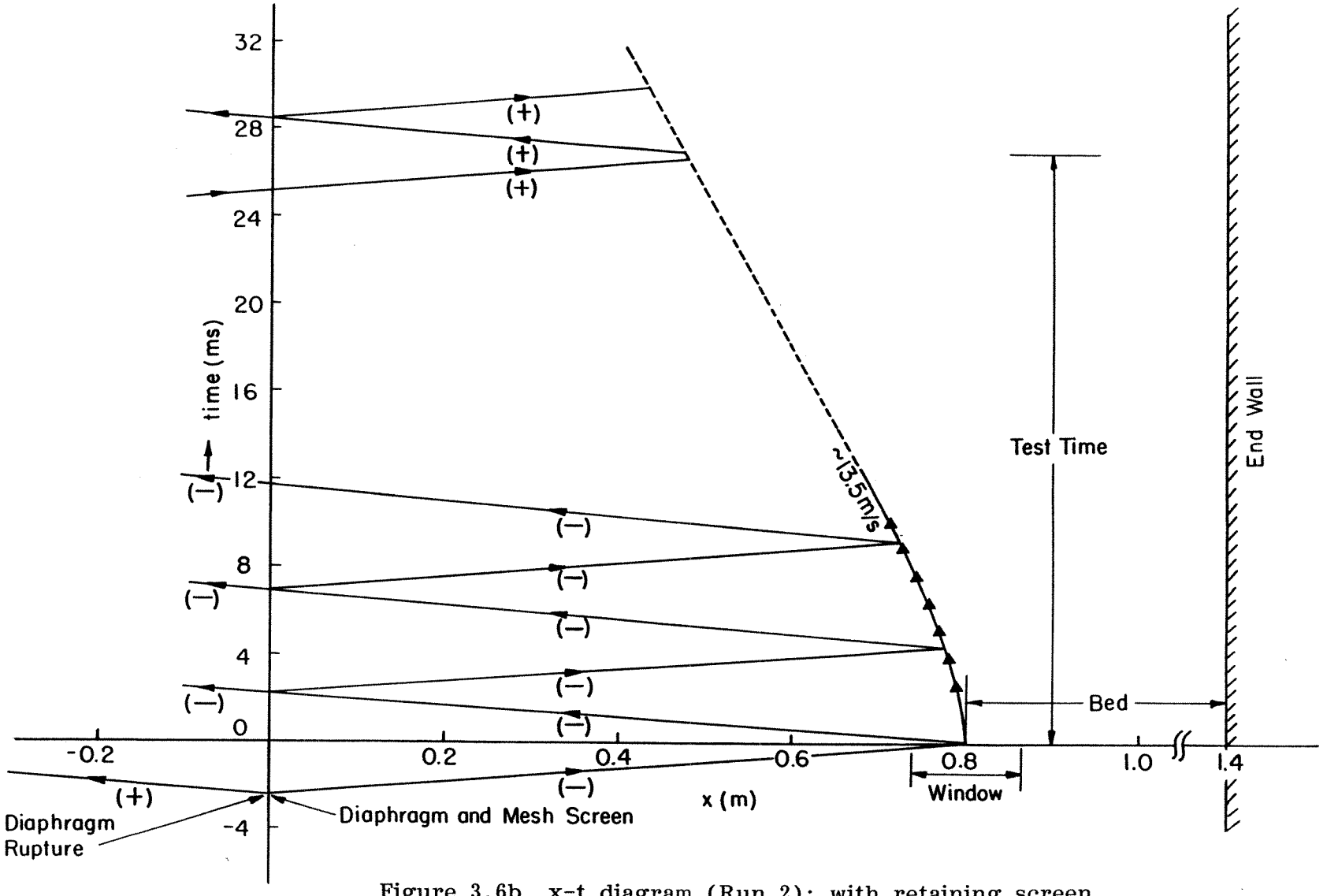

Figure 3.6b x-t diagram (Run 2): with retaining screen.

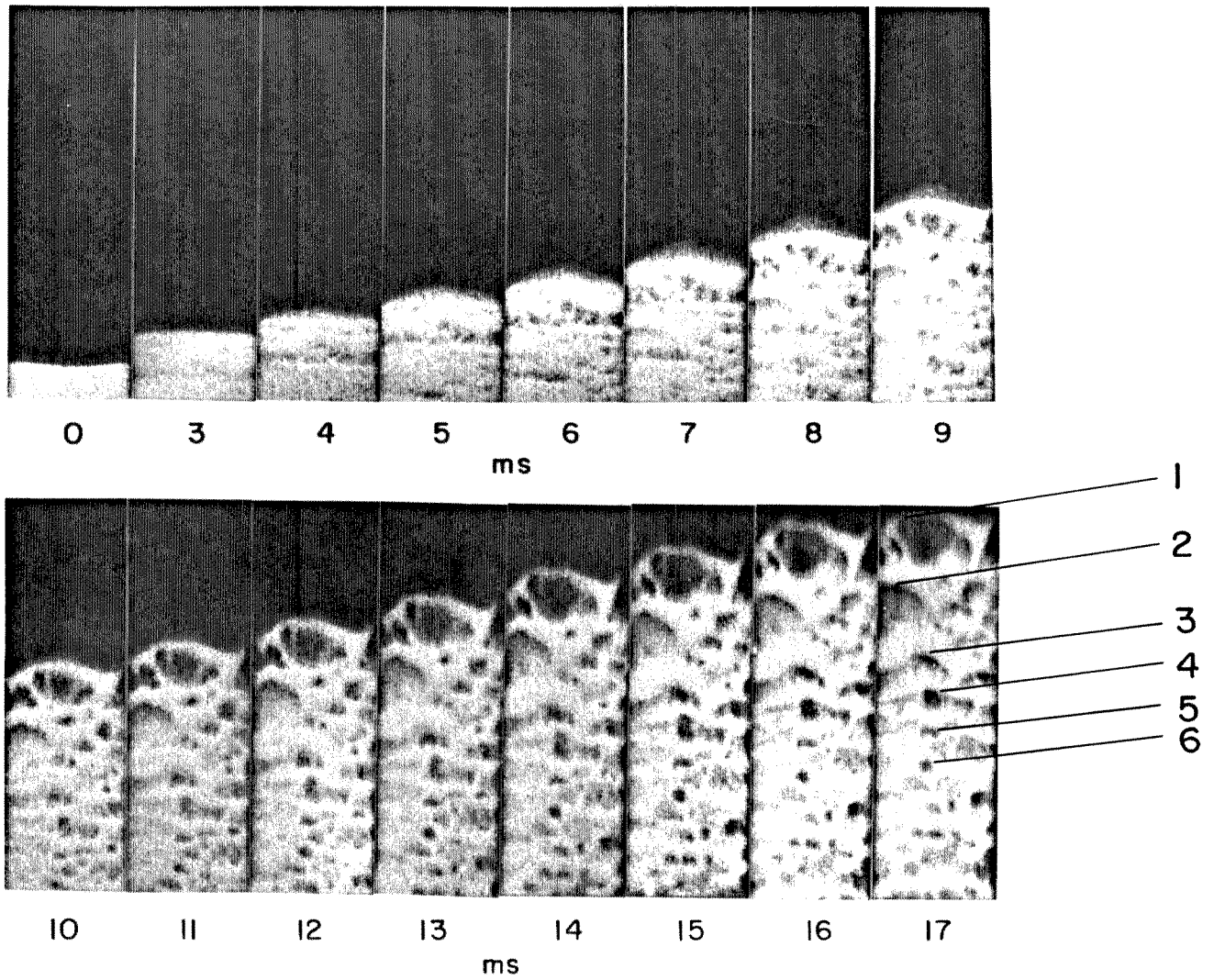

Figure 3.7a Rapid depressurization of a 17 cm bed of 0.25 mm glass beads (Run 3): motion picture sequence.

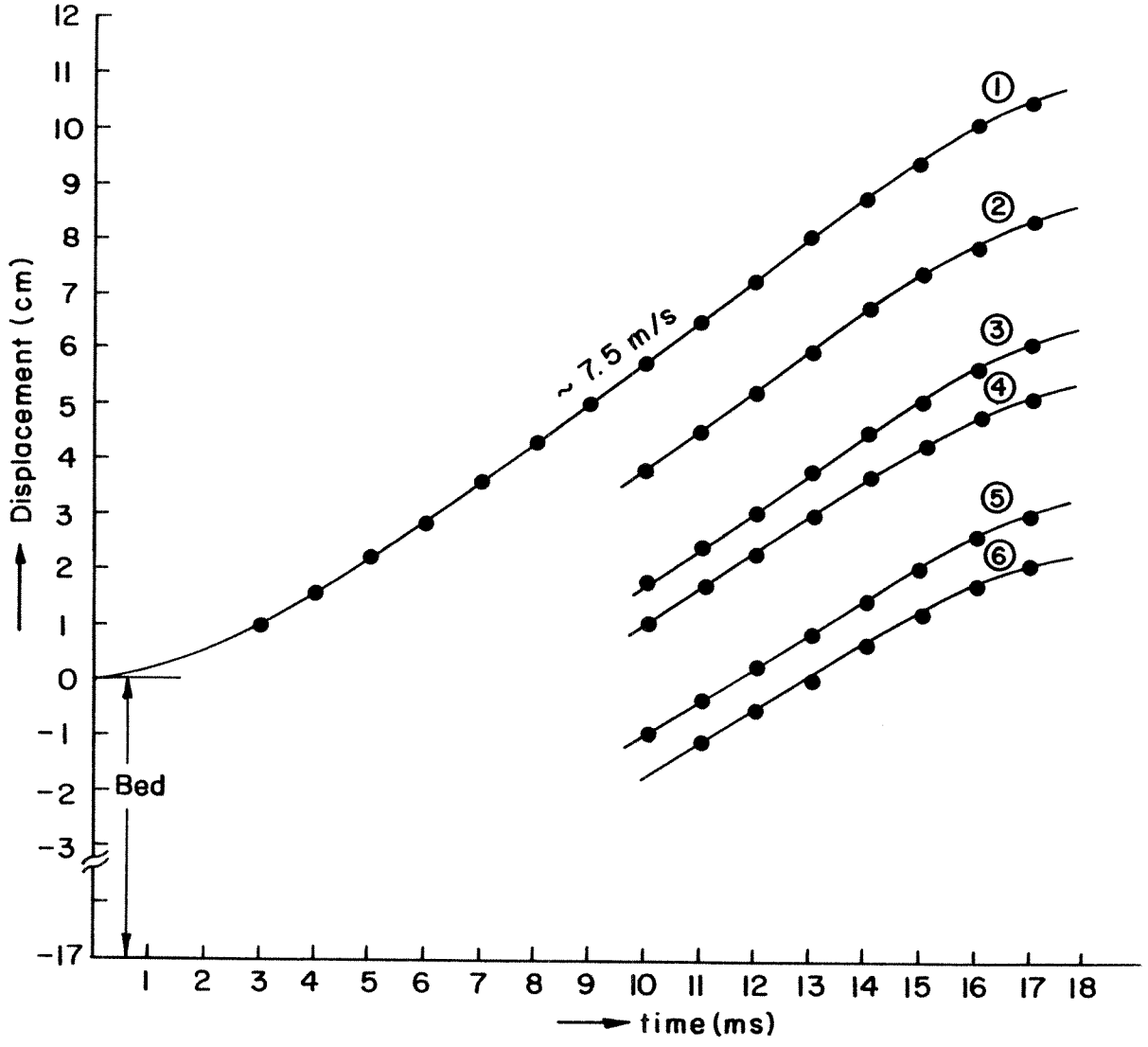

Figure 3.7b x-t diagram (Run 3).

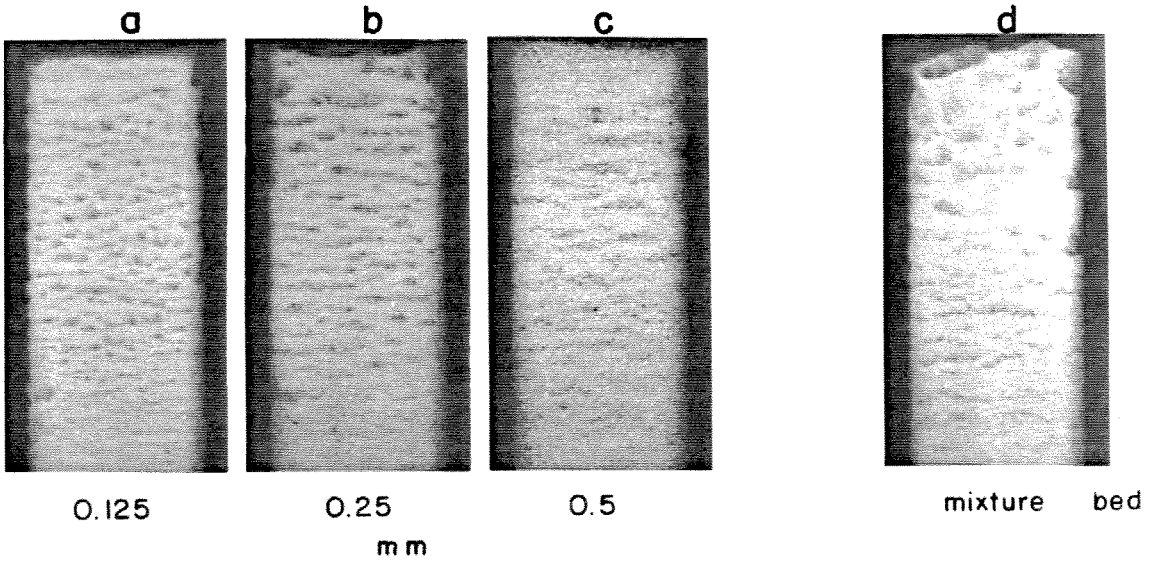

Figure 3.8 Early stages of expansion (6.3 ms).

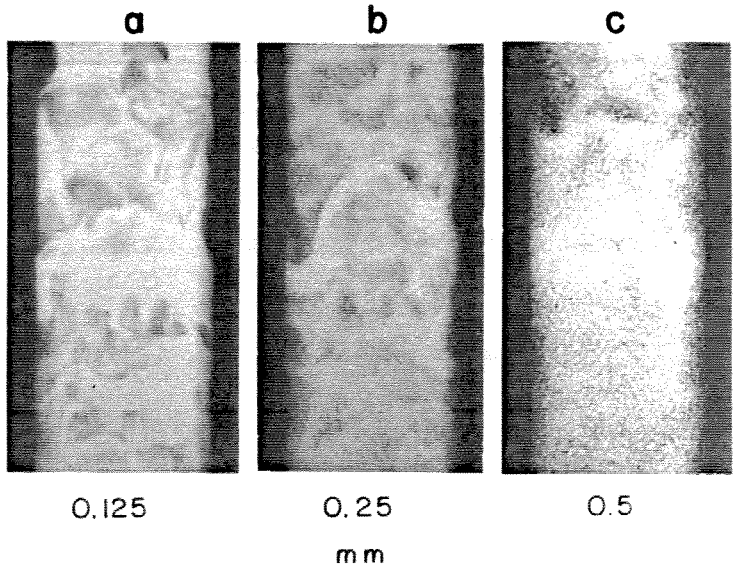

Figure 3.9 Late stages of expansion (20 ms).

Chapter 4

FLUIDIZATION EXPERIMENTS : CONFIGURATION 2

4.1. Introduction.

These experiments were done with short-to-moderate length beds ($0.5 < l_0 / D < 4$) mounted on a mesh screen in the driver section, with a long reservoir of working gas below the bed (Figures 2.3, 2.4). Dusty flow is generated here by the rapid depressurization of the gas within the bed and subsequent fluidization by the gas below the bed. The depressurization process is initiated by the expansion wave that transmits through the bed (§3.2). The transmitted expansion wave reflects from the bed bottom as a compression wave which sets up the driving pressure field across the bed. Consequently, the fluid from below enters and fluidizes the bed.

When driven by gas from below, the entire bed is lofted. The dusty gas flow so generated is rapidly accelerating, dense and nonuniform. It is characterized by the simultaneous presence of dense filamentary structures and dilute dispersions of particles. The flow field is continuously expanding, and in a given experiment, its nonuniform character prevails till high dilutions are reached.

High-speed motion pictures were extensively used to study the flow. Glass beads in sizes from 0.09 to 0.5 mm were used in most of the experiments. Plastic beads, particle mixtures in size and density and ignimbrite volcanic ash were also used.

The experimental results are presented separately as pressure traces and flow visualization, as their information at most times cannot be directly correlated (see §2.3.1). The results presented here highlight the various aspects of the flow. More detailed results from a parameter survey are presented in Chapter 5.

4.2. Results.

4.2.1. *Pressure Traces.* Figure 4.1 is a pressure history recorded at a point 42 cm above the top of a 8.9 cm tall bed of 0.25 mm dia glass beads. The diaphragm burst pressure is 2.1 bar (Run 9). The wave configuration through expansion 4 - 4′ is the same as that in Figure 3.6a. The pressure rise 5 - 5′ is mainly due to i) bed acceleration, and ii) fluid leakage across the bed. The arrival of the bed is signaled by spikes (5′) as particles impact and shear against the transducer. The pressure rise (5′ - 9) as the bed passes represents the driving pressure field across the bed, and the pressure fluctuations (6 - 6′ - 7, 7 - 7′ - 8) are local nonsteady activities in the bed, namely bed expansion through bubble growth; the latter observation is borne out by flow visualization (§4.2.2).

Figure 4.2 shows some salient features of the dense dusty flow field. These are photographic prints of selected frames drawn from high-speed motion pictures of the flow generated with a 7.6 cm deep bed of 0.18 mm glass beads at 2.0 bar diaphragm burst pressure. Figure 4.2a shows an expanded and elongated bubble (Run 10a). Bubble walls are continuously stretched by the through flow, resulting in a dusty flow with dense filamentary structures, as in Figure 4.2b (Run 10b).

Figure 4.3 is a pressure survey made at four locations, referenced to the initial location of the bed top, in a shorter bed (5.1 cm) of the 0.25 mm dia glass beads lofted 7.8 cm from below the window center. The diaphragm burst pressure is 1.9 bar (Run 11). The various stages of bed expansion are well represented here. The incident expansion fan strength is 1.4. The depressurization above the bed is complete by 8 ms. The driving pressure field across the bed is initially set up by the expansion wave transmitting through the bed and reflecting as a compression wave from the bed bottom. The fluid entering from below fluidizes the bed. The bed expansion proceeds upwards along expanding and elongating bubbles (see §4.2.2). The growing bubble passing by the transducer (trace B) is characterized by i) a spiky pressure rise (1 - 2) and ii) by a slow expansion (2 - 3) as the bubble

grows and expands while still traversing the transducer. As the bed expands, the through flow continuously increases, and at later times, the transducer signal is noisy (trace C) owing to collisions of the particles against the sensitive surface of the transducer. The pressure drop below the bed (trace D) is caused by a simple expansion wave, and this pressure drop can be used to compute the instantaneous fluid velocity and density below the bed. This information, along with a knowledge of particle speeds, can be used (see appendix C) to estimate the instantaneous slip Reynolds numbers of the particles (see §5.2.1.4). In this experiment, the test is terminated by the arrival of the reflected shock wave from the top end of the facility (4, 5, 6).

4.2.2. *Bubble Growth and Bed Expansion.* Figure 4.4a is a pressure history monitored by the window transducer, T_w, and Figure 4.4b is a corresponding sequence of flow features taken simultaneously with a high-speed motion picture, for the dusty flow generated with a 5.7 cm tall bed of 0.18 mm dia glass beads initially loaded 16 cm below the window center. The diaphragm burst pressure is 2.0 bar (Run 12). The flow arrives at the center of the window about 14 ms after the initiation of the experiment.

Figure 4.4b shows the mechanism of bed fluidization and subsequent expansion in the upper regions of the bed. The bed expansion occurs along nonuniformities initially formed during the rapid depressurization process. As the latter grow into bubbles, the through flow increases, and the bed continues to expand. Subsequently, the bubble walls will be stretched resulting in a flow with dense filamentary structures.

The pressure history (figure 4.4a) shows how pressure within the bubble A behaves as it passes along the wall. It is characterized by: i) a spiky pressure rise (2, 3) and ii) a slow pressure drop (4, 5, 6) as the bubble expands and elongates while still traversing the transducer. Afterward, the pressure continues to drop (7,

8) due to continuous depressurization along the wall resulting from the burst of the bubble at the top (6).

4.2.3. *x-t Diagram and Intensity Measurement.* Figure 4.5 is an $x-t$ diagram for the 7.6 cm deep bed of 0.18 mm dia glass beads starting 42.5 cm from below the center of the viewing window. The diaphragm burst pressure is 2 bar (Run 13). The $x-t$ diagram has been constructed from transducer records and motion picture information. The bed expansion data have been listed in Table 4.1. The diagram shows the leading edges of the incident expansion fan, its reflection from the top of the bed and the re-reflection from the mesh screen. The depressurization above the bed is complete in 9 ms. The test is terminated by the arrival of the reflected expansion fan from the bottom end of the facility. The bed continuously accelerates and expands during the test time (~44 ms). The bed top reaches speeds of 46 m/s in 25 ms, representing an average acceleration of 185 g. Starting at 24 ms, the dusty flow coming by the window has expanded to about 10 times the original bed height.

Figure 4.6a is a photodiode trace generated by projecting frame-by- frame, a 8000 fps high-contrast motion picture of the dusty flow of Run 11, on to a photodiode (see appendix B). The photodiode trace represents a measure of the intensity of the back scattered light recorded on the motion picture and gives a general idea of the flow field density distribution and level of expansion. The multipeak intensity distribution of Figure 4.6a is typical of highly expanded beds. Figure 4.6b shows the features of the flow field at selected times as the flow traverses the viewing window (here the frames correspond to the numbers on Figure 4.6a). It is clear that flow field is dense and nonuniform, with filamentary structures (3, 7, 14) that span the channel. The intensity decrease during frames 4 - 6 is due to the passage of a large void region in front of the viewing window. The later time decrease in intensity (12, 13, 14) is due to arrival of the bottom regions of the flow and consequent termination of the flow.

Table 4.1. Data for $x-t$ Diagram : Figure 4.5

Bed Top		Bed Bottom	
t (ms)	S (cm) *	t (ms)	S (cm) *
9.5	2.5	27.8	10.1
16.3	12.5	33.9	20.1
20.4	22.6	39.3	30.2
21.8	27.7	41.8	35.0
23.0	32.4	44.1	40.1
24.0	36.5		
24.4	38.2		
24.8	40.0		
25.4	42.7		
26.0	45.5		

* S = displacement

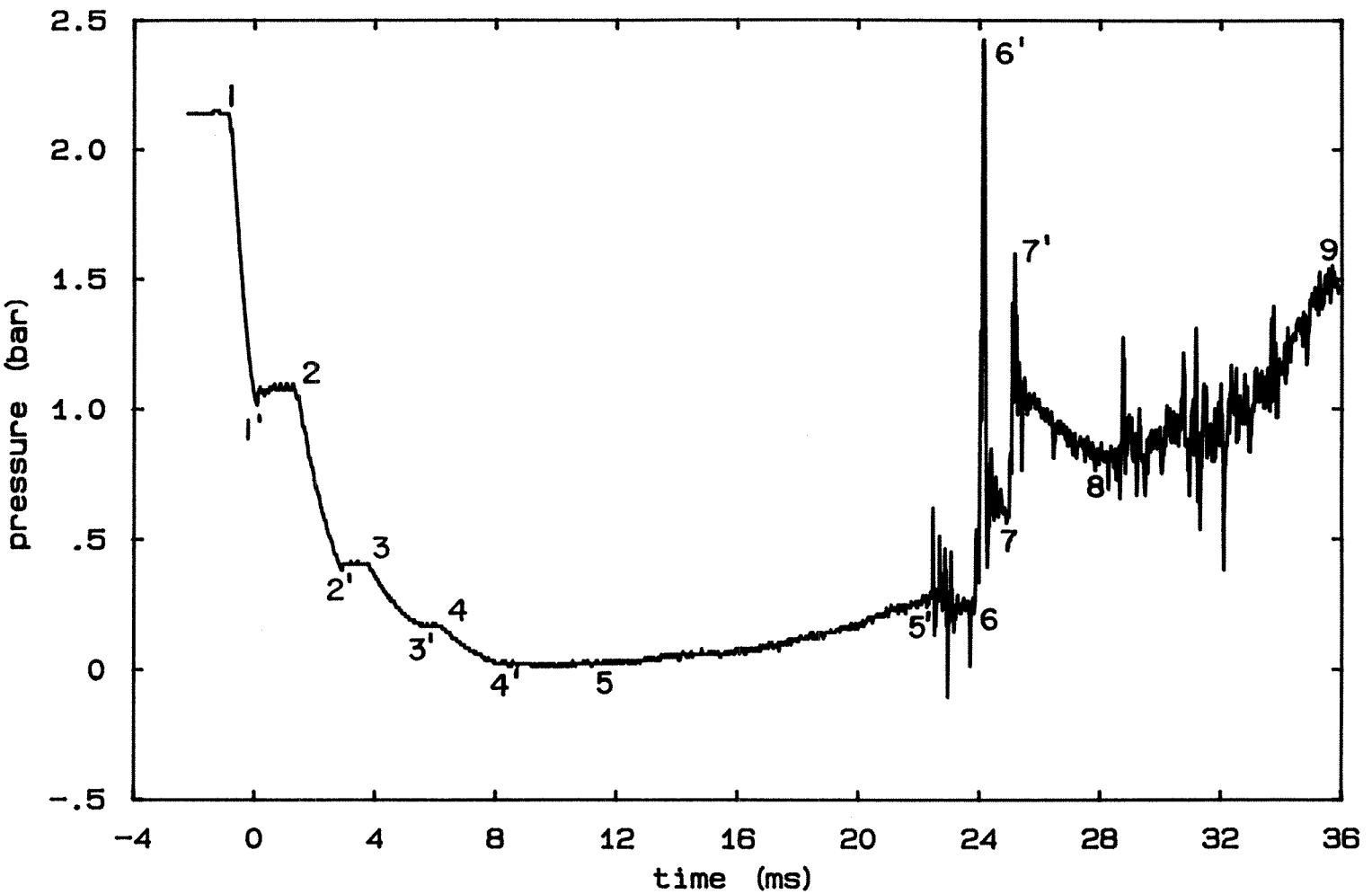

Figure 4.1 Pressure history 42 cm above bed (Run 9).

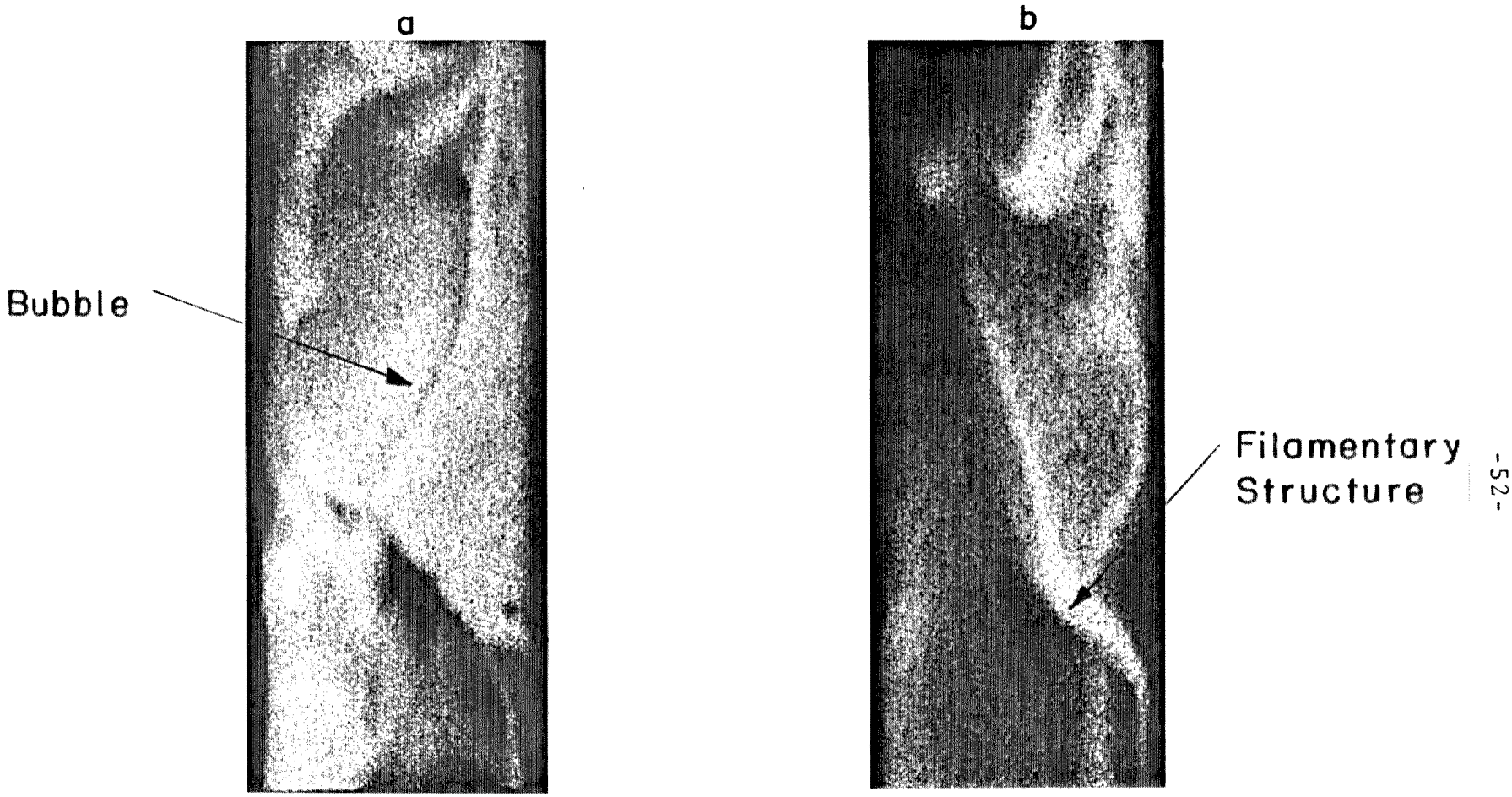

Figure 4.2 Salient features of dense dusty flow

(a) example of expanded and elongated bubble
(b) example of filamentary structure.

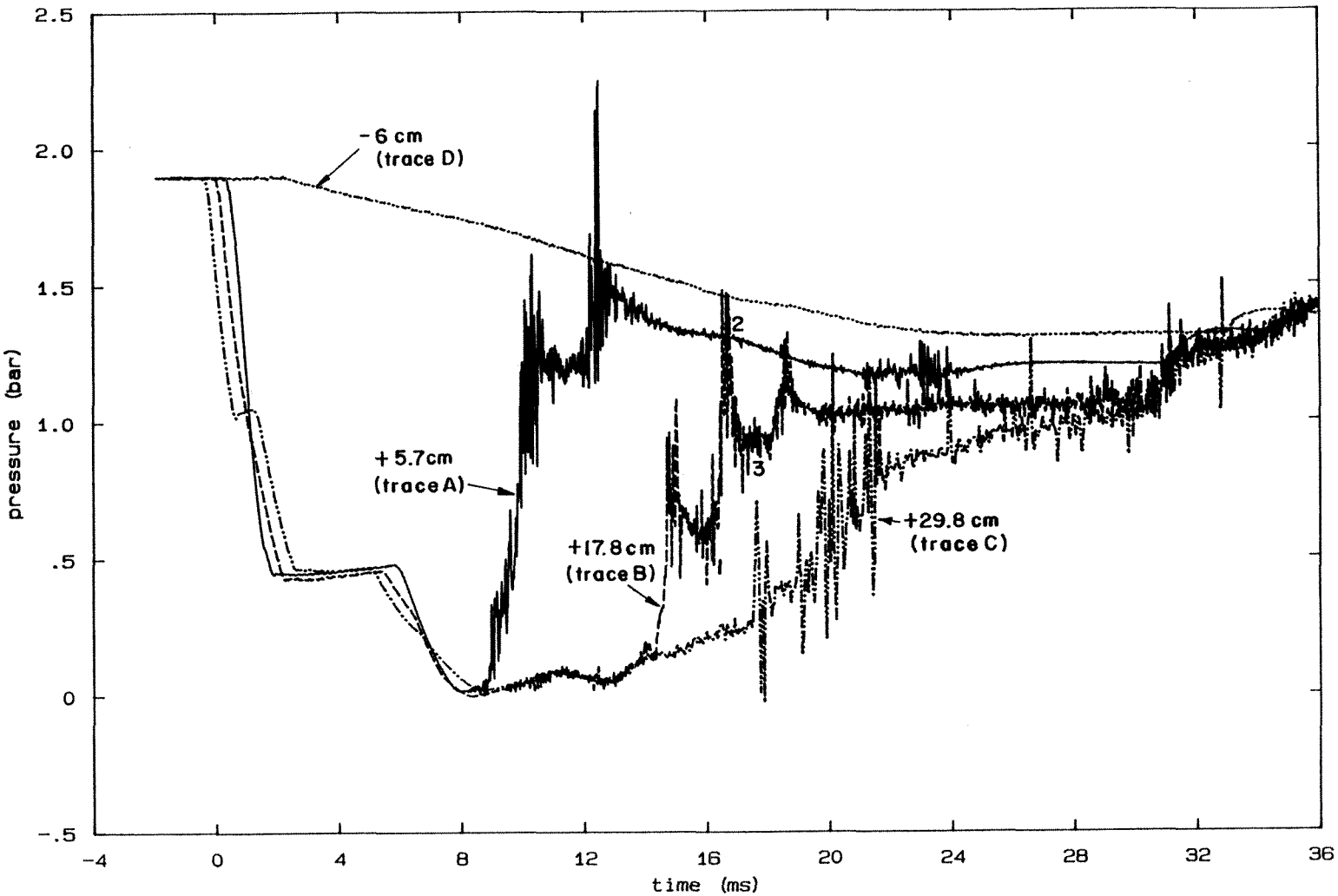

Figure 4.3 Pressure survey at locations referenced to initial location of the top of the bed (Run 11) (Bed 5.1 cm, 0.25 mm glass beads).

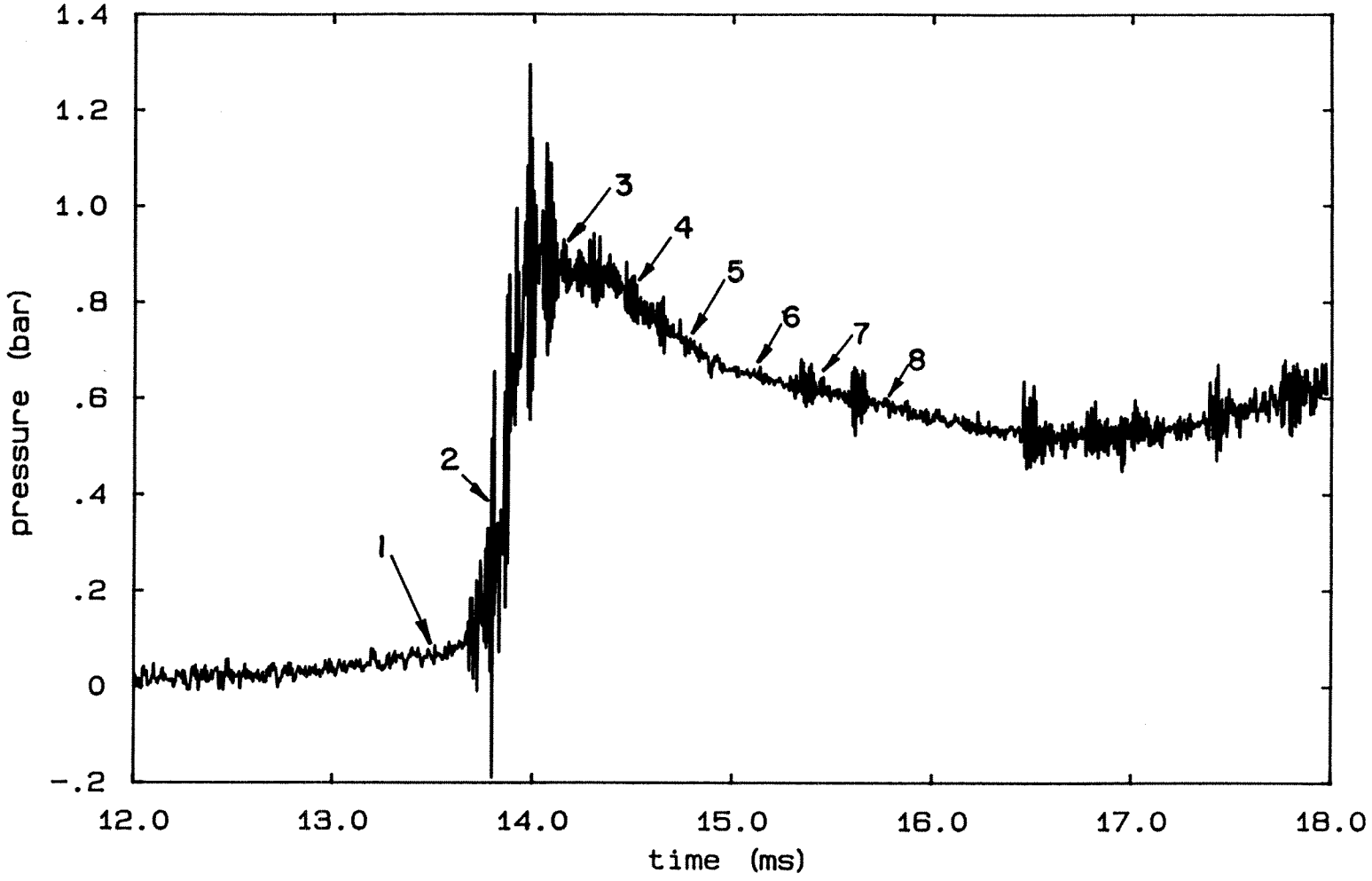

Figure 4.4a Pressure history of a growing and bursting bubble (Run 12).

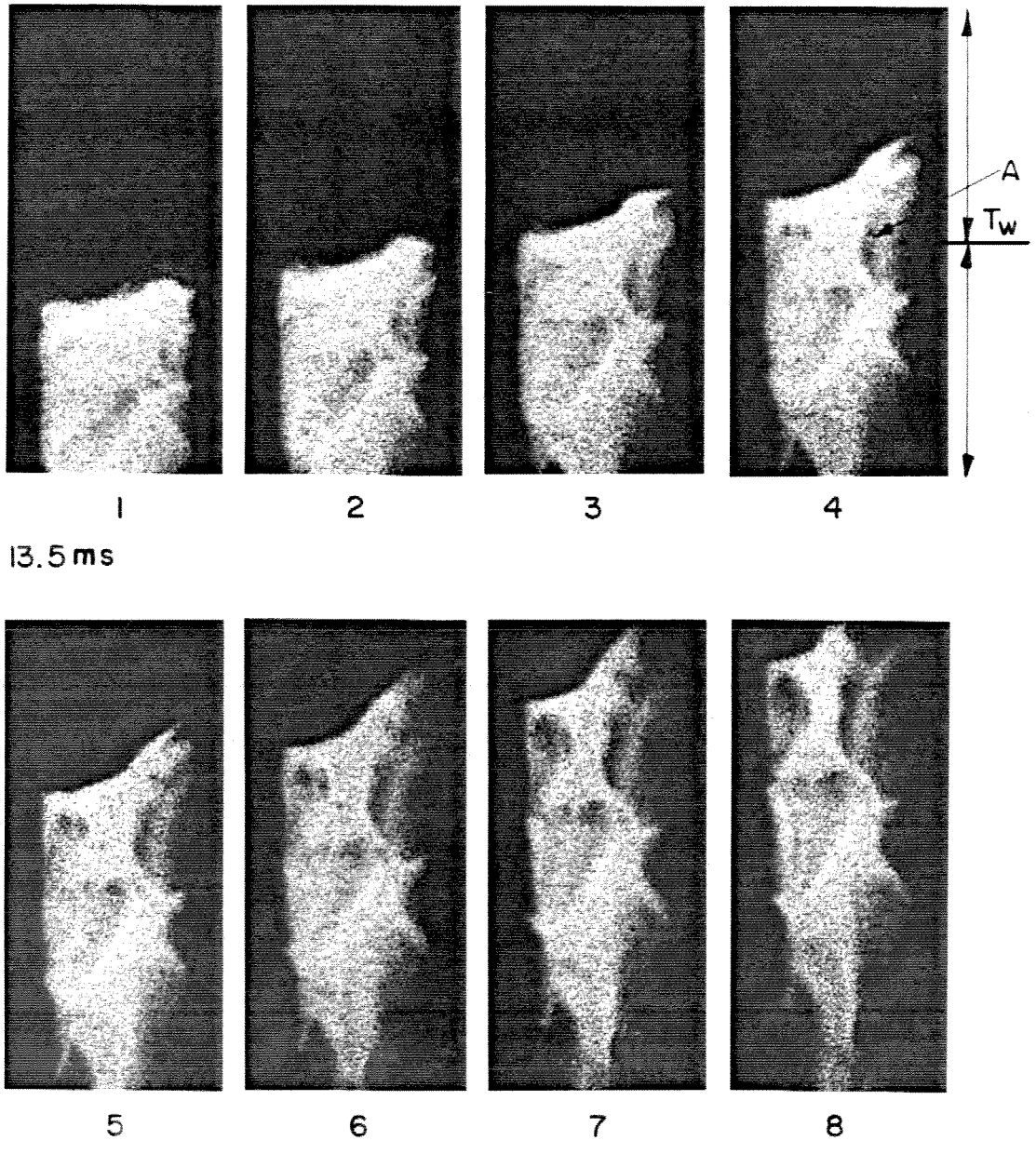

Figure 4.4b Fluidization in the upper regions of the bed (Run 12): motion picture sequence 0.33 ms apart, picture 1 taken 13.5 ms after initiation of the experiment.

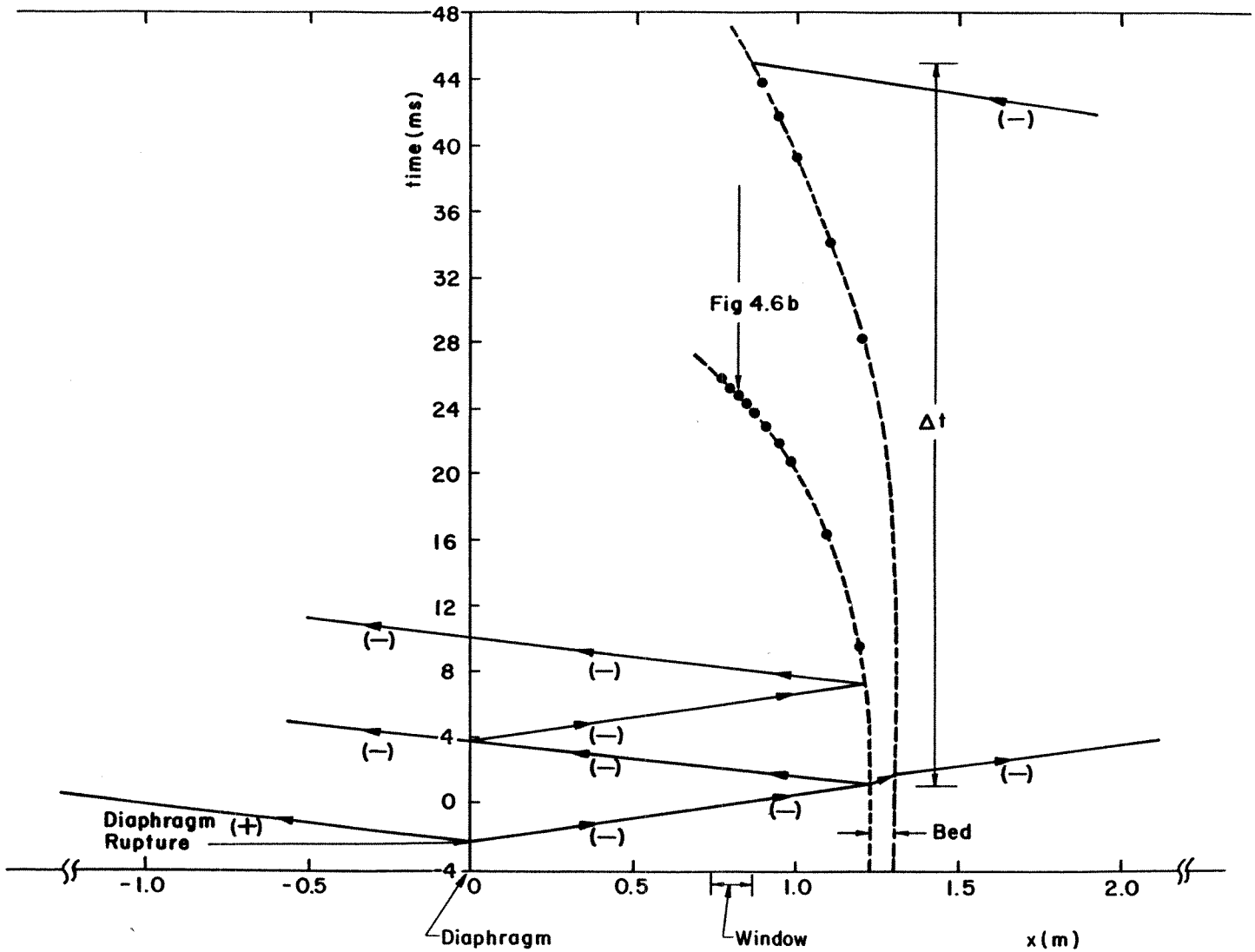

Figure 4.5 x-t diagram (Run 13).

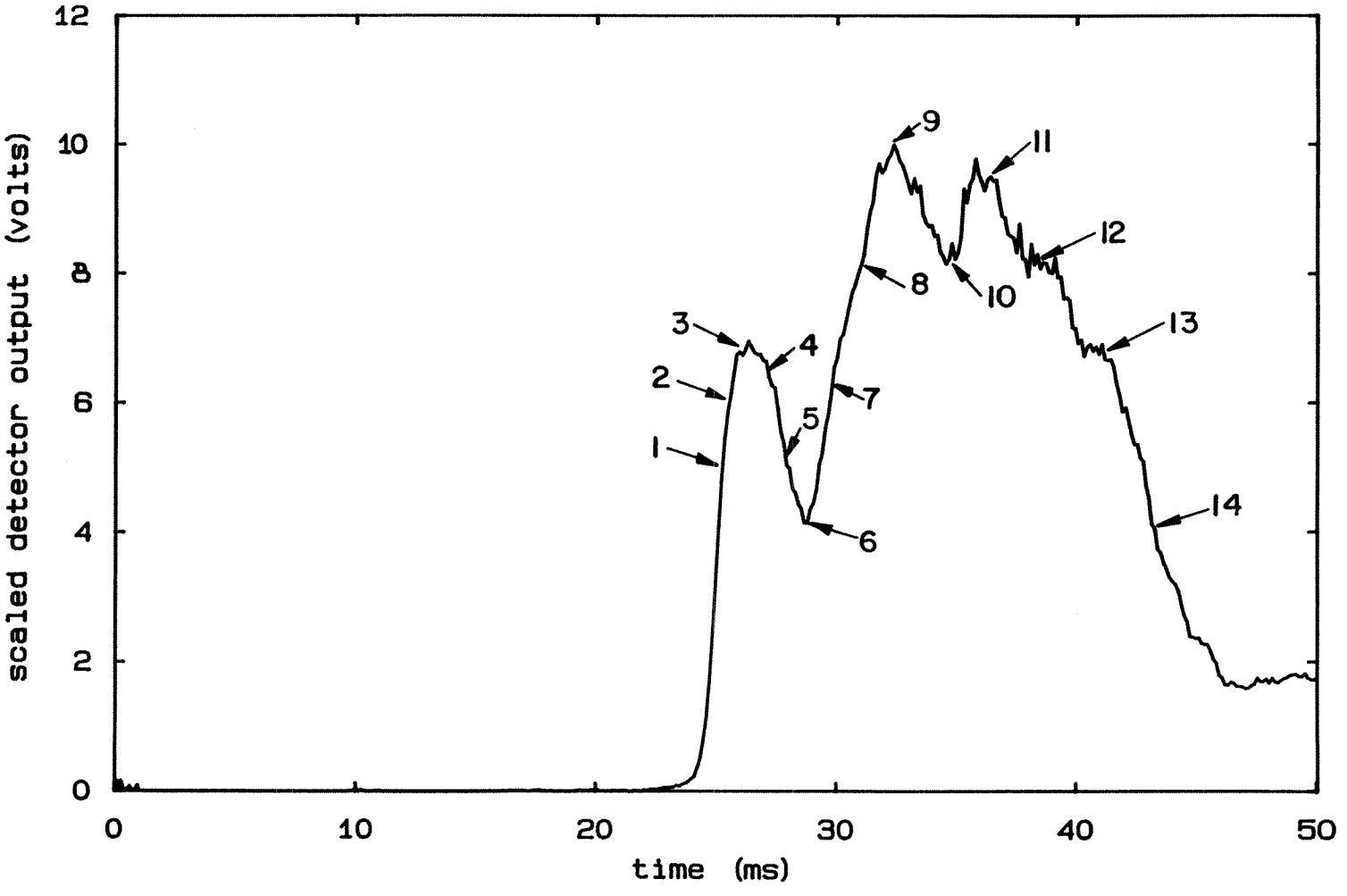

Figure 4.6a Photodiode trace of a high-speed motion picture (Run 13) (numbers correspond to frames in figure 4.6b).

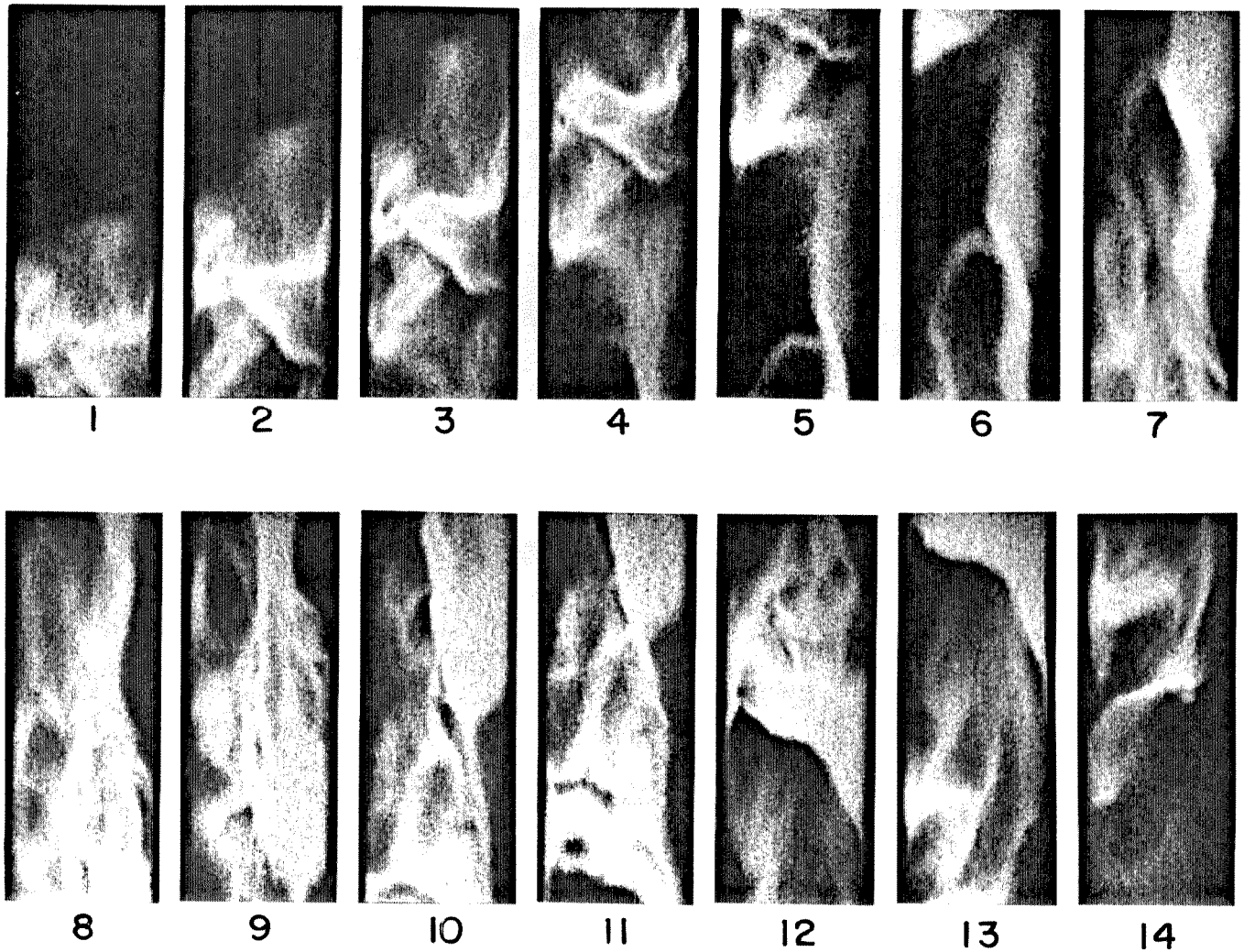

Figure 4.6b Flow sequence from a high-speed motion picture (Run 13) (frames correspond to numbers in figure 4.6a).

Chapter 5

FLUIDIZATION EXPERIMENTS : PARAMETER SURVEY

5.1. Introduction.

The results of the parameter survey of the fluidization experiments (configuration 2) are presented here. The parameters discussed are acceleration gradient, characteristics of the incident expansion fan, bed height, particle size, particle density, and operating pressure. The role of wall effects and electrostatic forces on flow development are also discussed.

The fluidization mechanics is strongly influenced by the presence of a gradient in acceleration, set up by stacking particles of different size or density or both, in the stationary bed prepared for lofting. The acceleration gradient in a stacked bed results from the fact that in a given fluid flow, the smallest and the lightest particles would accelerate the fastest and the largest and the heaviest particles would accelerate the slowest. The acceleration gradient experiments help to advance the understanding of the fluidization phenomenon.

Studies show that all flow fields, except packed plug flows and dilute disperse particle flows, are nonuniform and are characterized by the simultaneous presence of dense filamentary structures and dilute dispersions of particles.

5.2. Role of Acceleration Gradient.

An artificial horizontal discontinuity in acceleration characteristics was set up in a stationary bed, and the expansion of the bed was examined on initiation of lofting. The discontinuity is an interface between stacks with different particle size or density, or both.

Only short bed heights ($l_0 / D \sim 1$) were studied. The diaphragm burst pressure was around 2 bar. All beds were initially loaded on a mesh screen located at the bottom level of the window. The bed lofting was studied with high-speed

motion pictures taken at 6000 fps.

5.2.1. *Results.*

5.2.1.1 Stable Lofting. Figure 5.1 is a sequence of prints, from a motion picture, showing the lofting of a 3.8 cm deep bed, stacked in equal heights with 0.25 mm, 0.5 mm and 0.75 mm dia glass beads (Run 25). The smallest beads, which will accelerate the fastest in a given fluid flow, are at the bottom, and the largest beads are at the top. This stacking arrangement is highly stable. Figure 5.1a shows the stationary bed. On flow initiation (Figure 5.1 b-f) the bed lofts like a plug, and the nonsteady character of bed fluidization and subsequent expansion (§4.2.2) is not observed. The two interfaces between layers of different sized particles do not show any tendency to separate. The only nonuniformity seen is that due to particle shedding from the bed bottom by Rayleigh-Taylor instability.

Figure 5.2 is a motion picture sequence showing the lofting of a taller bed (5 cm) with 0.5 mm and 0.25 mm dia glass beads stacked in the ratio 7:1 by depth and arranged for stable lofting (Run 26). The horizontal fractures, resulting from the rapid depressurization of the gas within the bed (*cf.* §3.2.3), are visible in the upper regions (Figure 5.2b, c). These fractures do not grow in time. Indeed, the bed later repacks (Figure 5.2d) from the bottom to the top to form a plug in the channel. At this stage, the particle shedding at the bed bottom stops (Figure 5.2e) and the bottom becomes flat.

In general, stably stacked beds initially expand nonuniformly due to the expansion of the gas inside them, but will subsequently repack to form a plug in the channel.

5.2.1.2 Unstable Lofting. Figure 5.3 is a motion picture sequence showing the lofting of the three-particle bed of Run 25, now stacked in reverse configuration with the largest beads (0.75 mm) at the bottom and the smallest beads (0.25 mm) at

the top (Run 27). This stacking arrangement is unstable. On flow initiation, the bed quickly expands. In particular, expansion occurs at the interfaces (Figure 5.3b, c), and this arrangement behaves as three different beds. Expansion also occurs along horizontal fractures that are initially formed during the rapid depressurization of the gas within the bed (Figure 5.3d-f); here, the smallest beads partition the fastest (see §3.5).

5.2.1.3 Pressure Traces. Figures 5.4 and 5.5 represent the static pressure histories at a point 1.9 cm above the initial location of the top of the bed for the stable and unstable lofting of the three-particle bed (Run 25, 27). In stable arrangement, the bed has a near linear pressure gradient, while in the unstable arrangement, the bed continuously expands at the interfaces and at other fractures.

Figure 5.6 shows the pressure history below the bed for the stable and unstable lofting of the three-particle bed. The stronger expansion in the unstable setting is due to the greater through flow past the more expanded bed.

5.2.1.4 Fluid and Particle Velocities, Slip Reynolds Number. Figure 5.7a is a time plot of the fluid velocity (u_g) and particle velocity (u_p) for the stable lofting of the three-particle bed (Run 25), and Figure 5.7b is the corresponding plot for the unstable lofting of the three-particle bed (Run 27). The particle velocity for both cases is the average velocity of the largest particles (0.75 mm) and has been estimated from high-speed motion pictures of the flow. The gas velocity (u_g) and also its density (ρ_g) have been estimated (see appendix C) from the information provided by the measured pressure below the bed (fig. 5.6). The data and the slip Reynolds number estimates for both stable and unstable lofting have been tabulated in tables 5.1 and 5.2 respectively.

In stable lofting (Figure 5.7a), despite the large initial differences in fluid and particle velocities, the slip velocity, U ($U = u_g - u_p$), quickly approaches constant (quasi-steady) conditions. In unstable lofting (Figure 5.7b), on the other hand, the

slip velocity continuously increases. Figure 5.7c is a time plot of the slip Reynolds number, based on the largest particle diameter (0.75 mm), for the stable and unstable lofting of the three-particle bed.

The qualitative information available from the Reynolds number plot (Figure 5.7c) is essentially the same as that available through flow visualization. Initially, the two bed configurations, stable and unstable, are indistinguishable. In the stable arrangement, the slip velocity reaches a maximum and quickly approaches constant conditions with the slip Reynolds number asymptoting to around 900. In unstable arrangement, the slip Reynolds number continuously increases as the bed expands; here, eventually the Reynolds number will slowly decrease to an asymptotic value as the flow attains equilibrium.

The measured asymptotic value of the Reynolds number of 900 past the three-particle plug corresponds to that estimated, using the Ergun equation (D3), past a similar plug fully packed with only the largest beads (0.75 mm dia) and driven by the same pressure difference across it. Effectively, the three-particle plug behaves as a plug of the largest particles; the stack of smallest beads (0.25 mm dia) apparently expands by about 20% in volume to establish the same through flux ($\rho_g U$) as that past the largest (0.75 mm dia) beads at the top. This expansion is too small to be noticable.

5.2.1.5 Density Gradient. Similar stability observations were made when a bed was initially stacked with beads of one size but of different particle density (ρ_p) and lofted. Figure 5.8 is a motion picture sequence showing the lofting of a 3.8 cm deep bed stacked in layers of equal height with 1 mm dia beads of steel, glass and plastic with steel (slowest acceleration) at the top and plastic at the bottom (Run 28). This set up is highly stable and lofts as a plug (Figure 5.8b - d). The reverse stacking of this combination (Run 29)is highly unstable (Fig 5.9). On flow initiation, the bed quickly expands at the interfaces and along horizontal fractures

(Figure 5.9b, c). Also, since the beads are all of the same size, the fractures partition at about the same time. Figure 5.9 was reproduced from an original color motion picture frame, so the quality is not good.

In the stable arrangement, the interface cannot separate because the bottom accelerates faster than the top, and the bed packs up and moves just as a plug of the heaviest (steel) particles. The unstable arrangement, however, behaves as three different beds.

5.3. Effect of Bed Height.

Increasing the bed height, keeping particle size the same, results in an increase in bed drag, and, for the same driving pressure difference, the through flow is lower.

Figure 5.10 shows a photodiode trace along with the flow features for a much taller bed (9.5 cm; l_0/d_p = 528) of 0.18 mm glass beads (Run 15) as compared with Figure 4.4b (Run 12, l_0/d_p = 317). Clearly, the upper regions of the bed are not completely fluidized as compared with Figure 4.4b. The nonuniformities at the top levels of the bed, formed during rapid depressurization, do not grow and instead the material at the bed top consolidates (1, 2, 3) into a flow head (4, 5). The head formation is preceded by rapid upward buoyant motion of nongrowing bubbles as is evidenced by the splashing of particles at the bed top (1, 2). These bubbles start from intermediate levels of the bed. When the flow head is formed, most of the drag is across it and the through flux past it is quasi-steady. The magnitude of the through flux can be estimated using the Ergun equation (D3). The average through flow velocity is about 3 m/s and the through flux Reynolds number is about 60. The head acceleration is around 200 g.

The bottom of the bed is characterized by the presence of a flow *tail* (6) that terminates in a bulbous and streamlined bottom (7) from which material is slowly eroded by the coflowing fluid. The tail structure is more clear while working with

larger size particles, as is evident from picture 8 for 0.5 mm glass beads. The *tail* is formed by the accumulation of the particles originally shed at the bed bottom.

Figure 5.11 is a motion picture sequence showing the motion of a buoyant bubble and its emergence from the free surface in the upper regions of a bed accelerating at 150 g (Run 14). It resembles a spherical cap bubble seen in conventional fluidized beds (Rowe, 1971). The bubble here accelerates on approaching the top of the bed. The average speed of this bubble relative to the bed is about 5 m/s. An isolated buoyant bubble in an accelerating fluidized bed presumably travels much the same way, in the main body of the flow, as in conventional gas fluidized beds where the motion is governed by the following equation (Davidson & Harrison, 1977):

$$u_b = 0.83\ (gh)^{1/2}; \quad u_b: \text{bubble velocity}, \quad h: \text{bubble height}$$

in the present context $g \equiv 150 \times$ acceleration of gravity and $h \simeq 10$ mm

$$\rightarrow u_b = 3.2\ m/s \quad \text{(in the main body of the flow)} \quad .$$

5.4. Effect of Particle Size.

Reducing the particle size has the same effect as increasing bed height, both effectively increasing the particle population and thereby the drag interaction with the through flow.

Figure 5.12 is a motion picture sequence showing the lofting of a 6.3 cm bed of 0.09 mm glass beads ($l_0/d_p = 700$) lofted from the window bottom level. The diaphragm burst pressure is 2.0 bar (Run 19). The growth of the nonuniformities (b, c) formed during the depressurization process is not sustained in the long run and the bed reconsolidates (d, e) bottom up to form a plug in the channel. The Rayleigh-Taylor instability of the bed bottom is clear (d). The through flux quickly reaches quasi-steady conditions, and the shedding of the bottom stops as is

evidenced by the flattening of the bottom bubble roofs (e). The Reynolds number of through flux on reaching quasi-steady conditions is low and about 12. After forming, the plug accelerates at 160 g. The driving pressure field across the unexpanded plug resembles that in Figure 5.4.

5.5. Effect Of Particle Density.

Operating with lighter particles has the same effect as operating with smaller particles; both of these types of particles are dragged faster in a given through flow. For a given particle size, beds with lighter particles are less completely fluidized than beds with heavier particles.

5.6. Effect Of Particle Composition.

Operating with particle mixtures of mixed size and density and ignimbrite volcanic ash did not show any difference in the morphology of the flow field which was essentially composed of filamentary structures and a dispersion of colliding particles. Sorting, resulting from different magnitude drag forces operating on the various particles, was not observed in these early stages of bed acceleration and expansion as monitored in this facility.

5.7. Effect Of Operating Pressure.

Facility design and performance provided limited flexibility in changing operating pressure. Operating at higher pressure did not fundamentally influence the nature of the flow field. Here the through flow is higher, but also the particles are accelerated more rapidly by the denser fluid. The resulting flow morphology turns out to be not much different than at lower pressures. However, higher bed speeds are achieved, and the flow develops further.

5.8. Wall Effects.

The late stages of flow development are influenced by wall effects. The formation of the concentric column of particulates, namely the *tail* at the bed bottom signals the beginning of the observation of wall effects. The wall effects

manifest as faster moving fluid along the walls and denser accumulation of flow structures towards the center of the channel. The distorted fluid velocity profile with higher fluid velocities closer to the walls results in erosion of the nearby flow structures and consequent peeling off of the particles. Thereby, the dusty flow goes through a continuous dilution process.

5.8.1. *Late Stages of Bed Expansion.* Operating with extremely short beds ($l_0 / D \sim 0.5$) gave an opportunity to study the late stages of flow field development. Figure 5.13 shows the flow field of a 1.25 cm bed of 0.5 mm glass beads ($l_0/d_p = 25$) lofted from 75 cm below the window center (Run 20). These are single-flash polaroid pictures taken with backlighting and using darkened beads (*cf.* §2.3.2).

At early times of arrival (a, b), the flow speed is about 60 m/s, and also the flow field is uniform; though nonuniformities on the scale of 2 - 3 particles may prevail. More importantly, the flow is dilute, and the loading is progressively higher as the flow comes by. The interesting aspect here is the arrival of dense globular masses at later times (c, c′). High-speed motion picture (d) revealed that these are fragments formed when the tail breaks down during erosion, after sustaining its integrity over considerable length of travel. The fragments are again slowly diluted and dispersed by erosion.

Chapter 6 outlines some preliminary mass loading measurements using a special probe. The measured mass loading in dilute flows, like the ones arriving at early times (a, b), is quite low, and the corresponding volume fraction is around 0.9% (see §6.3).

5.9. The Role of Electrostatic Forces.

Particles rubbing against each other and against walls of the channel tend to accumulate electrostatic charges and the question arises as to whether the observed flow features are influenced by mutual electrostatic forces of attraction and

repulsion between particles.

The dense dusty flow generated in this facility is continuously accelerating throughout the useful test-period and the accelerations are many times that of gravity. In runs with 0.06 mm glass beads, it was observed that the beads had a tendency to stay on the channel walls at the end of the run. An estimate shows that such beads should individually carry about 100,000 basic charges to overcome the pull of gravity. Since all beads used in the experiments are larger than 0.06 mm, the accelerations due to electrostatic forces should be significantly less than 1 g and hence should not influence the flow development in a highly accelerating flow field such as the current one.

Table 5.1. Slip Reynolds Number: Stable Lofting

$P_0 = 2.07$ bar, $l_0 = 3.8$ cm

$d_p = 0.75$ mm, $\mu = 1.8 \times 10^{-5} \frac{\text{Kg}}{\text{m s}}$, $\text{Re} = \frac{\rho_g U d_p}{\mu}$

time ms	ΔP^* bar	$\Delta P/P_0$	$\Delta l^\dagger$ cm	$\Delta l/l_0$	ρ_g kg/m^3	u_g m/s	u_p m/s	$a_p = du_p/dt$ m/s^2	a_p/g	$U = u_g - u_p$ m/s	Re
0.0	0.07	0.034	0.00	0.000	3.55	0.00	0.0	0	0.0	0.00	0
0.5	1.17	0.565	0.01	0.002	3.52	3.70	0.0	0	0.0	3.70	543
1.0	1.73	0.835	0.02	0.005	3.49	5.45	0.0	400	40.8	5.45	793
2.0	2.01	0.971	0.05	0.013	3.45	9.94	1.7	2100	214.3	8.24	1185
3.0	1.95	0.942	0.10	0.026	3.43	12.48	4.6	2360	240.8	7.88	1126
4.0	1.92	0.927	0.15	0.039	3.41	13.92	6.6	2500	255.1	7.32	1040
5.0	1.89	0.913	0.20	0.052	3.38	16.40	9.2	2750	280.6	7.20	1014
6.0	1.86	0.898	0.24	0.063	3.36	18.75	12.0	2850	290.8	6.75	945
7.0	1.82	0.879	0.26	0.068	3.33	21.64	15.0	2900	295.9	6.64	921
8.0	1.80	0.869	0.26	0.068	3.31	24.44	17.9	2950	301.0	6.54	901

Table 5.2. Slip Reynolds Number: Unstable Lofting

$P_0 = 2.07$ bar, $l_0 = 3.8$ cm

$d_p = 0.75$ mm, $\mu = 1.8 \times 10^{-5} \frac{\text{Kg}}{\text{m s}}$, $\text{Re} = \frac{\rho_g U d_p}{\mu}$

time ms	ΔP^* bar	$\Delta P/P_0$	$\Delta l^\dagger$ cm	$\Delta l/l_0$	ρ_g kg/m^3	u_g m/s	u_p m/s	$a_p = du_p/dt$ m/s^2	a_p/g	$U = u_g - u_p$ m/s	Re
0.0	0.12	0.058	0.00	0.000	3.55	0.00	0.0	0	0.0	0.00	0
0.6	1.30	0.628	0.06	0.016	3.51	4.05	0.0	0	0.0	4.05	592
1.0	1.65	0.797	0.17	0.045	3.49	5.45	0.0	400	40.8	5.45	793
2.0	1.96	0.947	0.67	0.176	3.45	9.44	1.0	1300	132.7	8.44	1213
3.0	1.91	0.923	1.29	0.339	3.42	13.03	2.7	2100	214.3	10.33	1472
4.0	1.87	0.903	2.05	0.539	3.38	16.55	5.5	2400	244.9	11.05	1556
5.0	1.83	0.884	2.99	0.787	3.34	20.77	7.8	2530	258.2	12.97	1805
6.0	1.78	0.860	4.16	1.095	3.30	25.26	10.5	2750	280.6	14.76	2029
7.0	1.72	0.831	NA	-	3.25	29.84	13.4	2900	295.9	16.44	2226
8.0	1.67	0.807	NA	-	3.21	34.26	16.4	3090	315.3	17.86	2389

* ΔP = pressure difference across the bed

† Δl = bed expansion

ρ, U, d_p, μ: values used in the estimation of Re

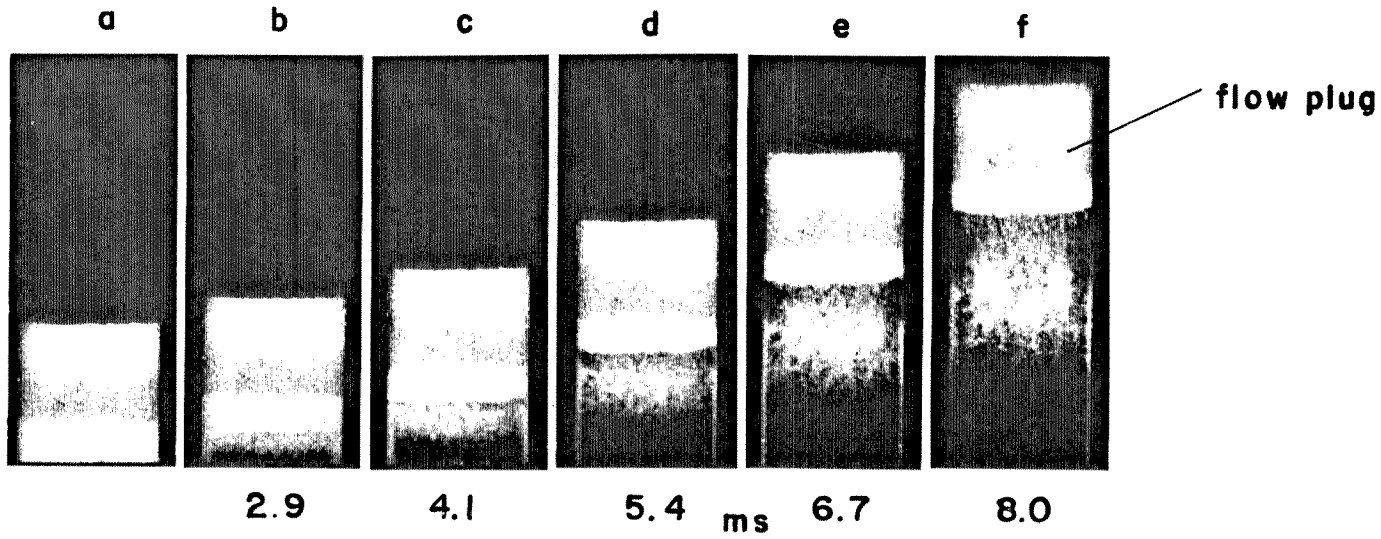

Figure 5.1 Stable lofting of a three-particle bed (Run 25).

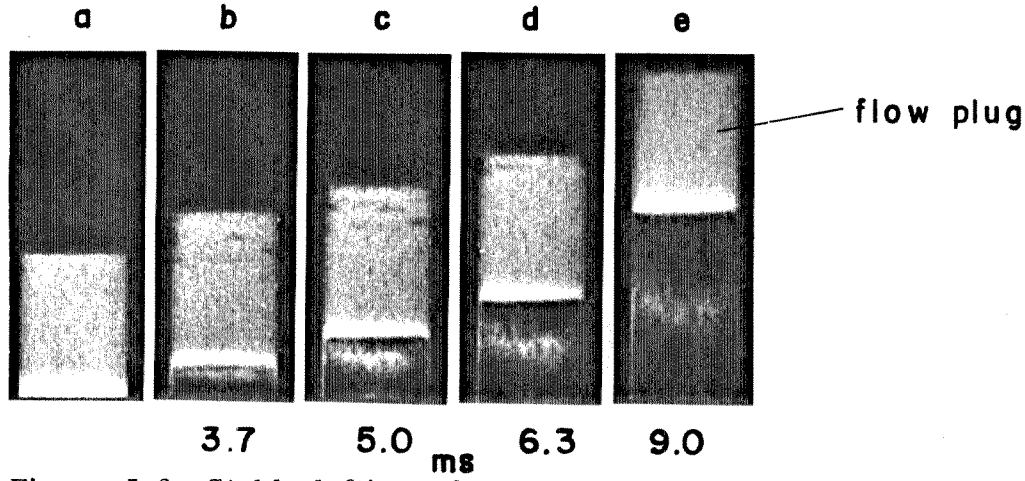

Figure 5.2 Stable lofting of a two-particle bed (Run 26).

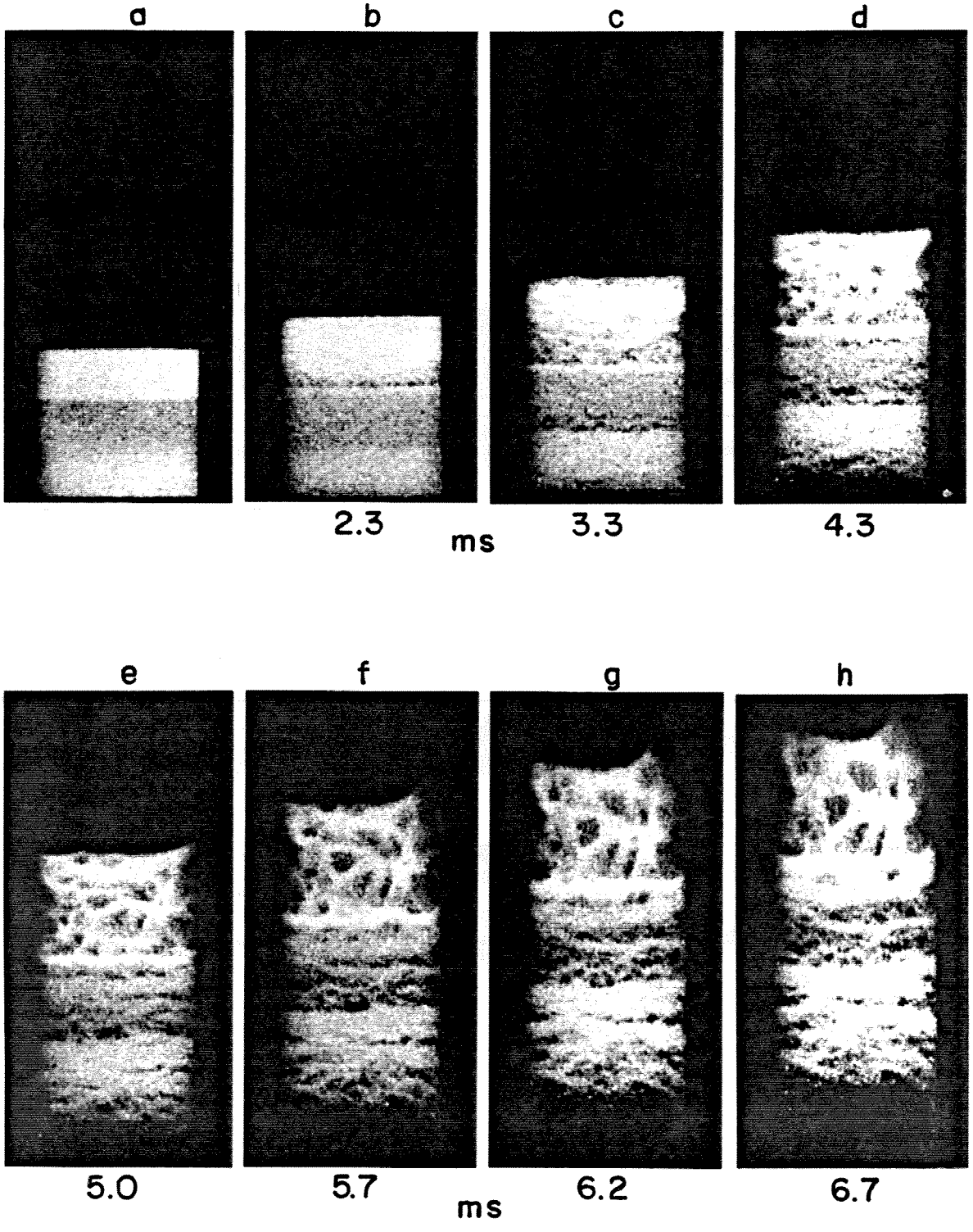

Figure 5.3 Unstable lofting of a three-particle bed (Run 27).

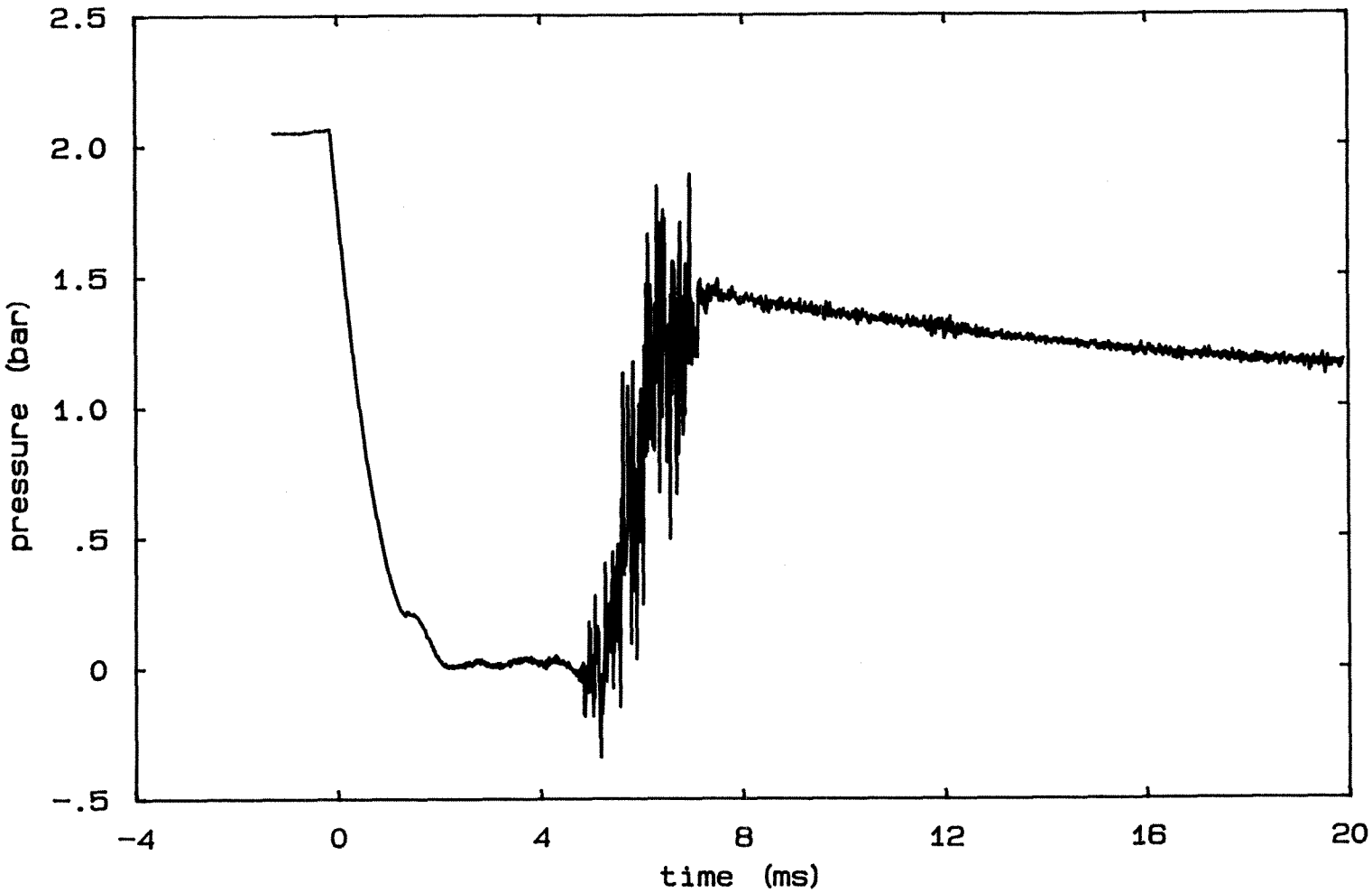

Figure 5.4 Pressure history 1.9 cm above the three-particle bed stacked for stable lofting (Run 25).

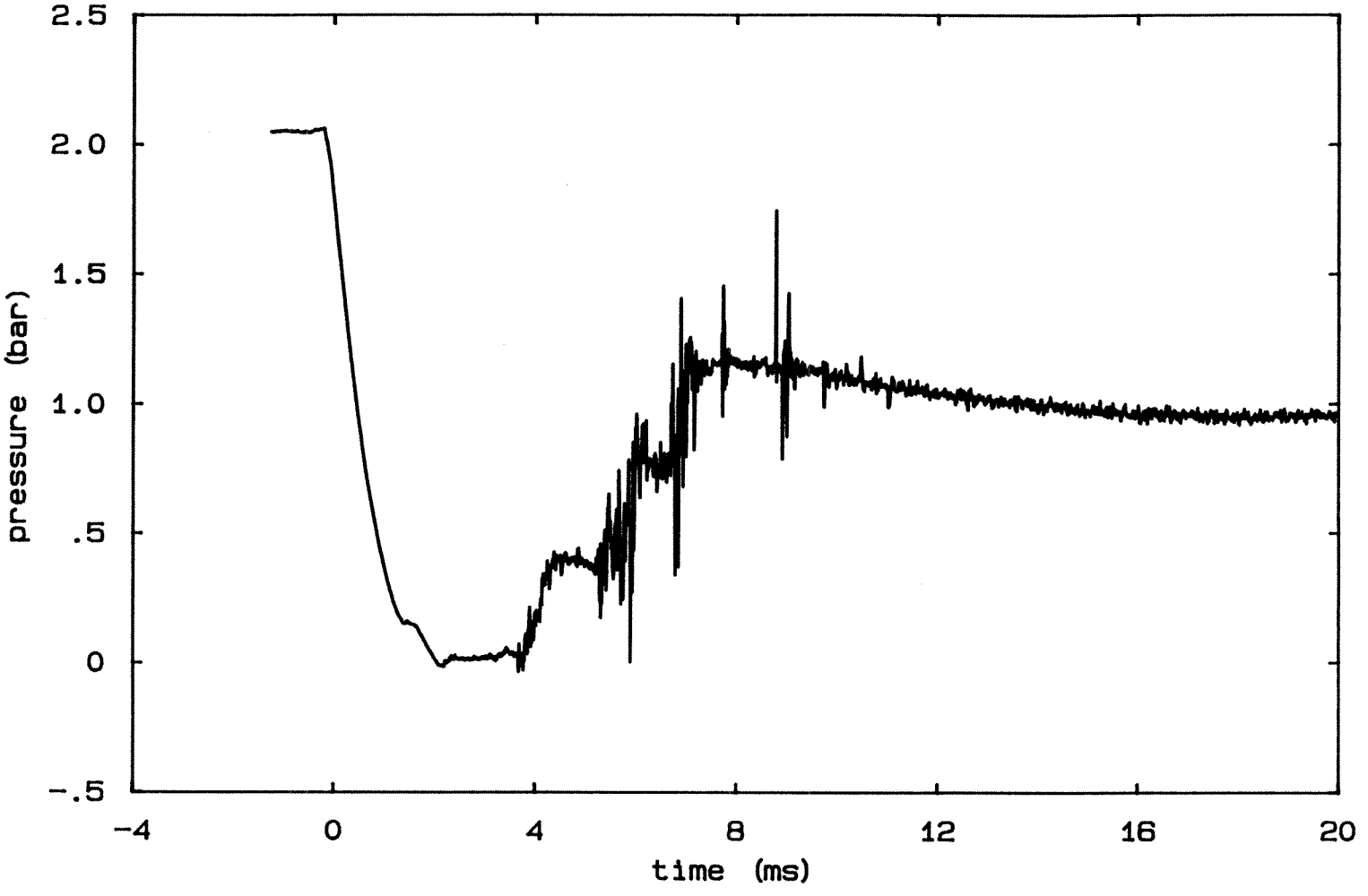

Figure 5.5 Pressure history 1.9 cm above the three-particle bed stacked for unstable lofting (Run 27).

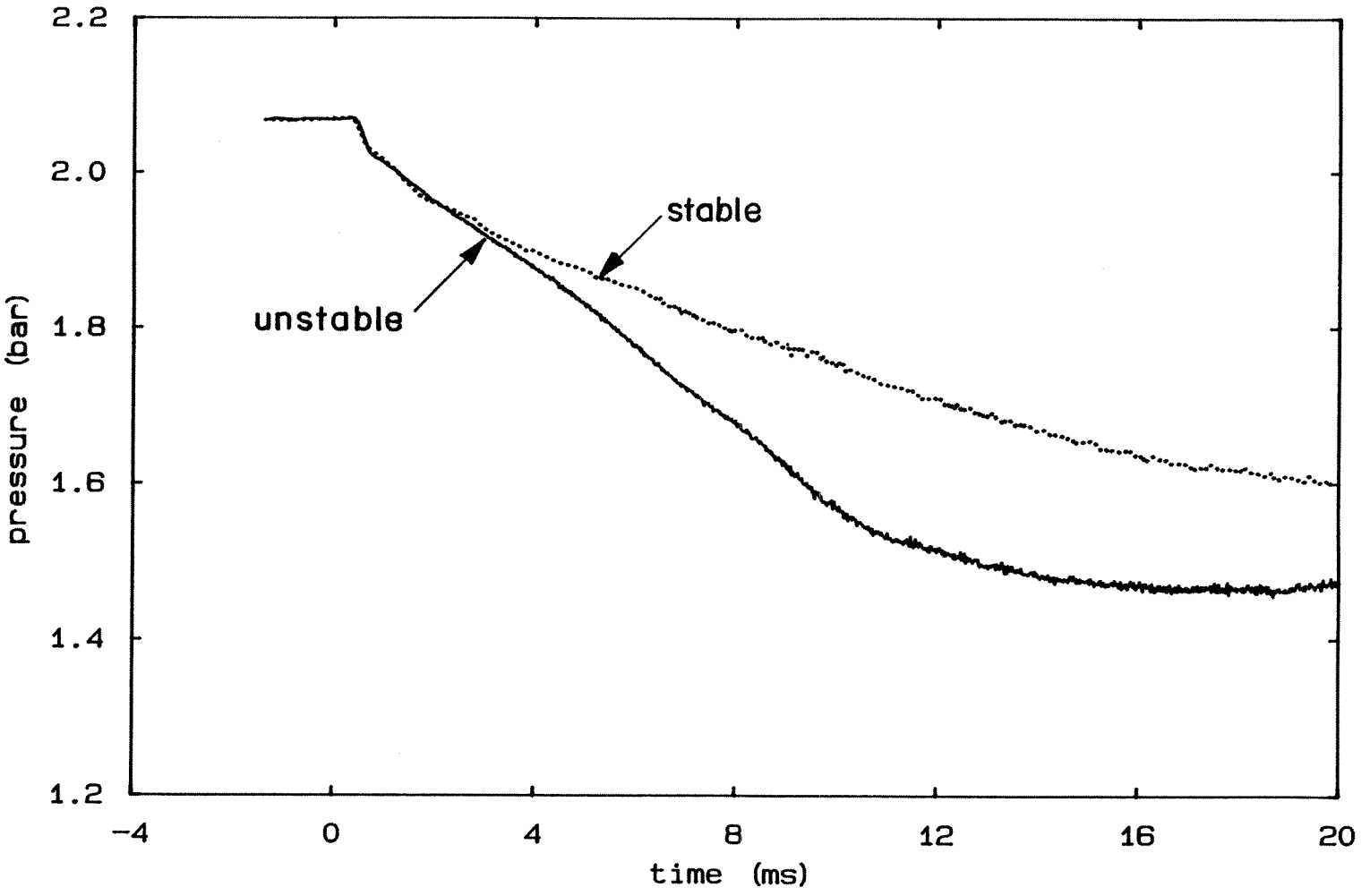

Figure 5.6 Pressure history below the three-particle bed for stable and unstable lofting (Runs 25,27).

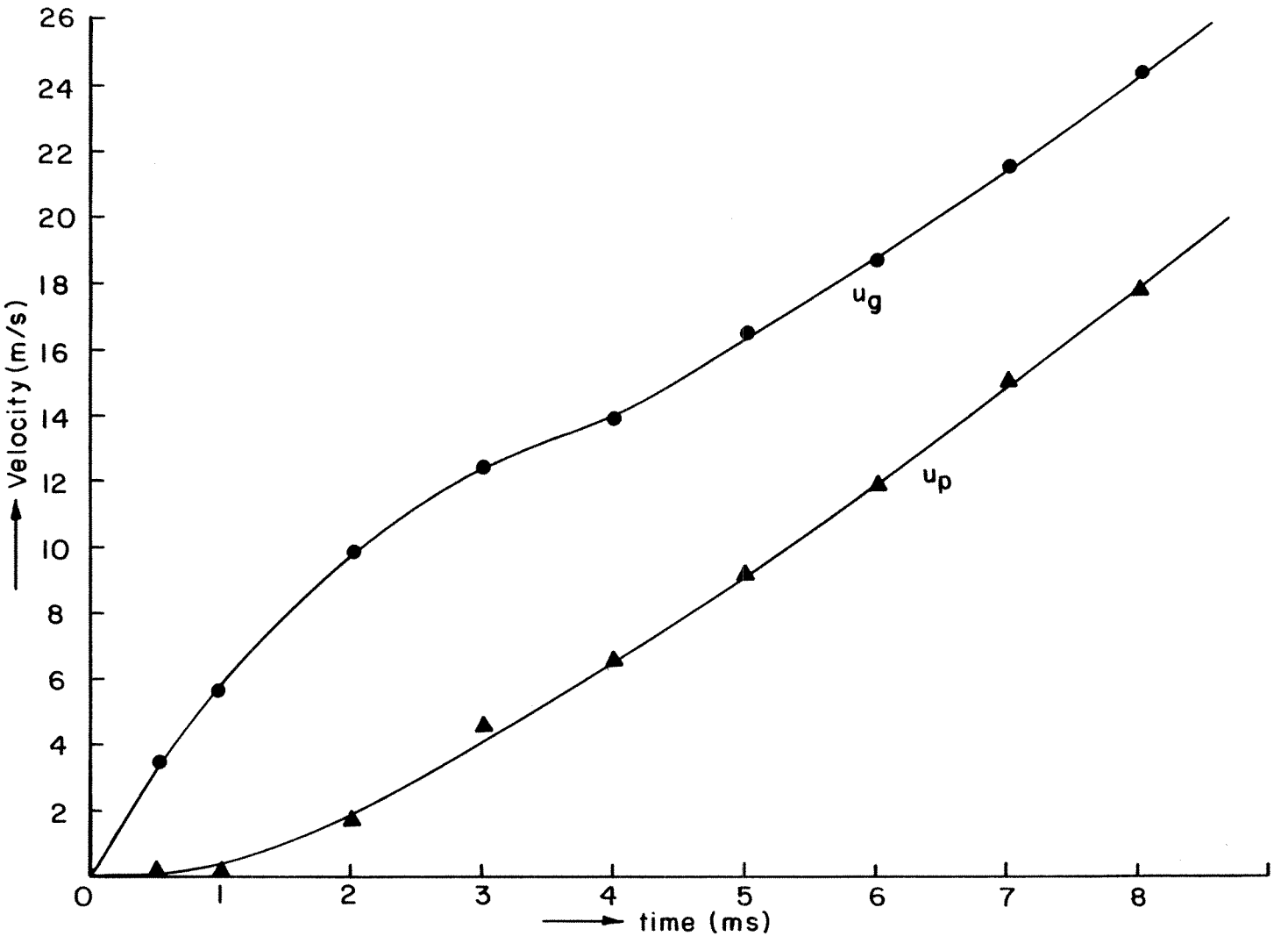

Figure 5.7a Fluid and particle velocities: stable lofting (Run 25).

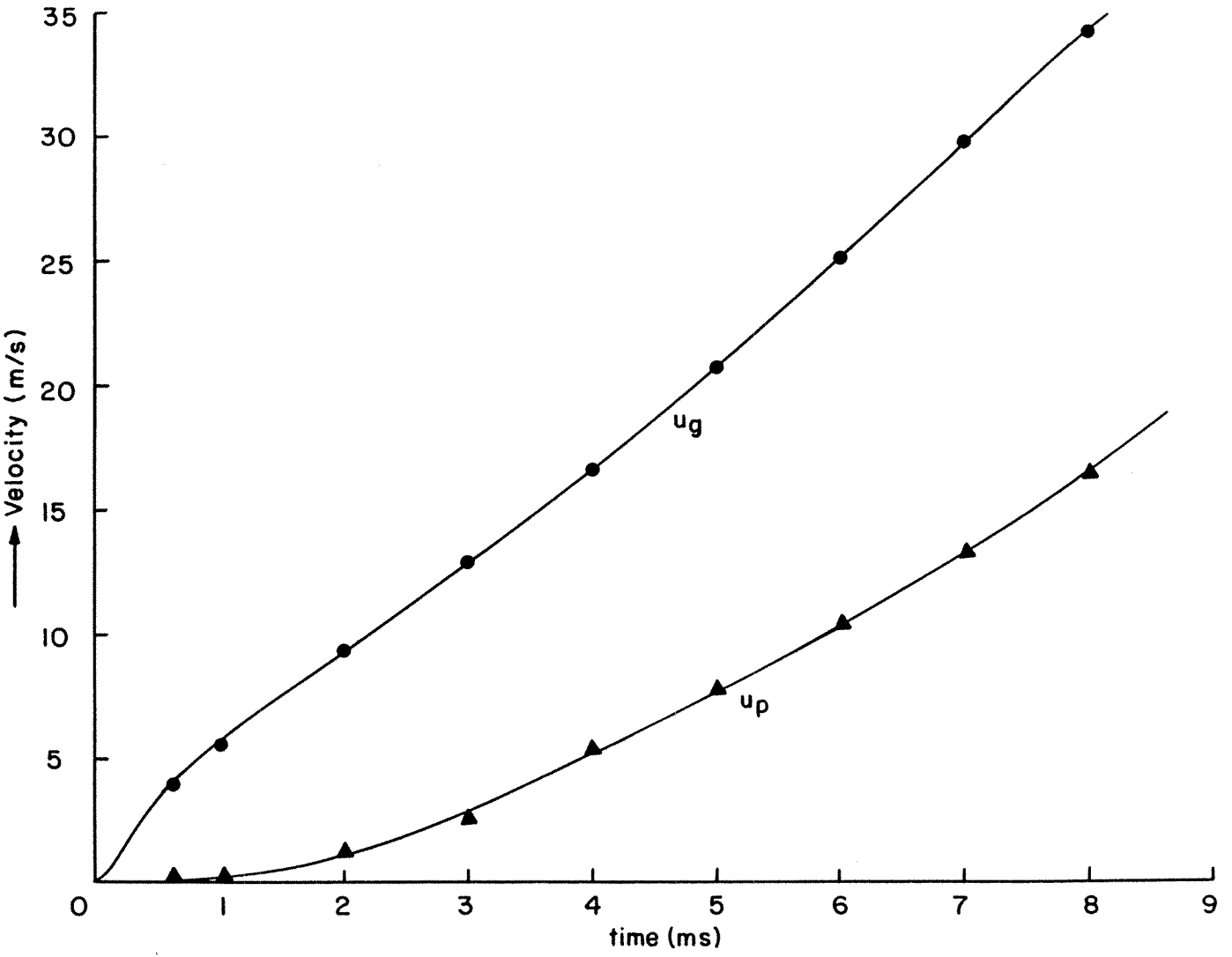

Figure 5.7b Fluid and particle velocities: unstable lofting (Run 27).

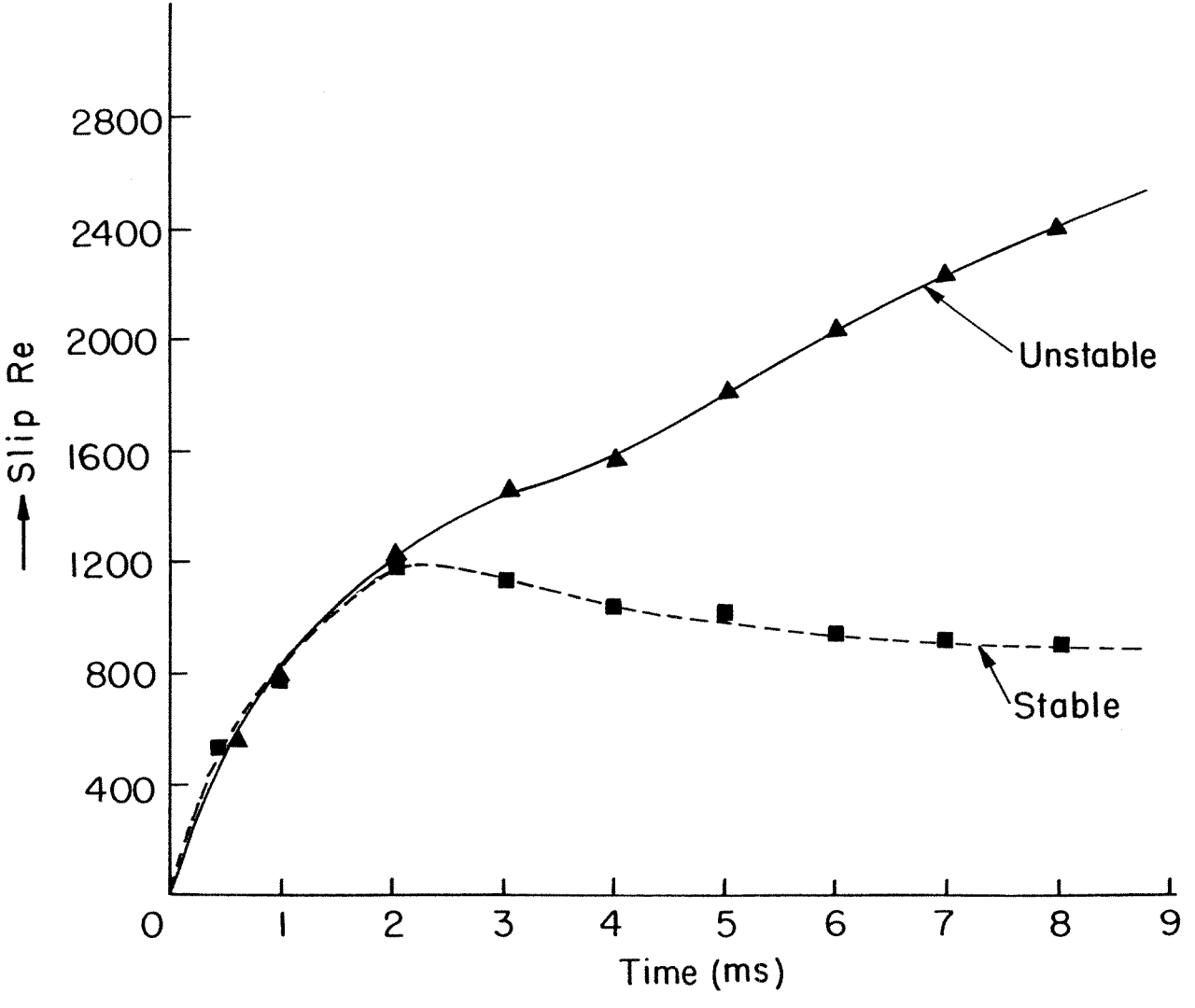

Figure 5.7c Largest particle slip Reynolds number for stable and unstable lofting of the three-particle bed (Runs 25,27).

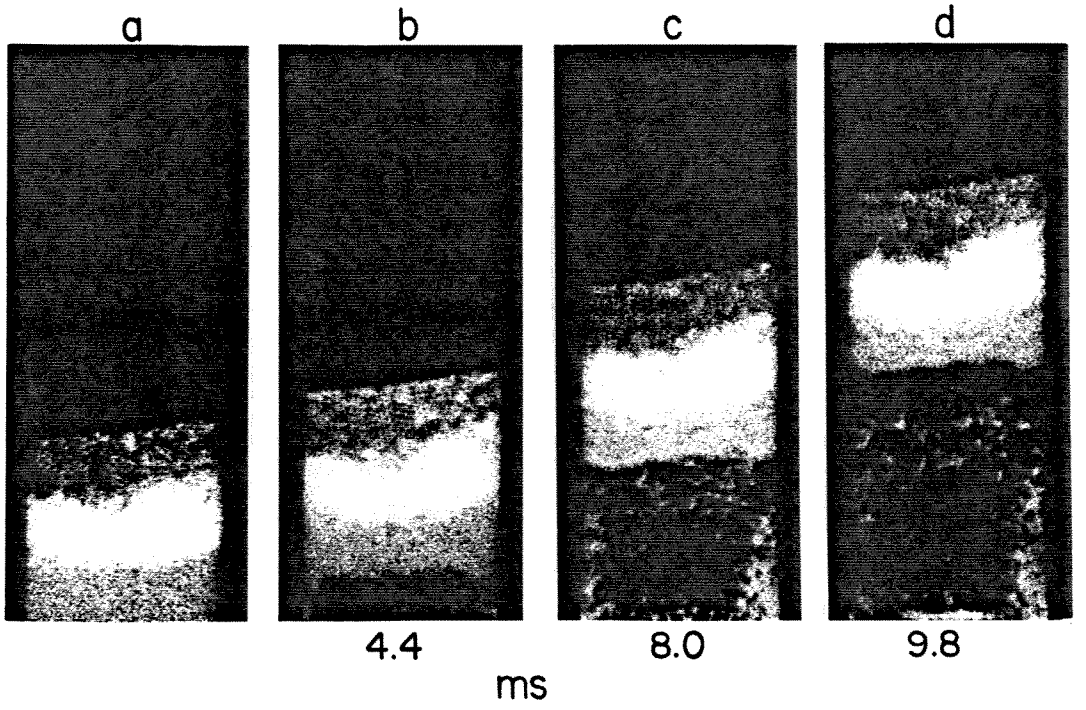

Figure 5.8 Stable lofting of a density gradient stack (Run 28).

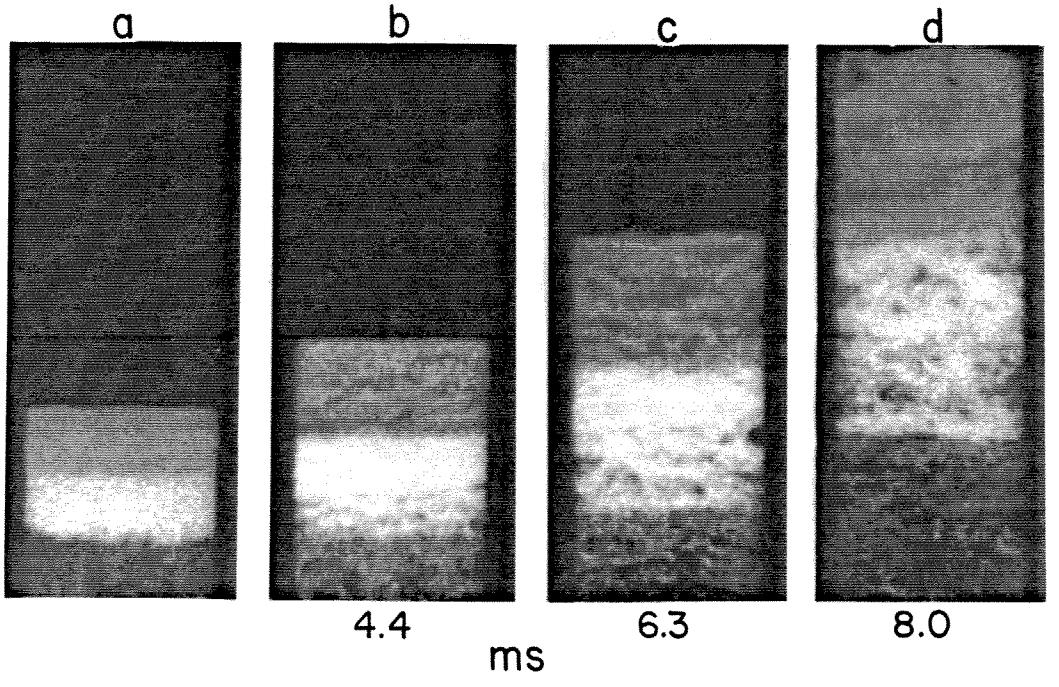

Figure 5.9 Unstable lofting of a density gradient stack (Run 29).

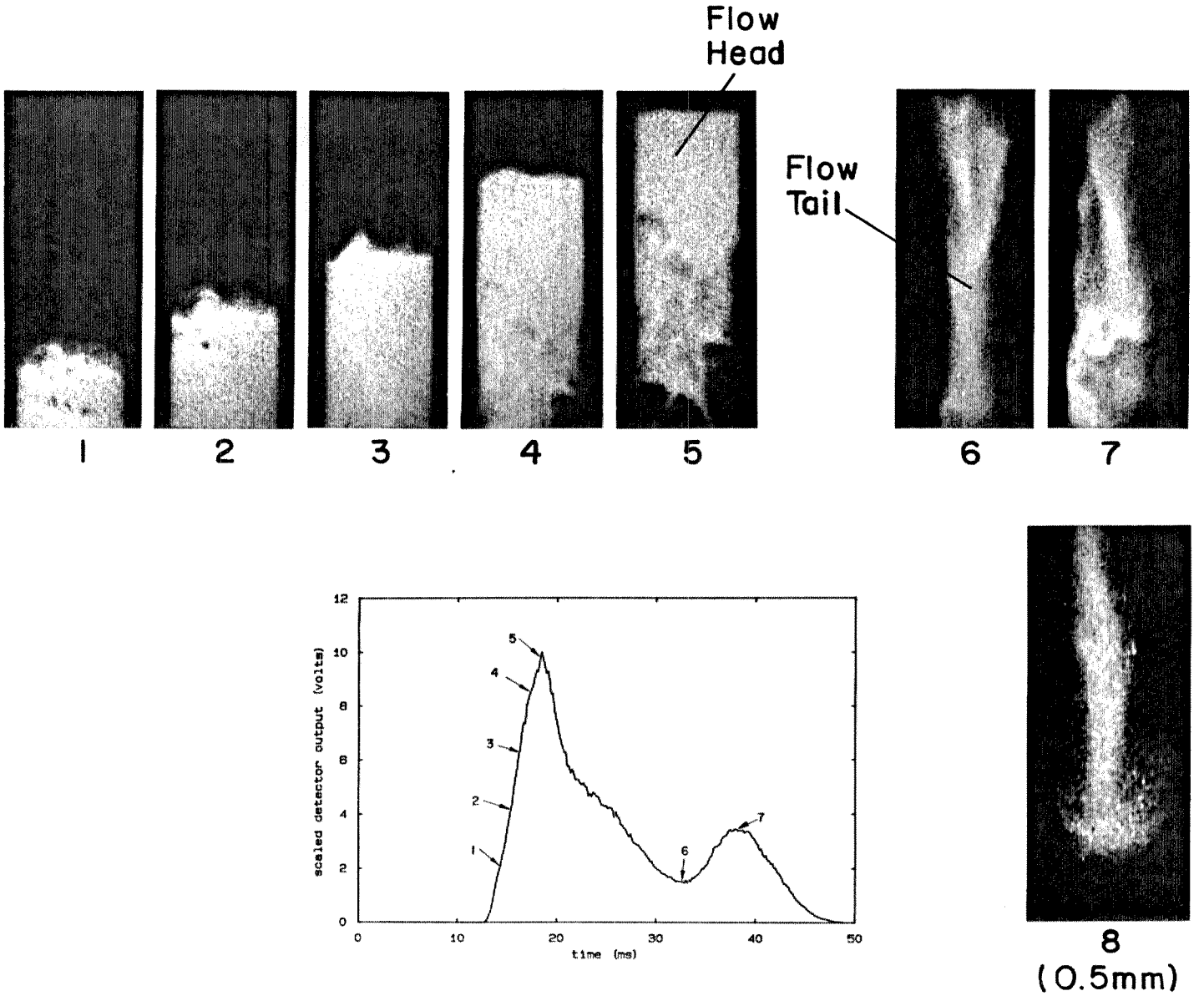

Figure 5.10 Photodiode trace and flow features for Run 15.

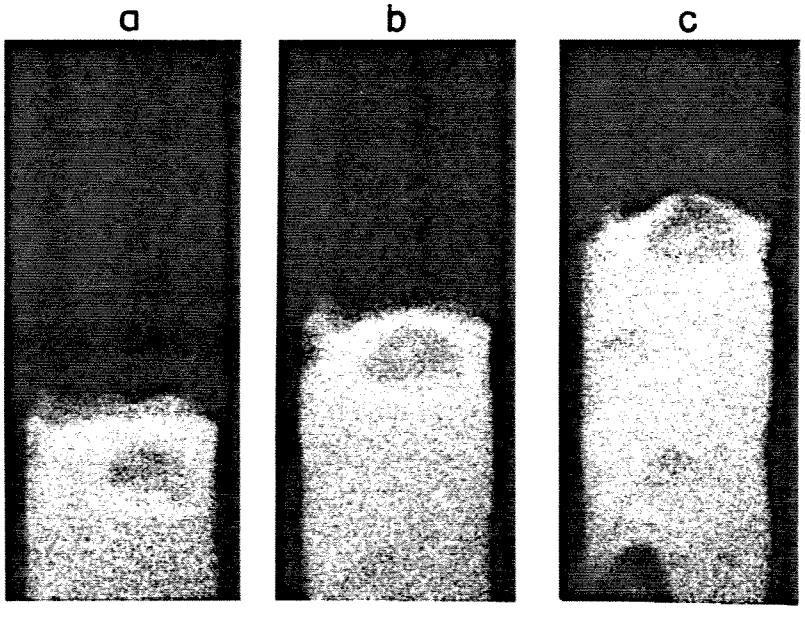

Figure 5.11 Motion of a buoyant bubble in the upper regions of a bed accelerating at 150g (Run 14) (frames 0.9 ms apart).

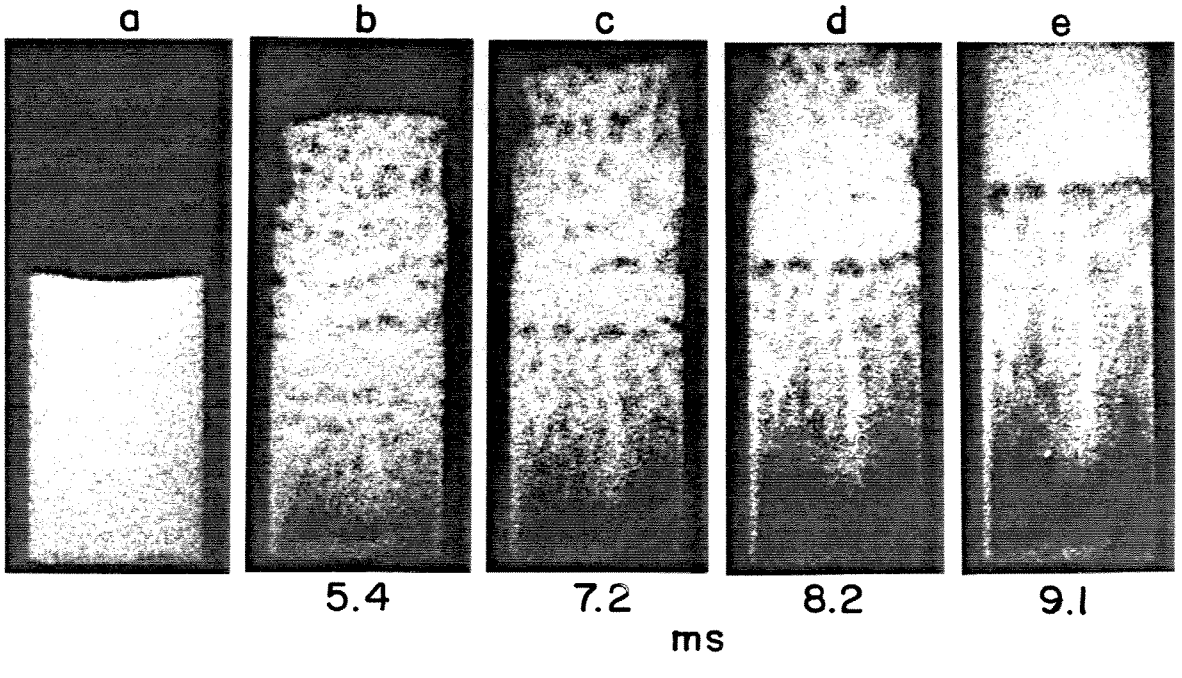

Figure 5.12 Formation of a plug in the channel (Run 19).

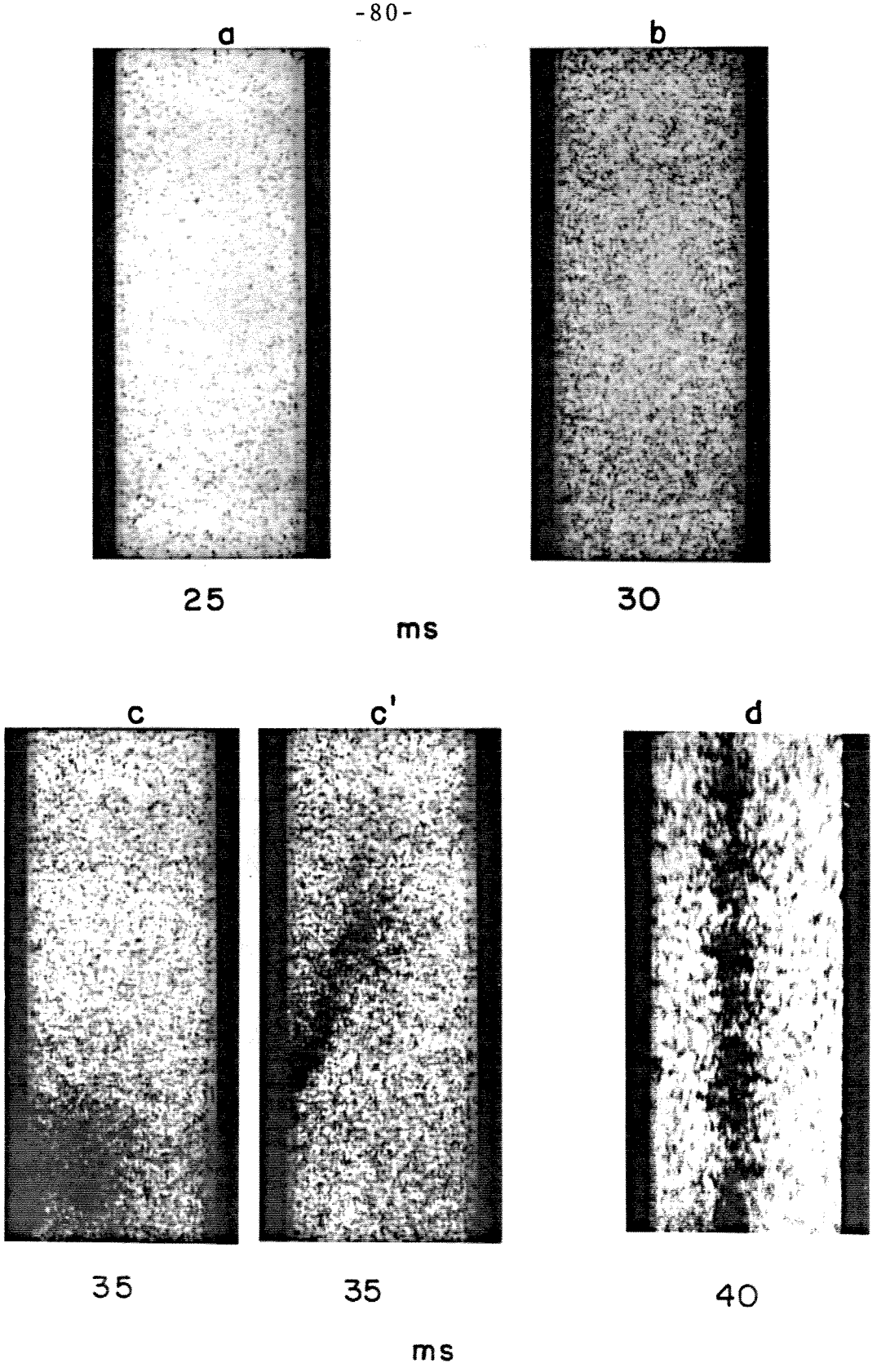

Figure 5.13 Late stages of bed expansion (Run 20).

Chapter 6

DYNAMIC PRESSURE MEASUREMENTS

6.1. Introduction.

From experiments on dusty gas generation, starting with a packed bed of particles, it is clear that the flow field is highly nonuniform and continues to remain so until high dilutions are reached. In this context, a point measure of dust density (m) would be informative.

Since the generated dusty gas flow is continuously accelerating and expanding throughout the useful test period, and not in equilibrium, a reasonable first step would be to try to make a point measurement of the dynamic pressure of the dust (DP_{dust}).

$$DP_{dust} \propto m\, u_p^2 , \quad u_p: \text{particle speed} \tag{6.1}$$

With an objective to measure the dynamic pressure of the dust, an experimental probe was designed, and its performance was cross checked with the extensive information already available through flow visualization. The flow generated was with short-to-moderate length beds ($0.5 < l_0 / D < 4$) mounted on a mesh screen in the driver section (configuration 2:, *cf.* §2.1).

6.2. The Probe.

Figure 6.1 is a schematic of the probe. It is essentially a flange carrying three transducers and is mounted in the dusty gas flow below the test-section. Transducer T1 mounted head on in the channel measures the total pressure of the dusty gas (P_{T1}); transducer T2 mounted in a sheltered configuration measures the total pressure of the gas phase (P_{T2}) as the dusty gas flow enters a *total pressure tube*; and transducer T3 is a conventional wall transducer measuring the static pressure (P_{T3}) in the flow. The transducers used are PCB 112A21 devices (see §2.2). The

surface of T1 is protected with a 0.5 mm thick layer of RTV 511 coating.

The configuration for transducer T2 is based on the design of Dussourd and Shapiro (1958) who developed a probe to measure the total pressure of the gas phase in an equilibrium flow of gas and particles. As the dusty gas flow enters the *total pressure tube* the gas phase stagnates while the particles, due to their inertia, continue to move in the tube. The pressure tap to transducer T2 is located very close to the inlet of the tube, and this minimizes the effects of drag interactions between the stagnant gas and the particles within the tube. The length of the *total pressure tube* is about the starting length of the bed and its inside dimension is about ten particle diameters.

The difference between the two measured total pressures gives the dynamic pressure of the dust phase (DP_{dust}), and the difference between the total pressure of the gas and the static pressure gives the dynamic pressure of the gas phase (DP_{gas}).

$$DP_{dust} = P_{T1} - P_{T2} = k_1 \, m \, u_p^{\,2} \tag{6.2}$$

$$DP_{gas} = P_{T2} - P_{T3} = k_2 \, \rho_g \, u_g^{\,2} \tag{6.3}$$

where k_1 and k_2 are calibration constants for the dust phase and gas phase dynamic pressure measurements. The constant k_2 can be obtained through an independent estimate of the dynamic pressure of the gas as is possible from a knowledge of the fluid entry conditions into the bed (appendix C). The constant k_1 can be obtained only through an independent measure of dust density like through radiographic techniques, and dust velocity through motion-picture photography.

If the dusty gas flow is in equilibrium, then $u_p \sim u_g$ and an estimate for mass loading (M) would be:

$$M = m/\rho_g = \frac{k_2}{k_1} \frac{DP_{dust}}{DP_{gas}} \tag{6.4}$$

6.3. Results : *Typical Total Pressure Traces.*

Figure 6.2 is a probe pressure history for a 5.1 cm bed of 0.25 mm glass beads located 30.5 cm below the probe and operated at 2.0 bar pressure (Run 21). Interestingly, the two total pressure traces overlap each other in the gas flow till the arrival of the dusty flow. The salient features of the measurement are i) most of the dynamic pressure contribution comes from the dust phase, and ii) the distribution of the dust medium is highly nonuniform, and it is concentrated in dense structures which cause the characteristic high amplitude bumps (1, 2) as they impact on the transducer.

Since the dynamic pressure of the gas is quite low, it will be difficult to make an accurate measurement of it; especially since the transducer records are noisy due to particle impacts. Also, a point probe just making the two total pressure measurements should in itself be very useful.

The dynamic pressure of the dust at level 1 (Figure 6.2) is 1.25 bar and level 2 is 1.75 bar. The dust phase velocity measured during the early times of arrival (~17 ms) is 36 m/s. Assuming $k_1 \sim 0.5$, the dust density at level 1 is 190 kg/m^3, and at level 2 is 270 kg/m^3. An average dust density of 230 kg/m^3 will correspond to a dust volume fraction of about 9%. The gas density at early times of arrival is about 1.9 kg/m^3, and this leads to an average dust loading of 120 in the dense dusty flow.

Figure 6.3 is the total pressure history showing the early stages of bed disassembly for the same 5.1 cm bed of 0.25 mm glass beads now located 12.7 cm below the probe (Run 22). The main features depicted here are i) the typical expansion profile of the dust dynamic pressure distribution owing to the higher flow

speeds at the bed top than at the bottom, and ii) the interesting response of the two total pressure transducers to a growing bubble wherein the pressure traces overlap with each other (*cf.* §4.2.2).

Figure 6.4 is a total pressure history 51 cm above a shorter bed (2.5 cm) of 0.25 mm glass beads, operated at 2.0 bar pressure (Run 23). The data here have been presented from the time of arrival of the dusty gas and onwards. The fluctuations in the dynamic pressure of the dust phase have definitely reduced owing to the dilution of the flow, and the flow field is approaching uniformity.

Figure 6.5 is the total pressure history 61 cm above an even shorter bed (1.25 cm) of 0.25 mm glass beads at 4.0 bar operating pressure (Run 24). The loading is progressively higher as the flow comes by, and the flow definitely looks uniform (*cf.* §5.8.1). An estimate of the mass loading (M) of the dust between 26 and 30 ms would be as follows:

$$DP_{dust} \text{ (measured: figure 6.5)} \approx 0.87 \text{ bar} \equiv k\, m\, u_p^{\,2}\ ;\ k \sim 1/2 \text{ (assumption)}$$

$$DP_{gas} \text{ (estimated: appendix C)} \approx 0.16 \text{ bar} \equiv 1/2\ \rho_g\ u_g^{\,2}\ ;$$

$$\text{assuming equilibrium flow } u_p \sim u_g\ ; \quad M = m/\rho_g \approx 5.4$$

The gas density is about 4.3 kg/m^3, and the corresponding dust density is about 23 kg/m^3 leading to a dust volume fraction of about 0.9 % in this dilute flow.

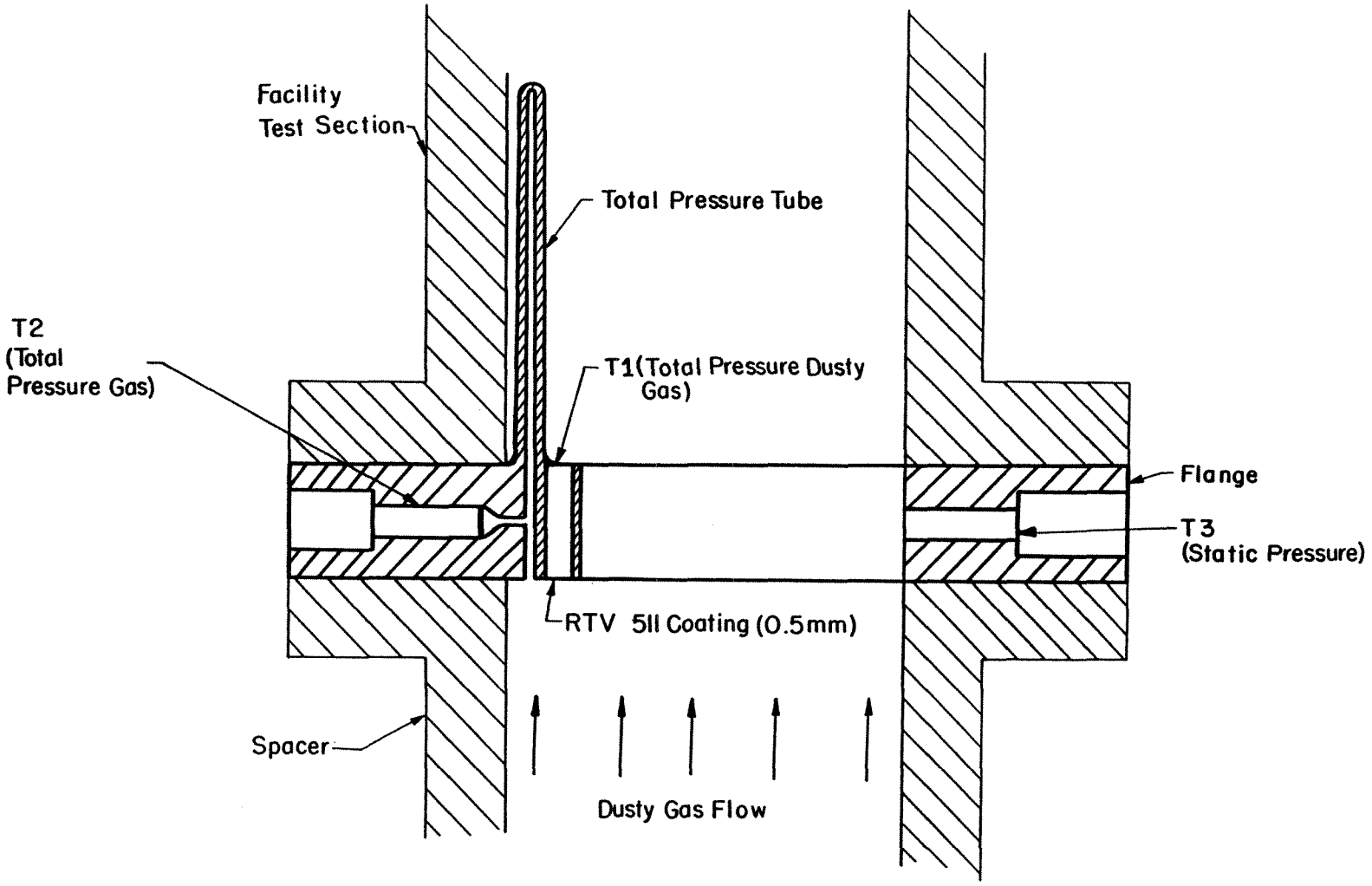

Figure 6.1 Schematic of dynamic pressure probe.

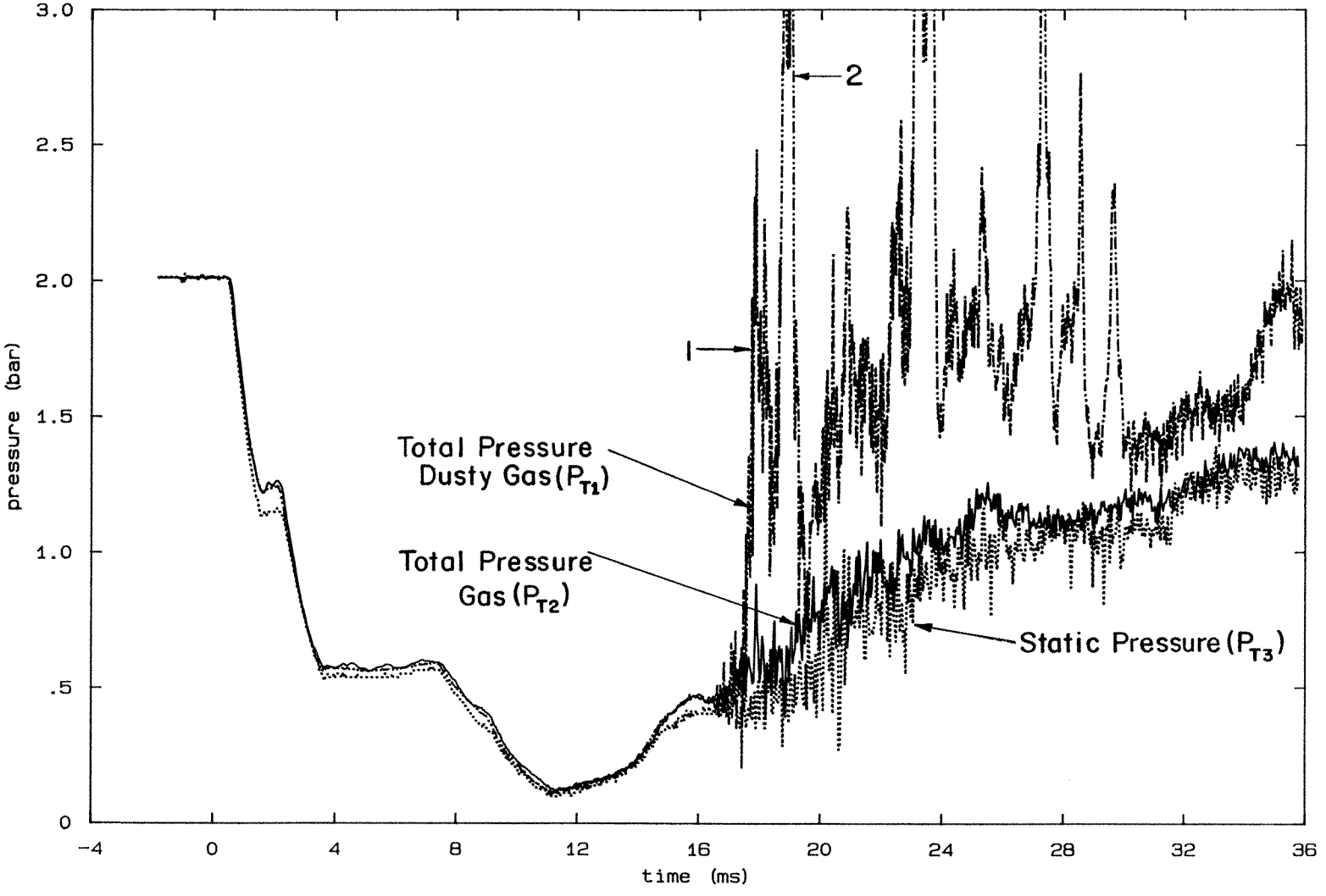

Figure 6.2 Probe history (Run 21).

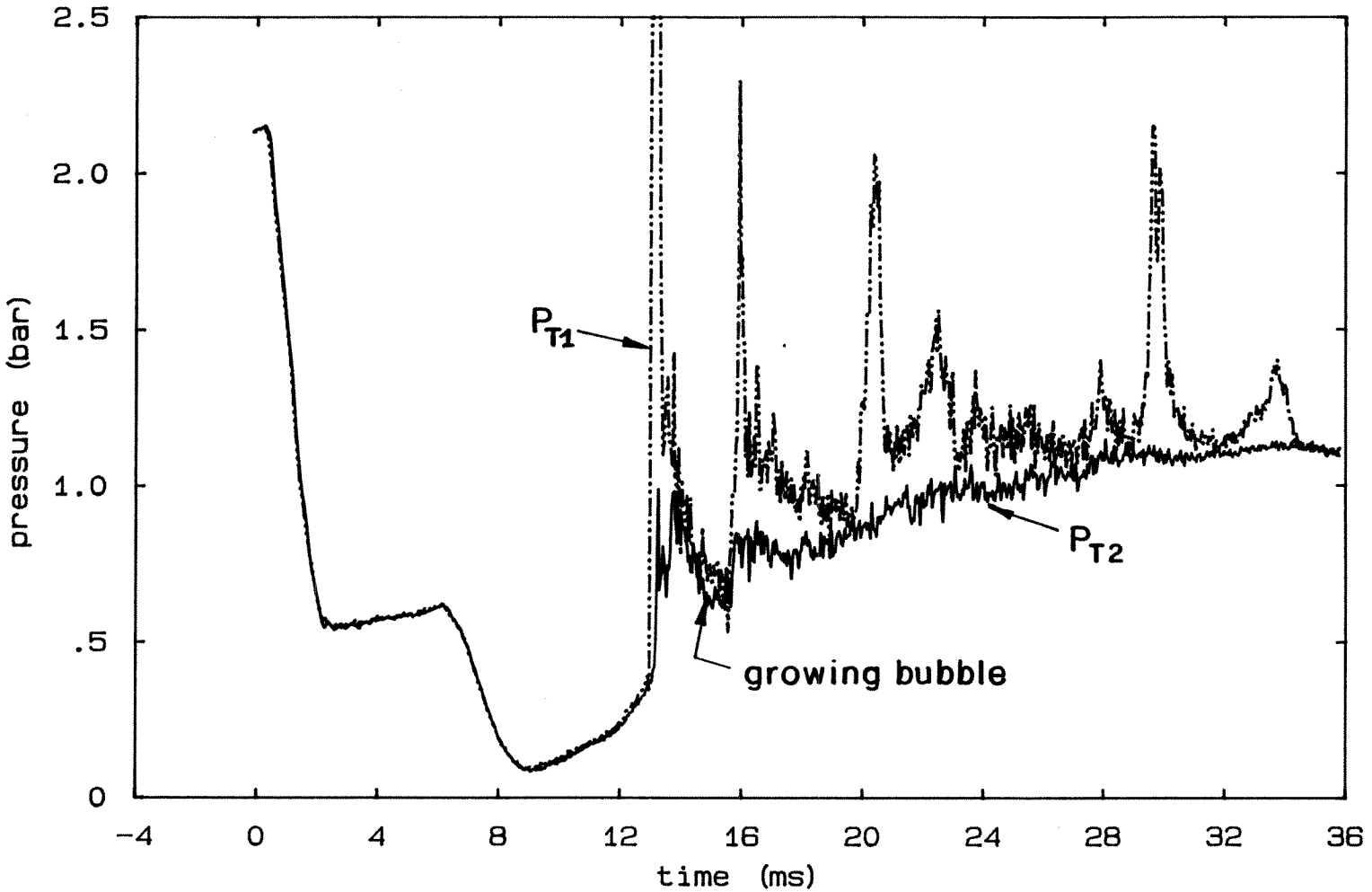

Figure 6.3 Total pressure history (Run 22).

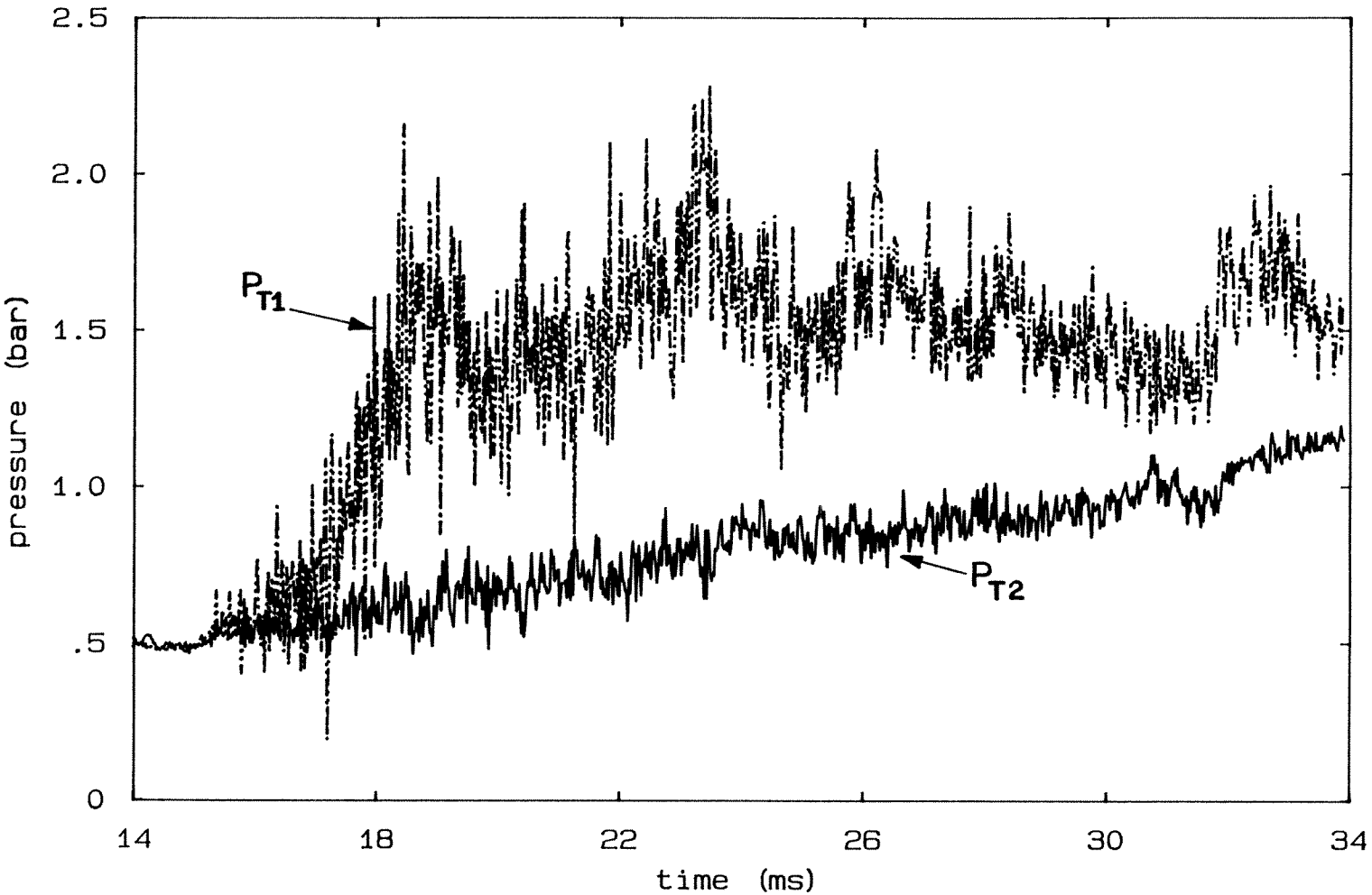

Figure 6.4 Total pressure history (Run 23).

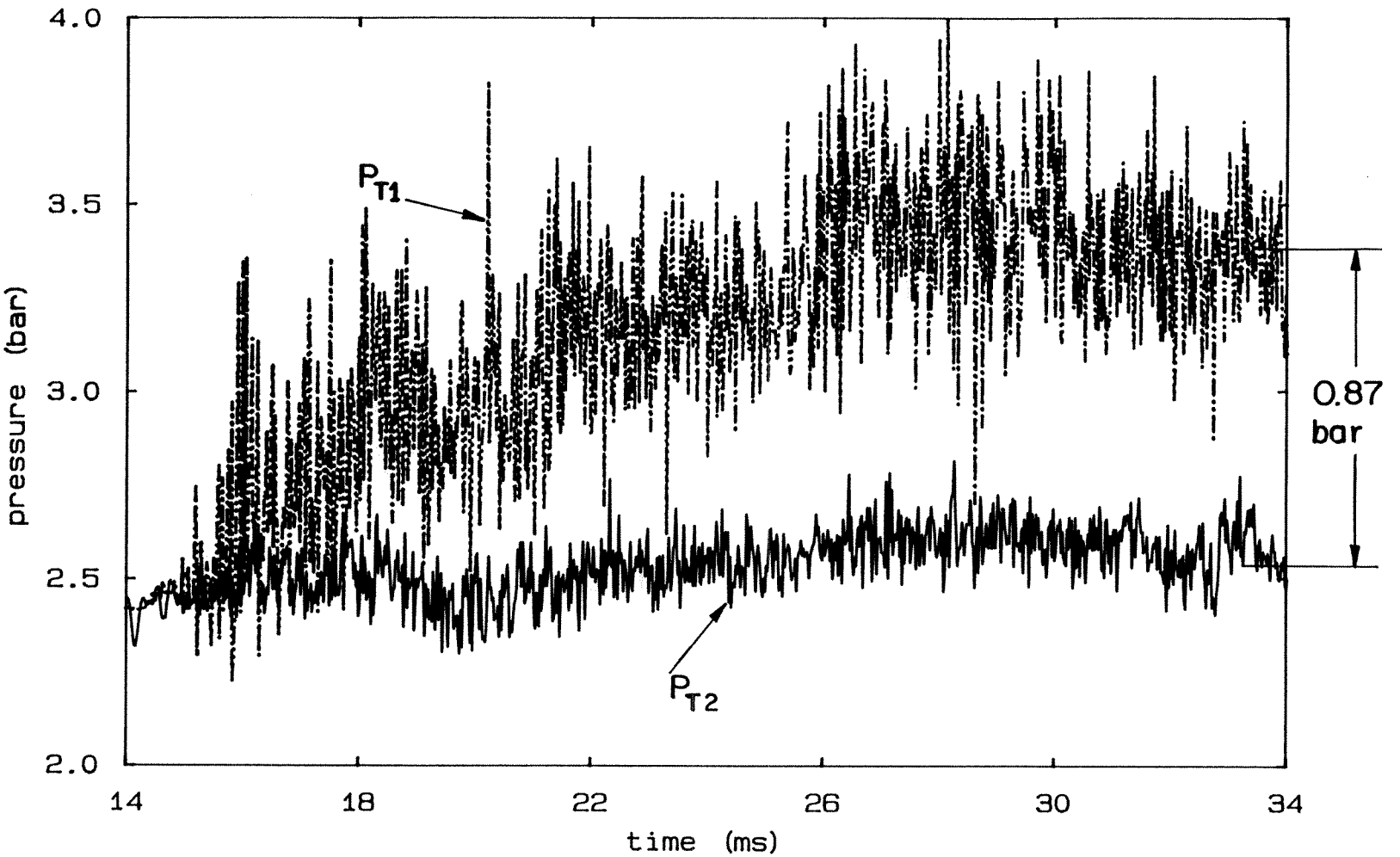

Figure 6.5 Total pressure history (Run 24).

Chapter 7

CONCLUSION

An experimental study of the flow of high-speed dense dusty gases was conducted in a novel shock tube facility. The flow was generated through rapid depressurization and subsequent fluidization of a packed bed of particles loaded under pressure in the vertical driver section of the shock tube. Glass beads, plastic beads, metal beads and ignimbrite volcanic ash were used in the experiments.

Two lofting configurations of packed beds were set up. In the first configuration, the rapid depressurization of the interstitial bed fluid and the consequent initiation of bed expansion was examined. During rapid depressurization, particle layers are subjected to tremendous accelerations for short durations. At 3.1 bar diaphragm burst pressure, the top layers of a bed of 0.125 mm glass beads experience an average acceleration of 275 g in the first five milliseconds following initiation of depressurization, and reach asymptotic speeds of 15 m/s. At 2 bar diaphragm burst pressure, the top layers experience an average acceleration of 150 g and reach speeds of 7.5 m/s. The speeds of the top layers of the bed are independent of particle size. The lower layers of the bed are accelerated to lower speeds as compared to the top layers and, in fact, the bottom layers of the bed do not loft.

The initiation of bed expansion occurs along horizontal fractures, that apparently are a consequence of an inherent instability of high-density particle systems; the detailed mechanism of operation of which is yet to be understood. The fractures partition the bed into slabs. The thickness of the slabs is proportional to the square root of particle size. Typically, for 0.125 mm dia beads the slabs are 2.8 mm thick. The fractures grow vertically. While the bed is still accelerating, particles rain down from the bottom surfaces of the slabs partitioning the fractures into bubbles with a characteristic honeycomb pattern. This observed instability of the

bottom surfaces of the slabs is analogous to the Rayleigh-Taylor instability observed in continuous media. The partitioning of the fractures occurs earlier for smaller particles. Interestingly, the initial size of the bubbles, in contrast to that of the slabs, is proportional to particle size; the initial bubble width being about 25 particle diameters. For 0.125 mm dia beads the bubbles are 3.1 mm in width. The bubbles eventually compete and the dominant ones prevail. In general, beds with smaller particles show more nonuniformities owing to the smaller scales of the nonuniformities. In configuration 1, since bed accelerations operate only at small times, there is no upward motion of the bubbles along the bed. Also, the flow development here is not influenced by any wall effects.

The second lofting configuration is a high-speed fluidization configuration. Here, the role of the fluid entering from below the bed, in continuing the bed expansion initiated during the rapid depressurization of the interstitial bed fluid, was examined. In this configuration, the entire bed is lofted. The flow field is continuously accelerating and expanding throughout the test time of about 44 ms. Operating with a 7.6 cm deep bed of 0.18 mm glass beads at 2 bar diaphragm burst pressure, the top regions of the flow reached speeds of 46 m/s in 25 ms, representing an average acceleration of 185 g. Operating with 1.25 cm bed of 0.5 mm glass beads at 2 bar diaphragm burst pressure, flows reached speeds of 60 m/s in 25 ms, representing an average acceleration of 240 g.

The typical flow field in configuration 2, at late stages, is dense and highly nonuniform, characterized by the simultaneous presence of dense filamentary structures and dilute dispersions of particles. Depending on operating bed heights and particle sizes, the flow in the upper regions of the bed at late stages, can be classified into four different categories characterized by: i) growing bubbles; as the bubbles expand and elongate, the bubble walls are stretched resulting in a flow with dense filamentary structures, ii) nongrowing bubbles that rapidly migrate to the free surface of the bed, iii) a flow head resulting from the repacking of the bed material

in the upper regions, and iv) a flow plug in the channel resulting from the repacking of the entire bed material. The results of the experiments done at fixed pressure (2 bar) are shown in Figure 7.1. The boundaries represent approximate demarcations between the four different flow types. The bed heights and particle sizes have been non dimensionalized with the channel width, which in the current experiments is fixed. The dependence of flow characteristics on channel width is not known. Approximately, for a bed height to particle size ratio below 440, the fluidization is complete. Keeping the particle size the same, as the operating bed height is increased, the tendency for the material to consolidate at the top regions of the bed increases until finally the whole bed repacks. The through flow past flow heads and flow plugs is quasisteady in nature and the flow velocity has been estimated using the Ergun equation for flow past porous media. Particle size and particle density have essentially the same effect on the quality of fluidization.

Only the late stages of flow development in configuration 2 are influenced by wall effects. Wall effects manifest as faster moving fluid along the walls and denser accumulation of the flow structures towards the center of the channel. The bottom of the dusty flow, at these late stages, is characterized by the presence of a flow tail; formed by the accumulation of the particles initially shed at the bed bottom. The distorted fluid velocity profile with higher fluid velocities closer to the walls results in the erosion of the nearby flow structures and the consequent peeling off of the particles. Thereby, the dusty flow goes through a continuous dilution process. The dusty flow is nonuniform until very high dilutions were reached. The development of the flow field is not influenced by any electrostatic forces of interactions between particles.

The fluidization mechanics is strongly influenced by the presence of a gradient in acceleration, set up by stacking particles of different size or density or both, in the stationary bed prepared for lofting. Typically, a size stacking with the smallest beads, which accelerate the fastest in a given fluid flow, arranged at the bed bottom

and the largest beads arranged at the bed top, is extremely stable and the bed lofts like a plug. The reverse stacking, with the largest beads at the bed bottom and the smallest beads at the bed top, is extremely unstable and the bed rapidly expands. An experiment, with a 3.8 cm stacked bed of 0.25 mm, 0.5 mm and 0.75 mm glass beads at 2 bar diaphragm burst pressure yielded the following results. In stable lofting, despite large initial differences in fluid and particle velocities, the through flow quickly approaches quasisteady conditions with the slip Reynolds number asymptoting to around 900, 8 ms after initiation of the experiment. In unstable lofting, the Reynolds number continuously increases as the bed expands, reaching values of 2400 during the first 8 ms of the experiment.

A multi-transducer probe was installed in the dusty flow, generated in configuration 2, and dynamic pressure measurements were made in the flow field. All the observed features of the flow field can be characterized with the probe. A typical dusty flow with dense filamentary structures has an average dust density of 270 kg/m^3 with a corresponding dust volume fraction of 9%. A dilute dusty flow has a dust density of 23 kg/m^3 with a corresponding dust volume fraction of 0.9%.

The results of the above experiments have shown that high-speed dusty gas flow fields, excepting packed plug flows and very dilute particle flows, are extremely nonuniform. This should provide insights into modeling such flow fields. Also, quantitative measurements of the average density of the flow field, during the various stages of development, would be useful.

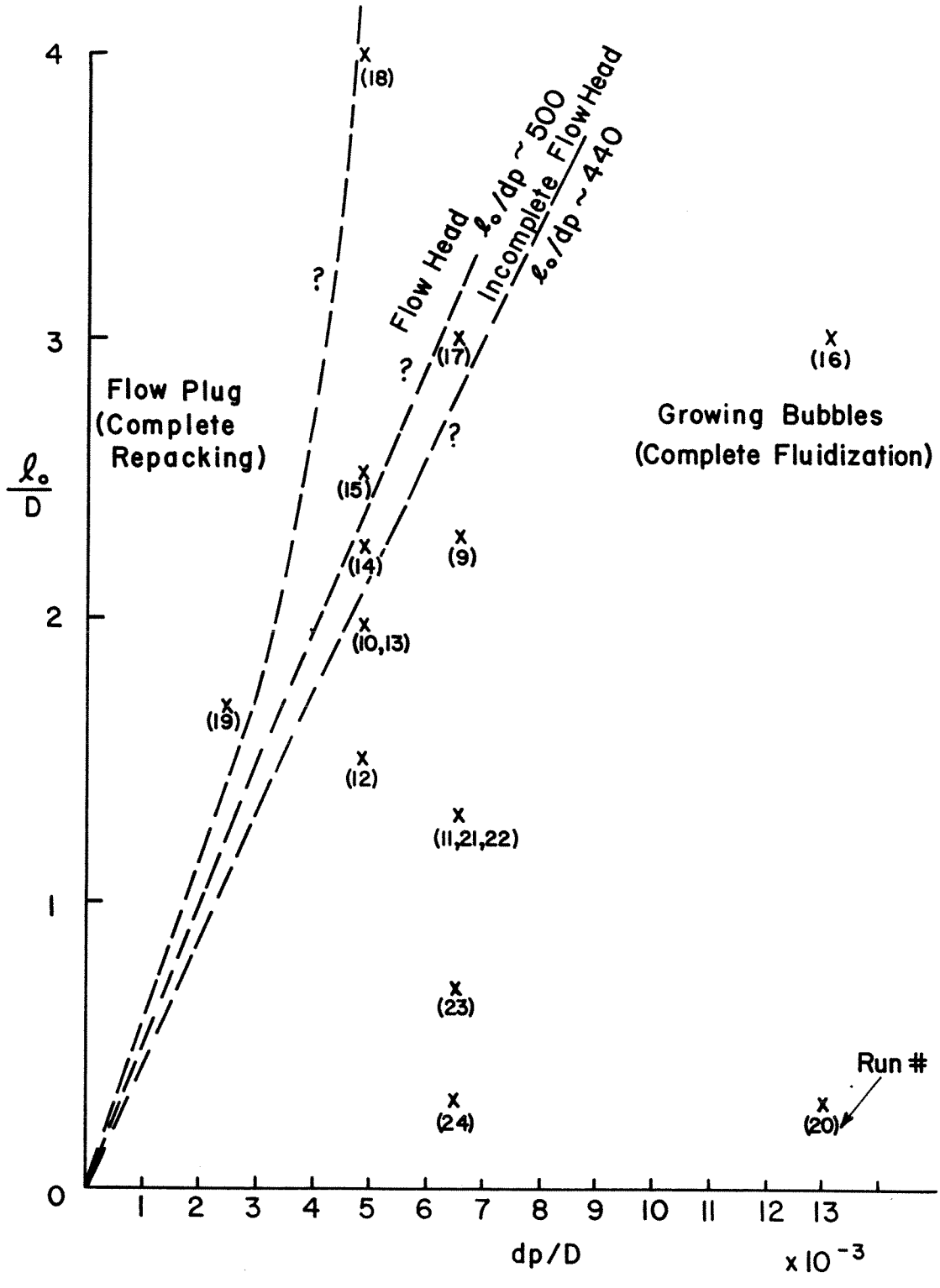

Figure 7.1 Approximate demarcations between different types of flows observed in configuration 2.

Appendix A

MICROPROCESSOR CONTROL

A microprocessor based control system was designed to handle the accurate timing needs of the experiment at different stages. It consists of a control unit and a trigger unit.

A.1. THE CONTROL UNIT.

Started by a trigger pulse, the control unit generates a specific number of timing pulses at a certain frequency and after a certain delay. This unit provides an elegant software based control of the experiment. It essentially consists of a microcomputer system that communicates with a peripheral device.

A.1.1. **Organization.** The microcomputer system was assembled from the Intel MCS/85 kit, and this was expanded to include *latches* (Intel 8212) and *buffers* (Intel 8216) to demultiplex the address and data busses and facilitate interfacing. A peripheral device, the *programmable interval timer* (Intel 8254), was interfaced to this system.

The 8254 has three 16 bit presettable downcounters (*counter* 0, 1, 2), independent in operation and software compatible. The counters can operate in six different programmable modes, *viz.*:

1. Mode 0 : interrupt on terminal count,
2. Mode 1 : hardware retriggerable one-shot,
3. Mode 2 : rate generator,
4. Mode 3 : square wave mode (rate generator),
5. Mode 4 : software triggered strobe,
6. Mode 5 : hardware triggered strobe.

Each counter communicates to the outside through the *clock, gate* and *out* terminals (Figure A.1). *Gate* is a control terminal for enabling and disabling the

counting of the respective input clock pulses. The *gate* input is sampled on the rising edge, and the counters are decremented on the falling edge of the input clock pulses.

Communication with the 8254 begins with the *control word register* into which the *control words* defining the operation of the counters are written. The initial counts are written into the respective counters.

Interfacing the 8254. Figure A.1 shows the arrangement. The data terminals D_{0-7} are connected to the respective system data bus lines, so are address lines A_0, A_1 and control lines $\overline{RD}$ & $\overline{WR}$. The chip select $\overline{CS}$ is drawn from the upper eight address lines A_{8-15} (FF in hex).

The main system clock running at 3.072 MHz. is stepped down by 10 to accommodate the time ranges of interest. *Counter* 0 has been chosen for delay operation (mode 0), *counter* 1 is a rate generator (mode 3) and *counter* 2 is used for event counting (mode 0).

Auxiliary controls are *enable* which prevents stray signals during power up and *clear* for clearing all flipflops to enable them to respond to incoming trigger.

A.1.2. **Control Operation.** The 8254 is programmed before hand and waits for the *external control* signal to resume counting. The start-up of the 8254 is initiated either manually or through a suitable incoming trigger pulse drawn from sources such as *trigger unit*, digital oscilloscope (*Nicolet* 4094) *etc.* The software overhead is minimal here. *Counter* 0 is count loaded before the arrival of the trigger pulse, and a maximum error of one clock cycle (3.25 μs) can result depending on the arrival of the trigger signal. *Counter* 1 uses one clock cycle for count loading, and the first output pulse is one clock cycle (3.25 μs) longer. These are definitely negligible errors. *Counter* 2 uses the first input pulse for count loading, and hence it is programmed to count one pulse less than desired.

Programming the 8254. The programming of the 8254 is elegant. The program is stored in the RAM *(Intel* 8155) of the main system. The accompanying *sample program* (table A.1) outlines the technique. First, the *control word register* is chosen (A1 A0 =11, FF03 in hex) and the *control words* defining the mode of operation of the counters are written in. The counters are next addressed and the initial counts are written in. Counters need one clock cycle for count loading. Figure A.2 depicts a *timing diagram* for a particular example, *viz.*:

delay : 308 clock cycles (1.026 ms)
frequency : 3.072 kHz (every 100 clock cycles)
number count : 2 (= 3 pulses)

Figures A.3, A.4, A.5 show the status of the output signal monitored at different stages of the microprocessor system operating with the *sample program*, using a digital oscilloscope *(Nicolet* 4094). All signals have been artificially scaled to 5 volts.

A.2. THE TRIGGER UNIT.

The trigger unit has been designed to generate a suitable trigger pulse at the initiation of the experiment. The downward traveling expansion wave, resulting from diaphragm burst, is sensed by a high-frequency response piezoelectric pressure transducer (PCB 112A21). The voltage signal from the transducer forms the input to the trigger unit.

A.2.1. **Organization.** Figure A.6 depicts the circuitry. In real time, the output from the transducer unit is suitably stepped up and compared against the set trigger level on the LM 311 *differential comparator.* Both the voltages being compared are negative here. As the expansion wave passes by the transducer, the trigger level is crossed, and the output of the comparator goes low. The falling edge is detected

by a suitable *one-shot* (74LS121) arrangement. The *one-shot* clocks a *D-latch* (74LS74) which outputs through another *one-shot*. By accomodating a *D-latch* and a *manual clear* control, stray triggering is avoided. This is especially necessary because frequent impacts of particles on the transducer during the passage of the dusty flow can generate unwanted triggers.

Table A.1. Sample Program

ADDRESS	OP CODE	DESCRIPTION
2000	21	LXI H
2001	03	A1,A0=11 (*control word register*)
2002	FF	chip select ($\overline{CS}$)
2003	36	MVI,M
2004	B0	mode for *counter* 2 (mode 0)
2005	36	
2006	76	mode for *counter* 1 (mode 3)
2007	36	
2008	30	mode for *counter* 0 (mode 0)
2009	2B	DCX H (⇒FF02)
200A	36	
200B	02	count for *counter* 2
200C	36	count 2 pulses (equiv. 3)
200D	00	
200E	2B	DCX H (⇒FF01)
200F	36	
2010	64	count for *counter* 1
2011	36	count 100 clk. cycles (frequency)
2012	00	
2013	2B	DCX H (⇒FF00)
2014	36	
2015	34	count for *counter* 0
2016	36	count 308 clk.cycles (delay)
2017	01	
2018	CF	RST 1

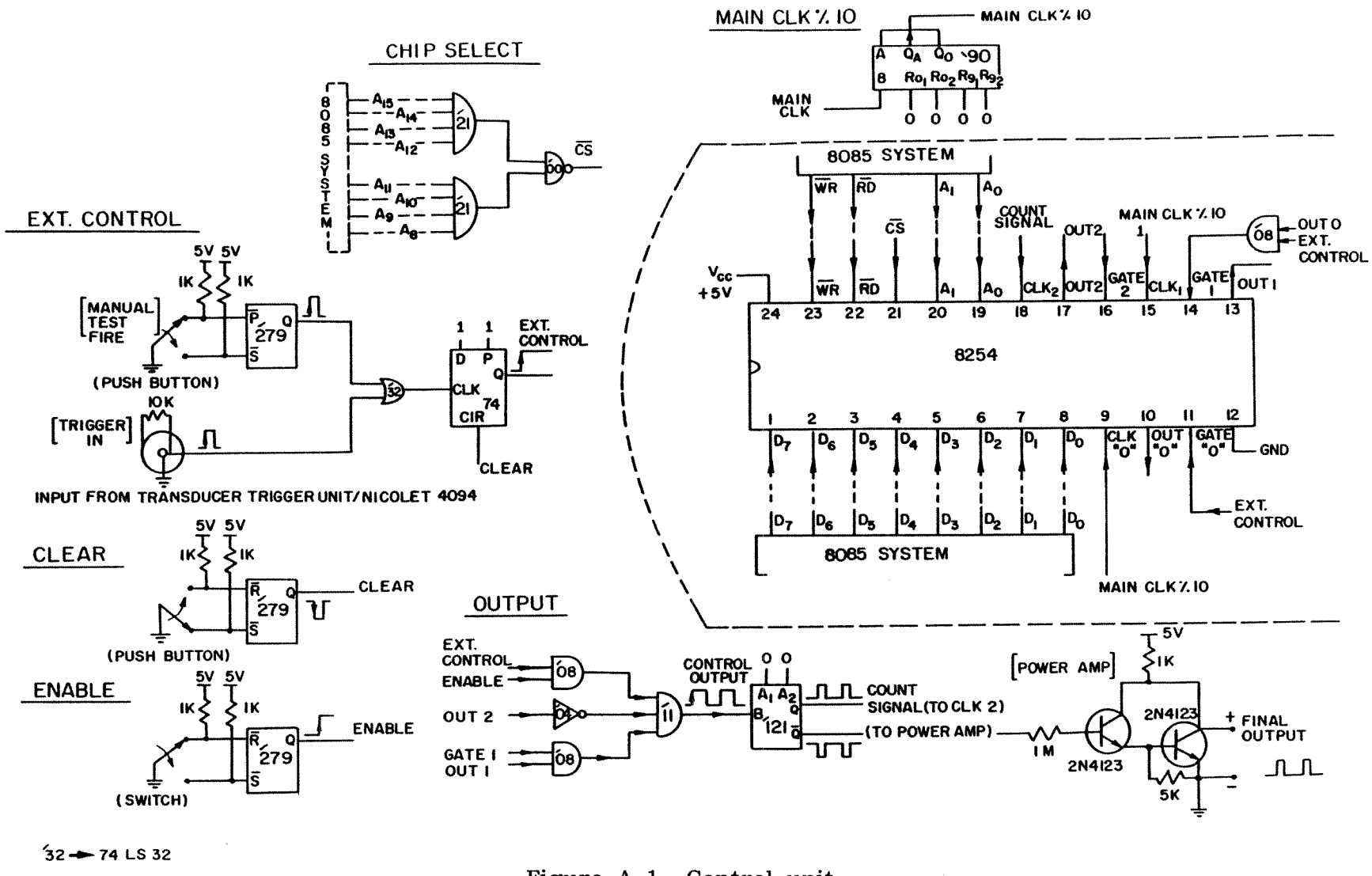

Figure A.1 Control unit

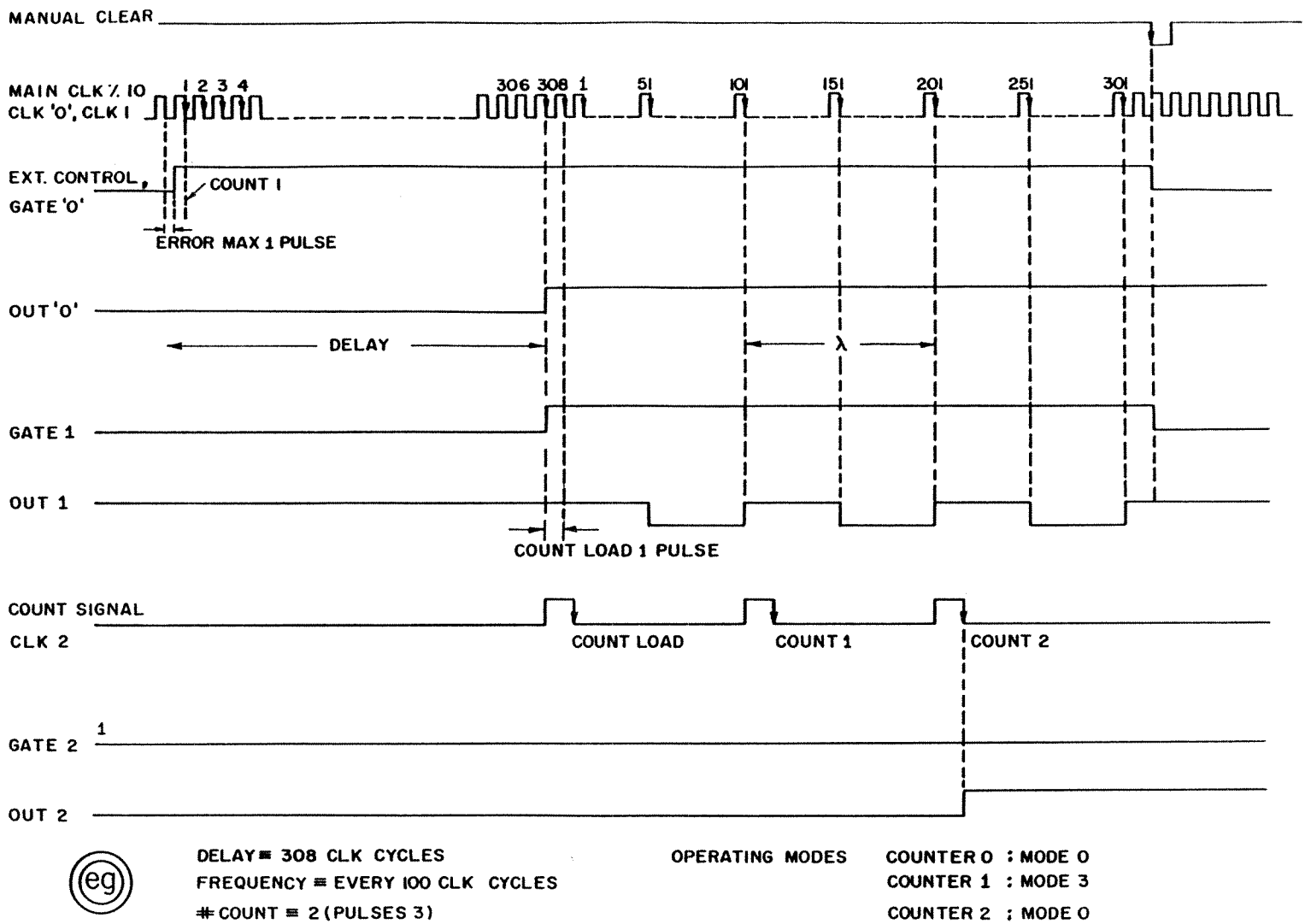

Figure A.2 Timing diagram

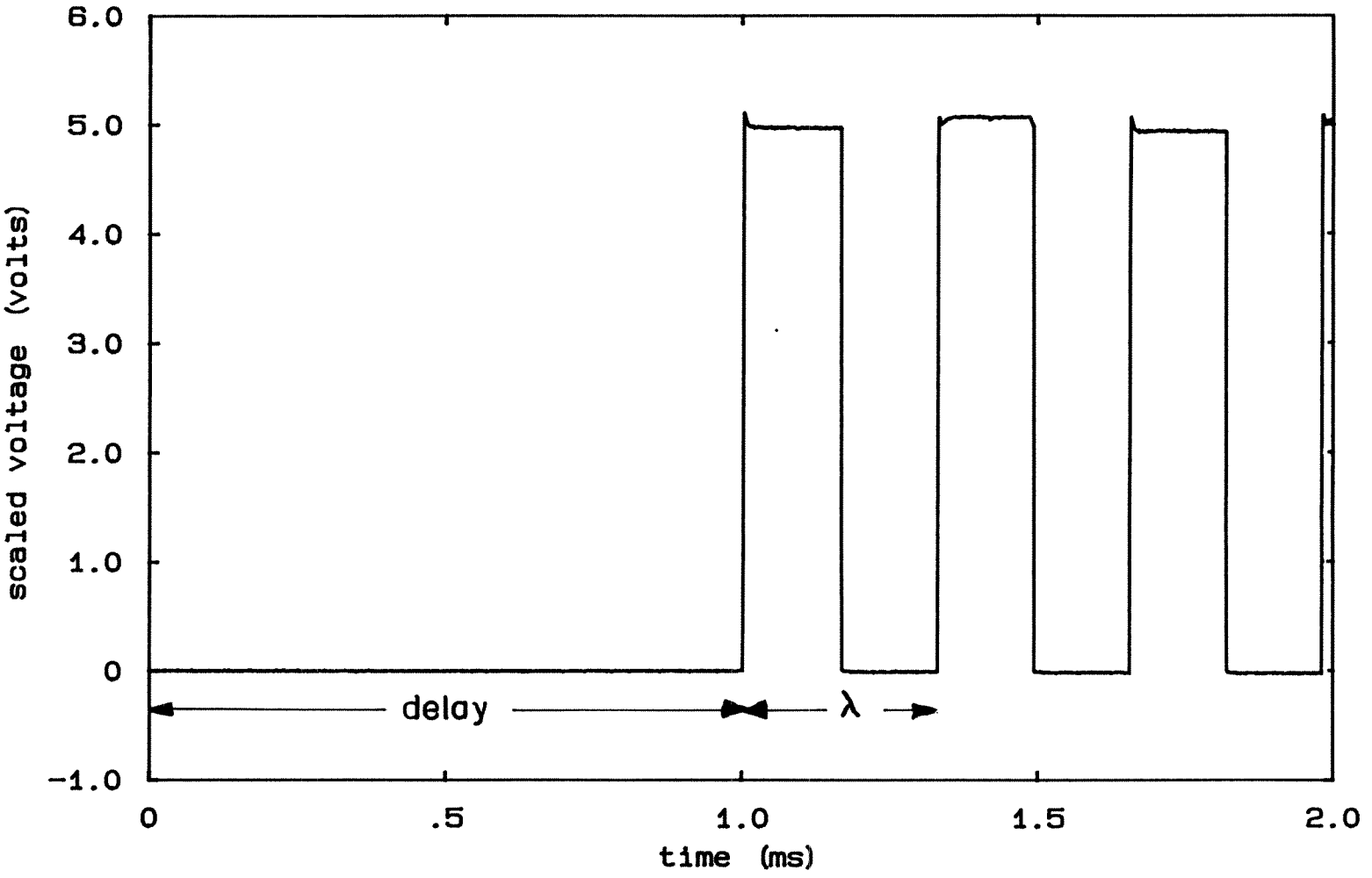

Figure A.3 Counter 1 operation (OUT 1·GATE 1)

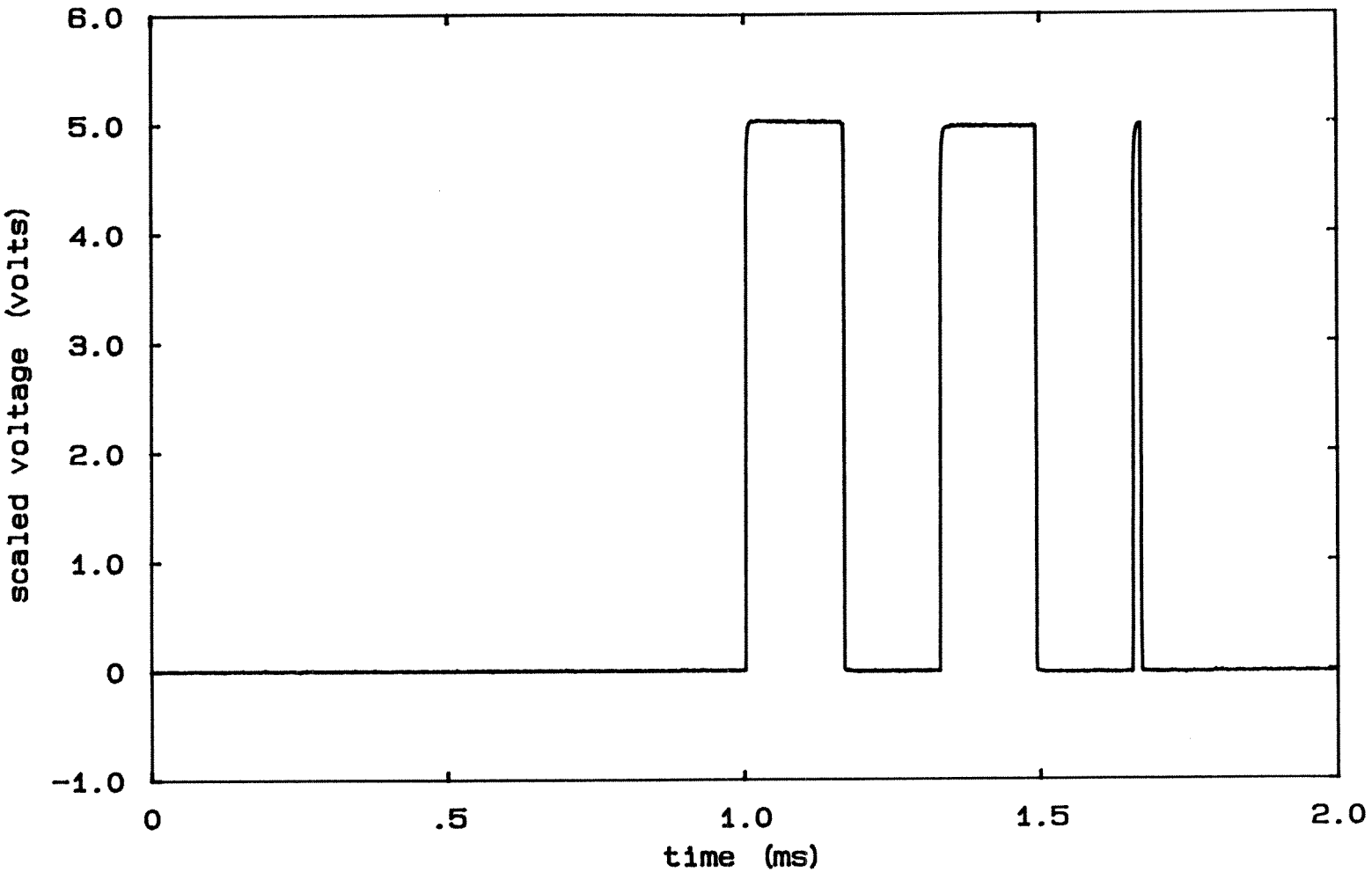

Figure A.4 Control output (with feed-back)

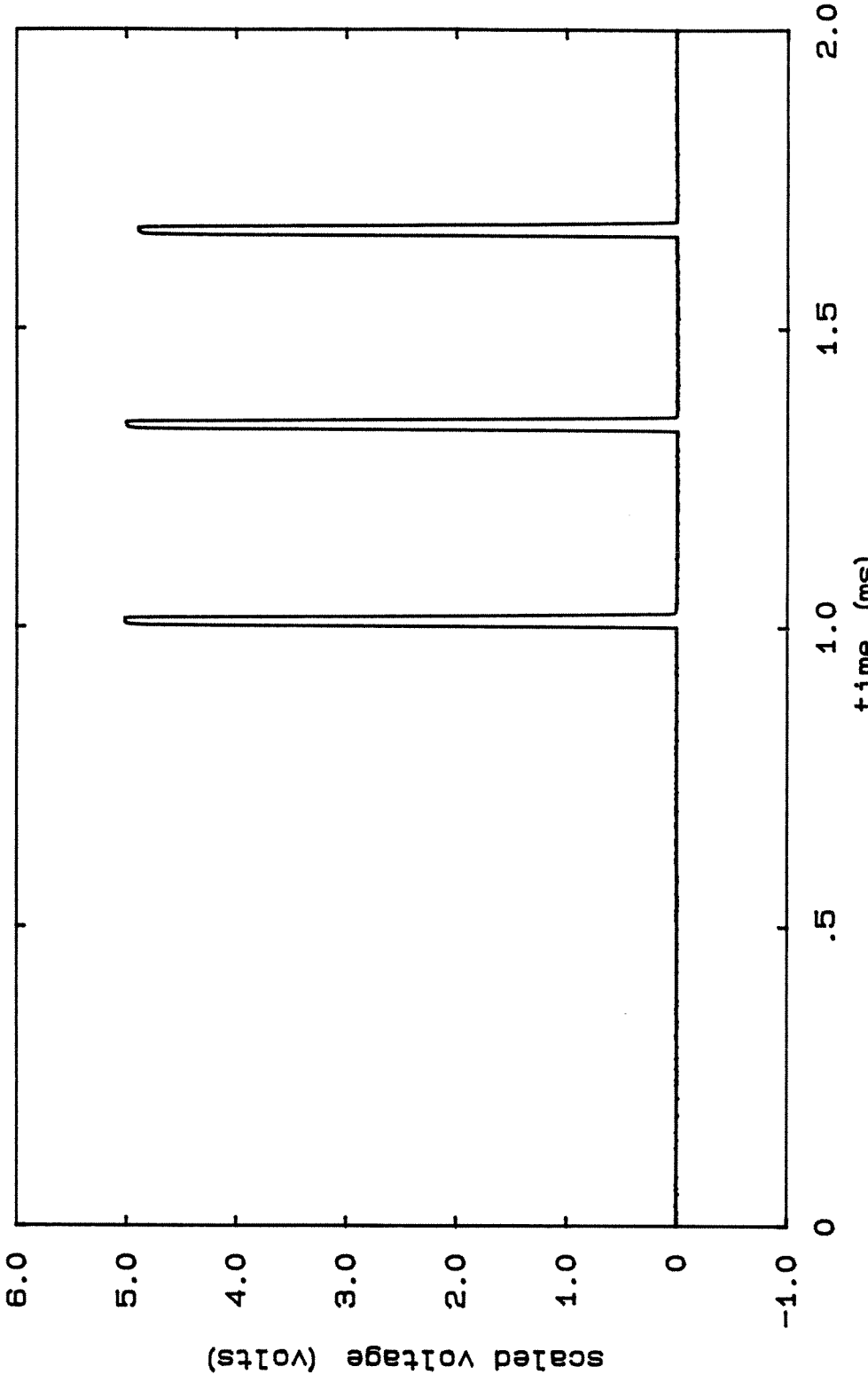

Figure A.5 Final output (from power amplifier)

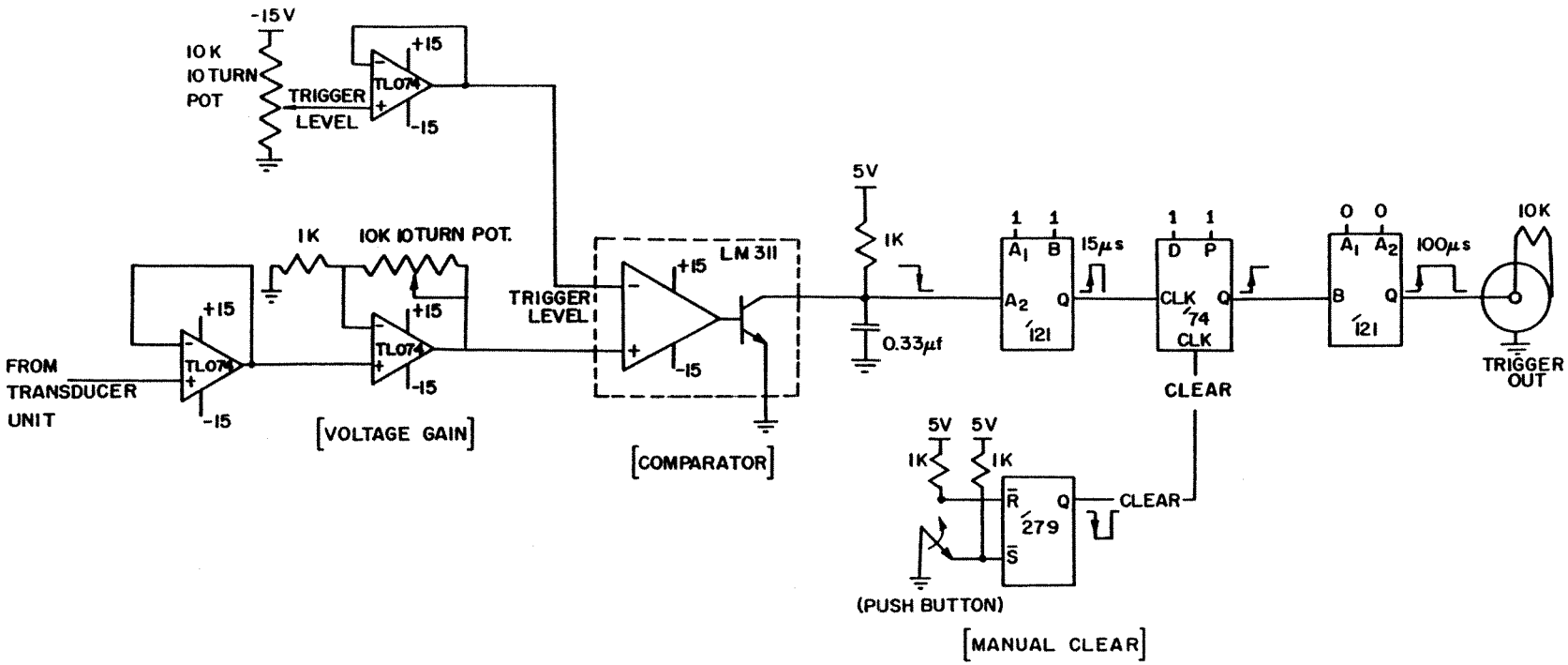

'74 → 74 LS 74

Figure A.6 Trigger unit

Appendix B

INTENSITY MEASUREMENT

A positive print of the motion picture is projected onto a photodetector and the voltage signal is recorded in real time on a Nicolet 4094 Digital Oscilloscope.

Figure B.1 shows the arrangement. The Eiki projector operates at 24 frames per second. The projector lamp is nominally rated at 250 watts and 24 volts. The lamp can be set for high or low intensity operation. The lamp light is continuously chopped by a three-blade timing shutter, and thereby the light incident on the film is switched on/off at 72 Hz. The light intensity shows negligible drift during the total duration of measurement (16 secs.). The light beam carrying the intensity information of the film is reflected off a piece of scratch-free plane glass and is passed in sequence through an infrared filter, and neutral-density filters. This leads to a beam of manageable intensity which is then condensed on to a photodetector.

The photodiode package (UDT 555D) has a detector, with a 1 cm sq. active area that can take a maximum light intensity of 10 milliwatt, and an operational amplifier. The photodetector is operated in the photo-conductive mode. The amplifier circuit (Figure B.2) operating at ±15V has a variable feed-back resistor and a 0.001 μf feed-back capacitor. The feed-back resistor is kept above 10 KΩ to avoid over illuminating the detector.

B.1. Measurement Procedure.

The signals are sampled on the oscilloscope at 500 Hz., a rate suitable to accommodate a full motion picture in one sweep. The preliminary procedures involve the projection of the film onto the photodiode and by trial, selecting a suitable combination of lamp intensity, neutral-density filters and feed-back resistor to get an optimal voltage trace. The final measurement is made with the ambient

lights switched off. First the output voltage, V_0, is nulled by adjusting the offset potentiometer. The projector is then switched on, and the film is projected, and the voltage trace recorded.

The photodiode output voltage signal is linerly proportional to the intensity of light incident on it. The light beam incident on the photodiode carries the frame-by-frame information of the photographic density of the film. The photographic density recorded on each frame of the film is logarithmically proportional to the the average light intensity it was exposed to during filming; a characteristic of any photographic film. Hence, the voltage signal of the photodiode represents a logarithmic scale of intensity variation.

Figure B.3 shows a raw voltage signal. The signal contour is the frame-by-frame history of the movie. The initial baseline signal is the transmission through the dark areas of the film. Figure B.4 represents a processed signal. The peak voltage for all movie traces is artificially scaled to 10 volts.

Two types of motion picture prints, medium and high contrast, were projected onto the photodetector. Figure B.5 shows the high contrast motion picture version of Figure B.4. The high contrast print has a modified response curve with bright regions brighter and dark regions darker. It makes a better motion picture for viewing purposes. It also gives a better idea of the relative density distribution in the dusty flow. Photographic prints, made from the movie original and presented along with the photodiode trace, are generally of the high contrast type, and therefore high contrast movie prints have been put to use.

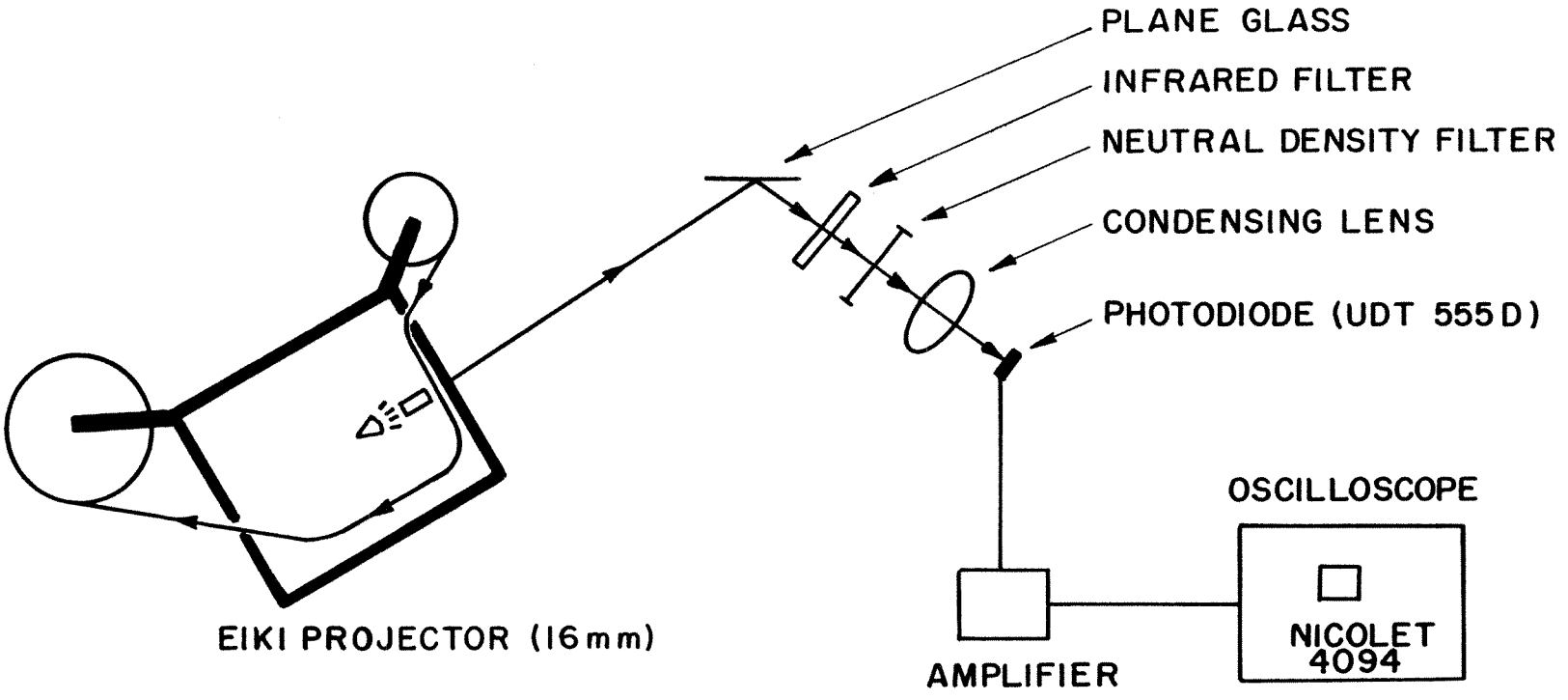

Figure B.1 Intensity measurement set up

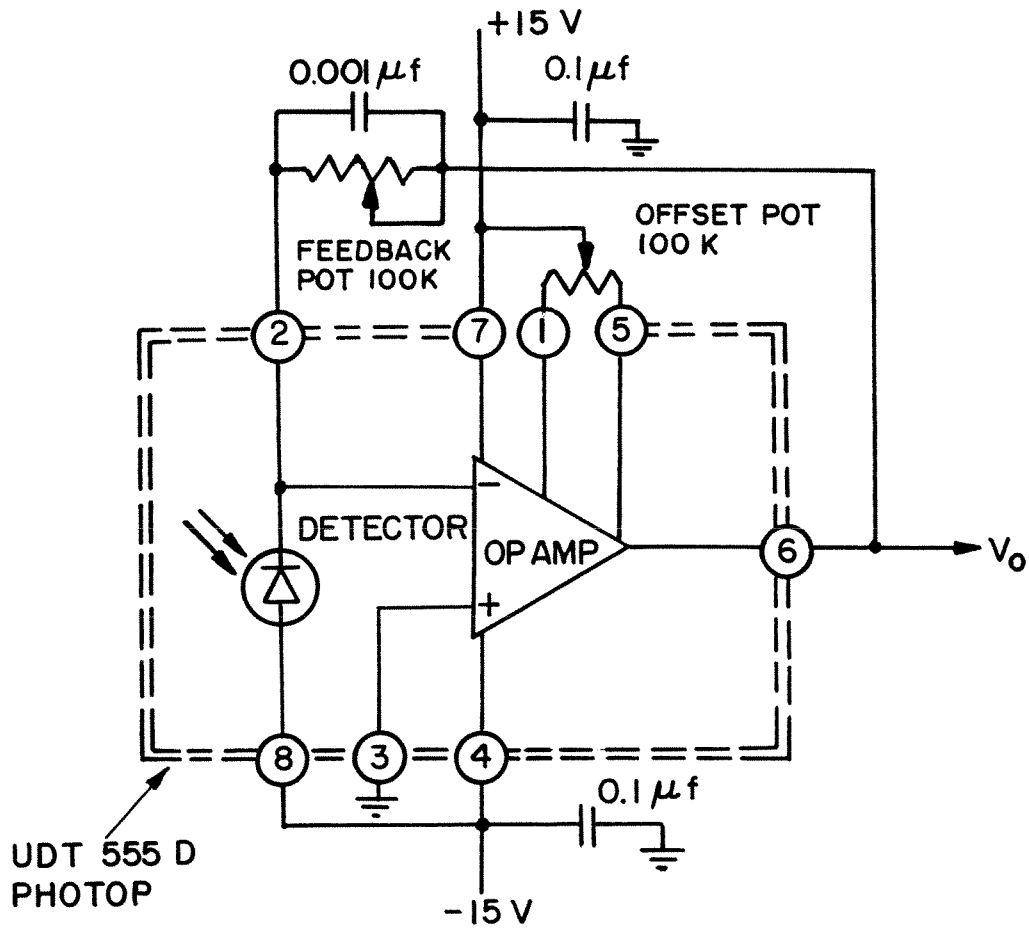

Figure B.2 Photodetector arrangement

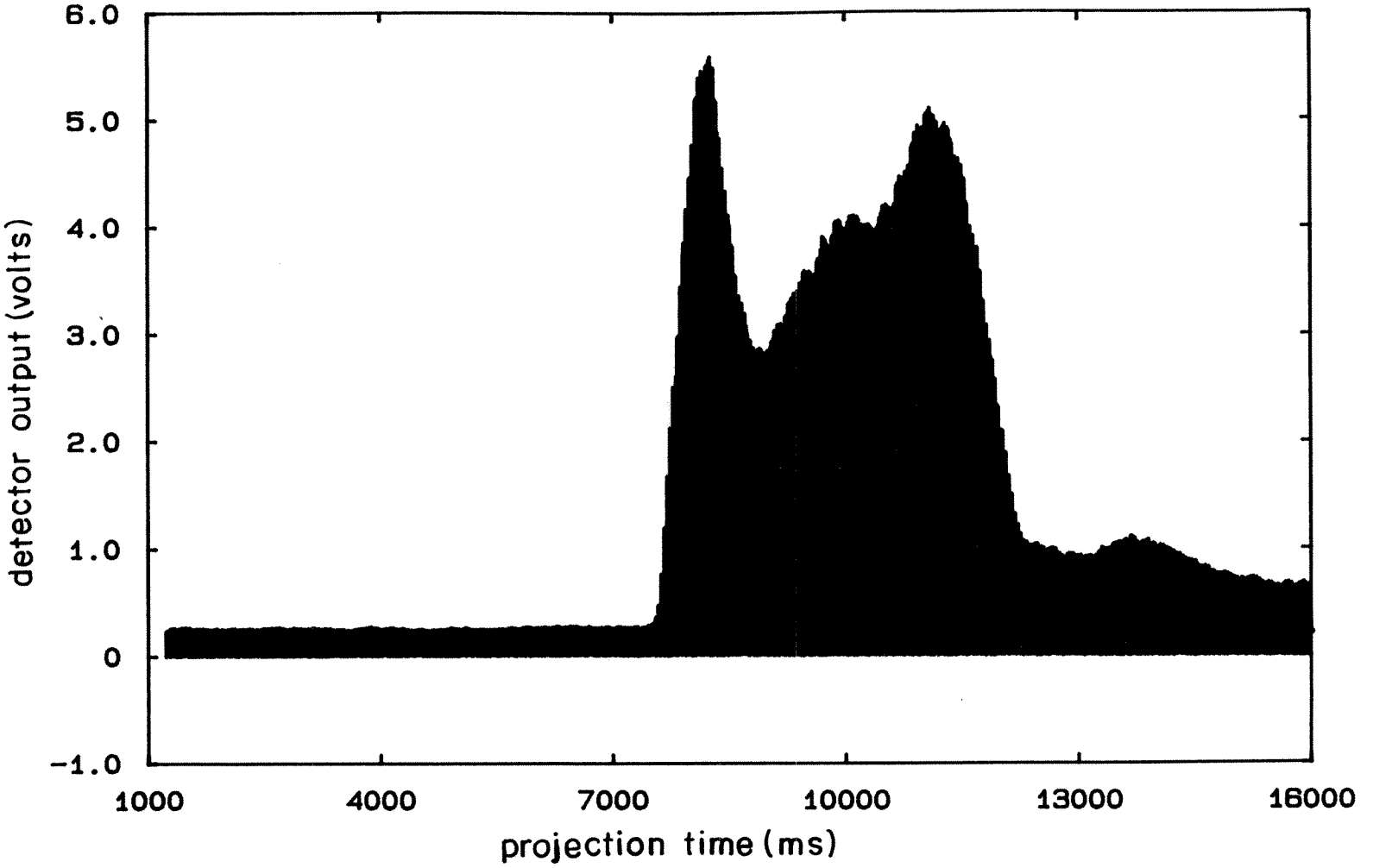

Figure B.3 Raw data

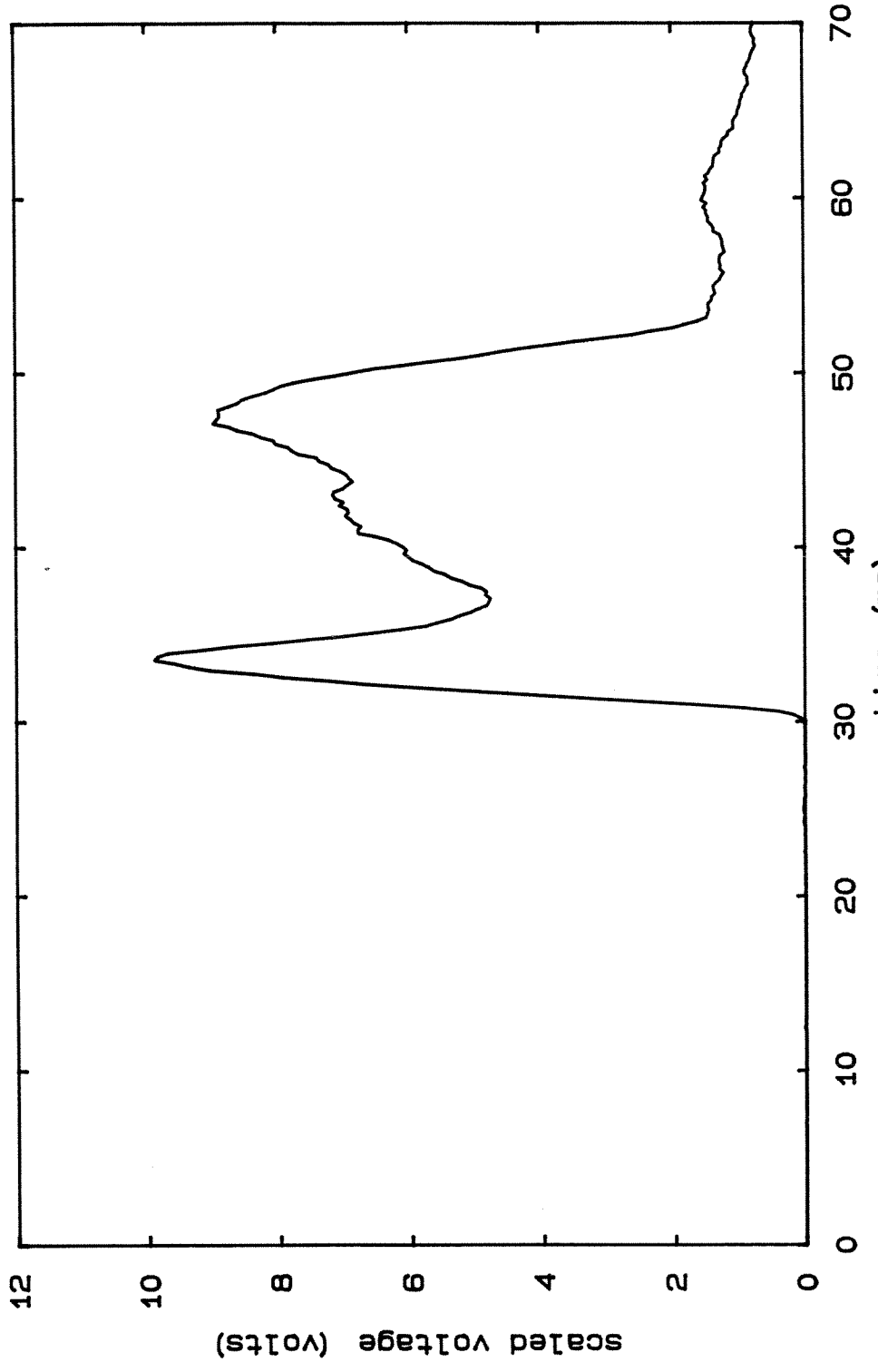

Figure B.4 Processed data

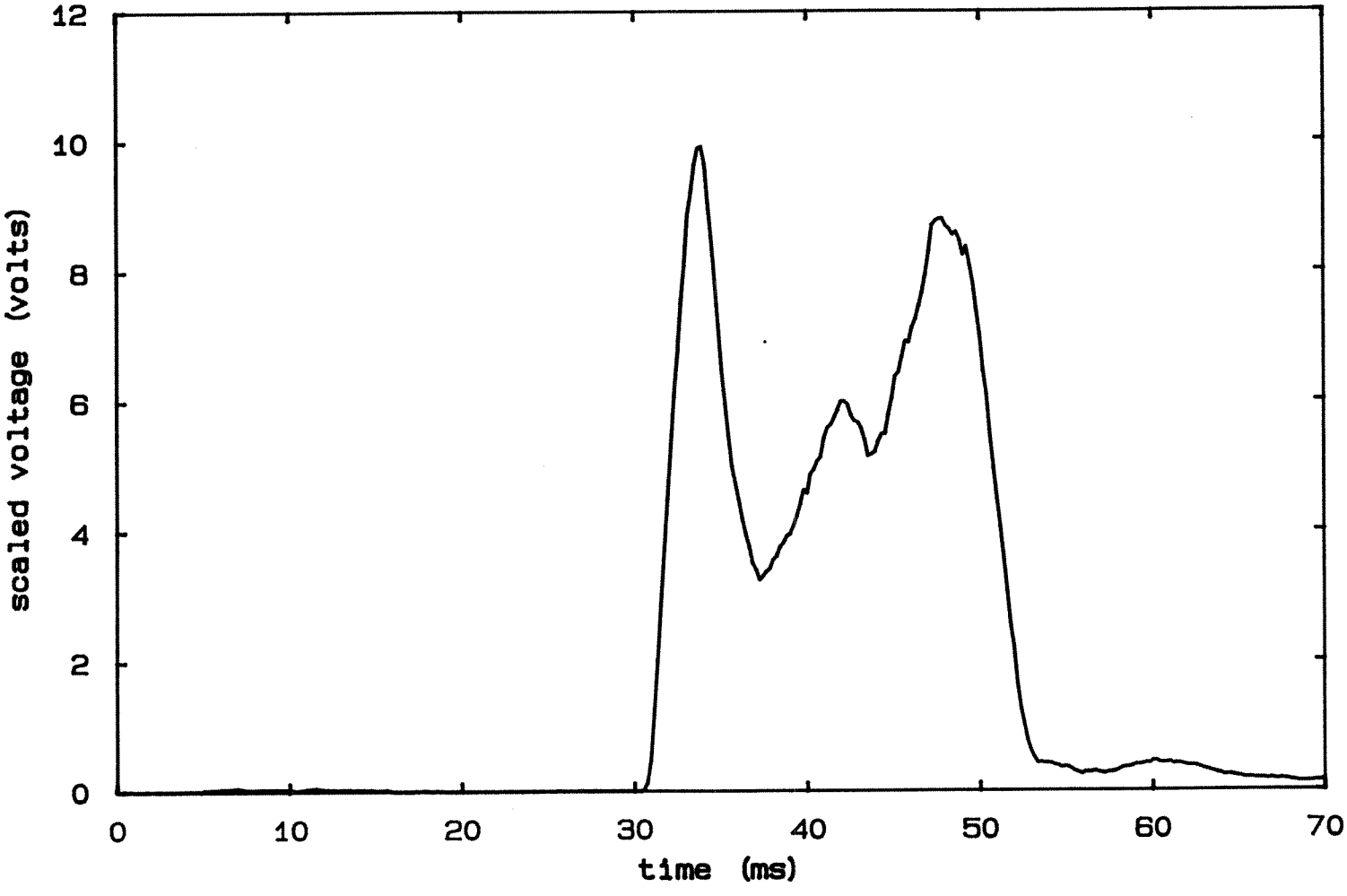

Figure B.5 Processed data (high-contrast motion picture)

Appendix C

CENTERED EXPANSION FAN

Consider a centered expansion fan (Liepmann and Roshko; 1957) moving into a gaseous region at pressure P_0 (bar, gauge), and density ρ_{g0}. Let the speed of sound in the medium be A. Let P_1 and ρ_g represent the instantaneous pressure and density during the depressurization process.

The instantaneous strength of the expansion is $\frac{P_0 + 1}{P_1 + 1} \equiv K$. For a constant K, the depressurization is complete and steady fluid flow conditions are established. We have,

$$\text{instantaneous fluid velocity} \quad u_g = A \frac{2}{\gamma - 1} [1 - K^{-\frac{(\gamma-1)}{2\gamma}}] \quad , \tag{C1}$$

$$\text{instantaneous gas density} \quad \rho_g = \rho_{g0} (1 - \frac{\gamma - 1}{2} \frac{u_g}{A})^{\frac{2}{\gamma-1}} \quad , \tag{C2}$$

With a knowledge of instantaneous particle velocity u_p, through motion-picture photography, one can estimate the instantaneous particle Reynolds number, Re.

$$\text{Re} = \frac{\rho_g (u_g - u_p) d_p}{\mu} \tag{C3}$$

where d_p is the particle diameter, and μ is the dynamic viscosity of the gas.

The instantaneous dynamic pressure of the gas DP_{gas}, can be estimated as:

$$DP_{gas} = \frac{1}{2} \rho_g \, u_g^{\,2} \tag{C4}$$

Appendix D

STEADY FLOW THROUGH POROUS MEDIA

At low Reynolds numbers ($\mathrm{Re} = \frac{\rho_g U d_p}{\mu}$; $\mathrm{Re} < 1$), the through flow velocity U of a gas of density ρ_g and viscosity μ past a porous bed of particles of size d_p is given by the linear constitutive relation, Darcy's law

$$U = - \frac{k}{\mu} \frac{\partial p}{\partial x} \quad , \tag{D1}$$

where κ is the permeability of the bed, and $\frac{\partial p}{\partial x}$ is the driving pressure gradient across the bed. For high Reynolds numbers, the relation between through flow velocity and pressure gradient becomes nonlinear. This nonlinear resistance is modeled by the Forscheimer relation

$$U + b \rho_g U^2 = - \frac{\kappa}{\mu} \frac{\partial p}{\partial x} \quad , \tag{D2}$$

where b is the Forscheimer constant.

For uniform porous media, coefficient κ has been empirically evaluated by Blake and Kozeny and coefficient b has been empirically evaluated by Ergun (see Davidson *et al.*, 1960). With the pressure gradient term replaced by an average pressure drop across the bed, the governing equation for the average through flow velocity ($\overline{U}$) in a porous bed is

$$\frac{\Delta P}{l} = \frac{150}{d_p^{\,2}} \frac{1 - \varepsilon^2}{\varepsilon^3} \mu \overline{U} + \frac{1.75}{d_p} \frac{(1 - \varepsilon)}{\varepsilon^3} \overline{\rho_g} \, \overline{U}^2 \quad , \tag{D3}$$

where ε, is the bed porosity and l is the bed height and $\overline{\rho_g}$ is the average gas density corresponding to the average of the end pressures. The through flux past

the bed is $\bar{\rho}_g \bar{U}$ and the Reynolds number of the through flux is $\frac{\bar{\rho}_g \bar{U} d_p}{\mu}$.

Equation D3 is the Ergun equation. It was first developed for liquid flow through porous media.

References

BAKER, G.R., McCRORY, R.L., VERDON, C.P. & ORSZAG, S.A. 1987 Rayleigh-Taylor instability of fluid layers. *J. Fluid Mech.*, **178**, 161-175.

BIRD, R.B., STEWART, W.E. & LIGHTFOOT, E.N. 1960 *Transport Phenomena*, John Wiley & Sons, New York.

BRACHT, K. & MERZKIRCH, W. 1979 Dust entrainment in a shock-induced, turbulent air flow. *Int. J. Multiphase Flow,* **5**, 301-312.

CABLE, A.J. & COX, R.N. 1963 The Ludwieg pressure-tube supersonic wind tunnel. *The Aeronautical Quarterly,* **14**, 143-157.

DAVIDSON, J.F., HARRISON, D. & GUEDES DE CARVALHO, J.R.F. 1977 On the liquidlike behavior of fluidized beds. *Ann. Rev. Fluid Mech.,* **9**, 55-86.

DAVIES, R.M. & TAYLOR, G.I. 1950 The mechanics of large bubbles rising through extended liquids and through liquids in tubes. *Proc. Roy. Soc. London Ser.* **A 200**, 375-390.

DIDWANIA, A.K. & HOMSY, G.M. 1981 Rayleigh-Taylor instabilities in fluidized beds. *I&EC Fundamentals,* **20**, 318-323.

DUSSOURD, J.L. & SHAPIRO, A.H. 1958 A deceleration probe for measuring stagnation pressure and velocity of a particle-laden gas stream. *Jet Propulsion,* **28**, 24-34.

EL-KAISSY, M.M. & HOMSY, G.M. 1976 Instability waves and the origin of bubbles in fluidized beds. *Int. J. Multiphase Flow,* **2**, 379-395.

FORTES, A.F., JOSEPH, D.D. & LUNDGREN, T.S. 1987 Nonlinear mechanics of fluidization of beds of spherical particles. *J. Fluid Mech.*, **177**, 467-483.

HAPPEL, J. & PFEFFER, R. 1960 The motion of two spheres following each other in a viscous fluid. *A.I.Ch.E. Journal*, **6**, 129-133.

HILL, M.K. 1973 Behavior of spherical particles at low Reynolds Nos in a fluctuating translational flow. Ph.D Thesis, California Institute of Technology, Pasadena.

KIEFFER, S.W. & STURTEVANT, B. 1984 Laboratory studies of volcanic jets. *J. Geophysical Res.*, **89**, 8253-8268.

LIEPMANN, H.W. & ROSHKO, A. 1957 Elements Of Gasdynamics, John Wiley & Sons, New York.

LUDWIEG, H. 1957 Tube wind tunnel - a special type of blow down tunnel. AGARD Report 143.

MORRISON, F.A., Jr., 1977 Transient non-Darcy gas flow in a finite porous bed. *ASME J. Fluids Engg.*, **99**, 779-781.

NILSON, R.H., 1981 Transient fluid flow in porous media : inertia-dominated to viscous-dominated transition. *ASME J. of Fluids Engg.*, **103**, 339-343.

ROWE, P.N. 1971 Chapter 4 in *Fluidization*, Academic Press, London.

SHARP, D.H. 1983 An overview of Rayleigh-Taylor instability. In *International Conference on 'Fronts, Interfaces and Patterns'*, Los Alamos National Laboratory.

SPARKS, R.S.J., WILSON, L. & HULME, G. 1978 Theoretical modeling of the generation, movement, and emplacement of pyroclastic flows by column collapse. *J. Geophysical Res.*, **83**, 1727-1739.

TSUJI, Y., MORIKAWA, Y. & TERASHIMA, K. 1982 Fluid-dynamic interaction between two spheres. *Int. J. Multiphase Flow,* **8**, 71-82.

VALENTINE, G.A. & FISHER, R.V. 1986 Origin of layer 1 deposits in ignimbrites. *Geology,* **14**, 146-148.

VOIGHT, B. (ed) 1979 *Rockslides and Avalanches*, vol.1. Elsevier, New York.

VOLPICELLI, G., MASSIMILLA, L. & ZENZ, F.A. 1966 Nonhomogeneities in solid-liquid fluidization. *Chem. Engg. Progress Symp. Series,* **67**, 42-50.

WALKER, G.P.L. & McBROOME, L.A. 1983 Mount St. Helens 1980 and Mount Pelee 1902 - flow or surge? *Geology,* **11**, 571-574.

WILLUS, C.A. 1970 An experimental investigation of particle motion in liquid fluidized beds. Ph.D Thesis, California Institute of Technology, Pasadena.

WILSON, C.J.N. 1985 The Taupo eruption, New Zealand II. The Taupo ignimbrite. *Phil. Trans. Roy. Soc. London,* **A314**, 229-310.

WILSON, L., SPARKS, R.S.J. & WALKER, G.P.L. 1980 Explosive volcanic eruptions IV. The control of magma properties and conduit geometry on eruption column behaviour. *Geophys. J. Roy. Astro. Soc.,* **63**, 117-148.

YERUSHALMI, J. & AVIDAN, A. 1985 Chapter 7 in *Fluidization*, Academic Press, London.

YERUSHALMI, J., TURNER, D.H. & SQUIRES, A.M. 1976 The fast fluidized bed. *Ind. Eng. Chem., Process Des. Dev.,* **15**, 47-53.

ZENZ, F.A. & OTHMER, D.F. 1960 Chapter 10 in *Fluidization and fluid-particle systems*, Van Nostrand-Reinhold, Princeton, New Jersey.

ZERNOW, L., LOUIE, N., ANDERSEN, H. & BLATZ, P.J. 1973 An experimental study of the reverse percolation lofting in a sand medium, DNA Report 3210F, Whittaker Corpn., Sherman Oaks.